Interactions of Cytochrome P450 3A4 with Phospholipid Bilayer Nanodiscs

Wynton D. McClary

A dissertation
submitted in partial fulfillment of the
requirements for the degree of

Doctor of Philosophy

University of Washington
2016

Reading Committee:
William M. Atkins, Chair
Rheem A. Totah
Abhinav Nath

Program Authorized to Offer Degree:
Medicinal Chemistry

University of Washington

Abstract

Interactions of Cytochrome P450 3A4 with Phospholipid Bilayer Nanodiscs

Wynton Delfon McClary

Chair of the Supervisory Committee:
Professor William M. Atkins
Department of Medicinal Chemistry

Cytochrome P450s (CYPs) are the major drug-metabolizing enzyme in humans. Cytochrome P450 3A4 (CYP3A4), in particular, is responsible for approximately half of all CYP-mediated drug metabolism. In mammals, drug-metabolizing CYPs are membrane proteins, and molecular dynamics simulations have been performed by several groups in order to probe how the membrane influences the dynamics of the CYP structure. However, the crystal structures used in these simulations were obtained in the absence of the membrane. As such, simulations using the resolved crystal structures may not accurately represent how the membrane affects CYP dynamics and thermal stability *in vivo*. Experimental techniques, therefore, are necessary in order to arrive at a complete understanding of CYP-membrane interactions. Using phospholipid nanodiscs as a model membrane, stopped-flow spectroscopy was performed in order to investigate the role of the membrane in modulating the dynamics of ligand binding to CYP3A4. Evidence is presented which suggests that some hydrophobic drugs may not be required to partition into the membrane in order to bind the CYP3A4 active site. Differential scanning calorimetry (DSC) was used to probe the effects of lipid composition on CYP3A4 thermal

stability. Results indicate that the stability of CYP3A4 is increased upon monomerization by nanodiscs. Furthermore, it is demonstrated that nanodisc lipid composition affects both the thermal stability and ligand binding dynamics of CYP3A4. These results highlight the utility of nanodiscs for studying interactions between mammalian CYPs and the membrane.

Table of Contents

Chapter 1

Interactions of Cytochrome P450s with the Membrane

1.1 Cytochrome P450 Structure and Function

Cytochrome P450s (CYPs) are a superfamily of heme-containing monooxygenases that typically catalyze the insertion of an oxygen atom into a carbon-hydrogen bond, a reaction that would otherwise have an extremely high energy of activation under typical conditions (1). CYPs are ubiquitous throughout nature and serve a critical role in the metabolism of both endogenous and exogenous substrates. For example, the fungal CYP51 is important in steroid biosynthesis, with demonstrated 14-demethylase activity (2). CYP51 has also been found in plants as well as in animals, where it is also believed to be involved in the steroid biosynthesis pathway (3,4). In humans, CYPs have been shown to play key roles in important biological pathways such as cholesterol biosynthesis and ω-fatty acid oxidation (5).

It is now well known that CYPs play a critical role in drug metabolism. It has been estimated that CYPs are responsible for the oxidation of approximately 75% of all drugs currently being marketed in the US (6,7). Of the human CYPs, the isoform CYP3A4 accounts for the majority (approximately 50%) of all CYP-mediated drug metabolism. This is due, in part, to a relatively large and flexible active site, allowing for a high degree of ligand binding promiscuity (8,9). CYP3A4 is also the most abundant drug-metabolizing isoform in humans, having high levels of expression in the liver and intestine, both key locations in the body for the detoxification of xenobiotic compounds (10,11).

Although the high degree of promiscuity seen with CYP3A4 (as well as other human CYP isoforms) allows for the metabolism of a wide array of substrates, this can potentially

become problematic when two or more drugs are metabolized by the same isoform. Interactions between drugs may occur, and they could either be favorable or unfavorable. For example, the dosage requirement of the immunosuppressant drug cyclosporine could potentially be reduced by coadministration with a CYP3A4 inhibitor, although this method has not been cleared due to the unpredictable nature of the inhibition of cyclosporine metabolism (12). Unfortunately this is often not the case, as several drug-drug interactions remain difficult to predict. This is further complicated by the difficulty in predicting the formation of potentially toxic metabolites during the drug design process, and the ability to engineer the metabolism of drugs by CYPs remains imperfect.

The structural understanding of CYPs has greatly improved over time, and we now have several crystal structures for a great number of CYPs, including but not limited to CYP2D6 (13), CYP2C9 (14), and CYP3A4 (8,15). Across all domains of life, CYPs share several common features (Fig. 1a). All CYPs are comprised of a large α-helical domain and a smaller β-sheet domain (16). All CYPs have a buried heme active site, which is immediately adjacent to the conserved I-helix. The I-helix is believed to play a critical role in proton delivery to heme-bound oxygen for the enzyme's catalytic activity (17,18). The primary feature that distinguishes mammalian CYPs from bacterial CYPs is the existence of an N-terminal membrane anchor. Many bacterial CYPs are soluble, containing the basic CYP fold yet having no particularly exposed hydrophobic regions with which to allow for association with the membrane. By contrast, mammalian CYPs are membrane-associated, the majority of which are located on the endoplasmic reticulum (ER), and some located on the outer mitochondrial membrane (19-21).

Although the structural understanding of mammalian CYPs has improved in the last decade, none of the crystal structures available for membrane-bound CYPs actually include a

membrane. Therefore, they may not be truly representative of the major conformers that exist *in vivo*. It should also be noted that due to the static nature of the resolved crystal structures, we are unable to achieve a complete picture of the dynamics of the enzyme in solution. In order to develop a more complete understanding of mammalian CYP behavior, it is necessary to systematically investigate this enzyme in a controlled membrane environment.

1.2 Mammalian Cytochrome P450 Active Site Channels and Membrane Topology

As noted previously, mammalian CYPs are membrane-bound proteins, located primarily on the surface of the endoplasmic reticulum, and they play a critical role in the metabolism of a wide array of drugs. Typically most drugs are hydrophobic to maximize drug absorption; if a drug is not hydrophobic enough, absorption from the gut will be poor, leading to low circulating levels. However, once absorbed, the hydrophobic nature of the drug would prevent it from being easily excreted from the body; most hydrophobic drugs are likely to partition into membranes and remain within them for an extended period of time. Cytochrome P450s essentially work by taking a hydrophobic compound, such as a drug, and inserting an oxygen into its structure in order to improve its water solubility. This converts the hydrophobic drug into a hydrophilic metabolite, which is more readily excreted from the body. It is presumed that the mammalian CYP structure may have evolved an increased preference for hydrophobic substrates. For instance, the hydrophobic regions on the surface of mammalian CYPs, which are primarily located proximal to the F' and G' helices, may facilitate the binding of hydrophobic drugs and be the major location of active site access channels. To investigate the location of active site channels, it is necessary to use techniques which probe the dynamics of the CYP structure. This will aid in the development of accurate models of drug binding to mammalian CYPs.

Molecular dynamics (MD) simulations have proven to be a useful tool for probing environmental effects on protein motion. This technique has provided valuable insight into the channel dynamics of several globular proteins, including several members of the CYP family (22-24). MD simulations to investigate potential locations for mammalian CYP active site access channels suggest that many channels are located adjacent to the loop formed by the F' and G' helices (F'/G' loop) as well as the loop formed by the B and C helices (B/C loop) (Fig. 1b). Collectively, these channels are referred to as the 'pathway 2' CYP active site channels (22). In addition, there may be other channels located closer to the distal, or cytosolic-facing portion of the enzyme which many have predicted are the sites of ingress and egress of small, hydrophilic ligands such as water and molecular oxygen. These channels may include, but are not limited to, the solvent channel 'S' and/or the water channel 'W' which has been predicted to be utilized by water molecules in order to reach the active site (23). These structural features are important to consider in the context of CYP orientation on the membrane surface.

Mammalian CYPs maintain their association to the membrane surface via the use of an N-terminal anchor as well as a hydrophobic face on the globular domain of the enzyme (25). The hydrophobic face, that is, the portion of the enzyme that is believed to associate with the membrane, includes the F'/G' loop, and it has been predicted that this surface of the enzyme at least partially inserts into the membrane bilayer based on epitope mapping and MD simulations (26). This orientation requires that the major active site access channels are oriented toward the membrane. This is consistent with the overall role of CYPs in converting hydrophobic substrates into hydrophilic products. Similar results were obtained from MD simulations performed by Baylon and coworkers (27). In their study, after allowing CYP3A4 in an aqueous environment to associate with a model membrane, they observed that CYP3A4 oriented was consistently

oriented such that the F'/G' loop was associated with the membrane. Furthermore, the theoretical heme-tilt angle from simulations, which measured the angle between the heme plane and the membrane, was consistent with the heme-tile angle they measured by linear dichroism, suggesting a CYP3A4 topology where the F'/G' loop faces the membrane. Although different isoforms may have varying degrees of insertion depth and may adopt slightly different angles within the membrane, this general orientation appears to be consistent for mammalian CYPs, and may serve as a way of maximizing the probability that the enzyme will bind to a hydrophobic substrate.

Taken together, the highlighted studies propose that hydrophobic substrates must partition into the lipid bilayer in order to reach the buried heme active site of the CYP prior to catalysis. This idea is sometimes referred to as "the hydrophobic substrate binding hypothesis". It has typically been assumed that all hydrophobic ligands bind to mammalian CYPs via partitioning into the membrane first. However, although there has been great improvement in our knowledge of CYP dynamics due to computational tools such as MD simulations, it must be noted that currently very little empirical evidence exists to support the proposed models. In order to arrive at a more complete picture of how various types of ligands bind to the CYP active site, techniques that reveal the pre-equilibrium kinetics of ligand binding would prove useful.

Stopped-flow spectroscopy is a rapid-mixing technique used to monitor pre-equilibrium kinetics of a process in solution that would otherwise be too fast to observe (or a schematic of the stopped-flow apparatus, see figure 2). The typical stopped-flow apparatus contains two syringes, each containing a reactant of interest. A pneumatic piston rapidly drives the contents of the two syringes through a t-shaped mixer before filling up a sample cell. When the sample cell is filled, the now mixed solution will then fill a stop syringe until it contacts an electronic switch, which

signals the instrument to begin rapidly collecting spectroscopic data from the sample cell. A typical stopped-flow apparatus has a dead time of approximately 2 milliseconds, making it a useful tool for monitoring the kinetics of rapid reactions such as ligand binding to CYPs.

1.3 Thermostability of Membrane Proteins

The thermodynamics behavior of membrane proteins is often influenced by the nature of the membrane environment that they exist in. For example, it has previously been demonstrated that bilayer thickness directly affects the probability of channel opening, via a membrane mismatch mechanism, for the mechanosensitive channel of large conductance, MscL, found in *E. coli* (28,29). The nucleotide binding domain of P-glycoprotein has been shown to have both ATP binding and ATP hydrolysis that can be modulated by the fluid phase of the membrane (30,31). It has clearly become evident that in order to arrive at a more complete picture of mammalian CYP thermodynamics behavior, it is necessary to understand how the membrane environment may influence the thermodynamic properties of these enzymes.

Several techniques exist with which to study the thermodynamic stability of proteins. One technique that has proven to be quite useful is differential scanning calorimetry (DSC) (32). This relatively straightforward technique provides a direct measure of the heat capacity and change in enthalpy for the unfolding of a sample. In the typical DSC experimental setup, a sample cell is filled with the protein of interest and a reference cell is filled with a buffer control. The temperatures of both cells is then increased, typically by increments of 1°C. Because the reference cell does not contain protein, it requires less energy to raise the temperature of the cell relative to the sample cell. This difference in energy required to increase the cells to identical temperatures corresponds to the excess specific heat capacity of the sample and can be plotted as a function of temperature.

As a protein undergoes thermal melting, a melt profile from the excess heat capacity can be generated, referred to as the DSC thermogram. Several useful pieces of information can be obtained from the thermogram. One parameter that can be determined is the transition (or melting) temperature of the sample, usually denoted as T_m. This is the temperature at which the excess heat capacity reaches a maximum and is a useful measure of the thermostability of a particular sample. Another useful parameter is the change in enthalpy, or ΔH, for the reaction. By integrating the area under the heat capacity curve, the total change in enthalpy can be determined and can provide insight as to the overall degree of covalent and non-covalent interactions within a sample; larger changes in enthalpy indicate a greater abundance of stabilizing interactions within the protein or complex.

Other properties can be investigated using DSC, such as the degree of cooperativity within a transition. In work done by Shaw and coworkers using DSC in order to investigate the phase transition properties of lipids incorporated into a nanoscale model membrane system called nanodiscs (33), when the thermal melt profile of lipid vesicles was compared to nanodiscs, it was observed that the lipid transition shifted to higher temperatures and displayed a broader peak, consistent with a loss of cooperativity of the phase transition. Combined with other data, they attribute this loss of cooperativity to the presence of a new boundary layer of lipids that is not seen in vesicles. While methods other than DSC could potentially be used to probe such as an environmentally sensitive fluorescent probe, DSC does not require any additional probe molecules which could potentially alter the phase properties of the membrane.

DSC is a powerful technique that could allow for a more in depth understanding of the thermodynamic behavior of membrane proteins, including mammalian CYPs. There are a few examples of DSC analysis being performed on mammalian CYPs. For example, work done by

Anzenbacher, Hudeček, and Stružinský, used DSC to monitor the unfolding of CYPs from rat liver microsomes (34). However, to the best of our knowledge, there has been no extensive investigation into the effects of a membrane on the thermodynamic stability or the mechanism of thermal denaturation of CYPs. Because mammalian CYPs exist in the membrane, it is necessary that we understand their thermodynamic properties in a membrane environment using techniques such as DSC.

1.4 The Role of Lipid Composition on Membrane Protein Dynamics

Most attempts to characterize membrane proteins include a membrane surrogate such as detergent, or they are carried out in a model membrane environment. It is common to use a model membrane system that is composed of a single lipid of head group type, chain length, and saturation. However, it is well known that biological membranes are a mixture of different lipid types, proteins, and other components. As such, experimental data collected in a single homogeneous lipid phase should be interpreted with caution. Membrane models with well-defined heterogeneous mixtures of lipids could reveal the effects of specific membrane properties on protein function and behavior.

As noted previously, most mammalian CYPs are located on the ER membrane. The ER membrane is the primary site of lipid and cholesterol biosynthesis within the cell (35). This organelle is composed of a wide variety of lipids with different head groups, chain lengths, and saturation in mammals. Included in the composition of this membrane is approximately 55% phosphatidylcholine, 30% phosphatidylethanolamine, 15% phosphatidylinositol, and trace amounts of phosphatidylserine and other lipids. While it is very difficult to precisely replicate the lipid composition of the ER or other biological membranes using a model membrane system *in*

vitro, there has been an increased effort in systematically investigating the effects of lipid composition on protein thermodynamics and activity.

There are several examples in the literature of the influence of lipid composition on mammalian CYPs. In 1996 it was demonstrated that relative to vesicles containing only phosphatidylcholine, nifedipine oxidation by CYP3A4 occurs with a higher V_{max} in vesicles containing a mixture of phosphatidylcholine and phosphatidylserine (36). V_{max} was further increased when utilizing microsomal vesicles. By contrast, K_m remained unaffected, suggesting that CYP3A4 operates more efficiently in a mixture of lipids while likely maintaining its conformational state. A separate study in 1998 was performed in order to investigate the effects of lipid composition on the insertion of CYP1A2 into the membrane (37). Utilizing fluorescence energy transfer, this group was able to observe an increase in how much CYP1A2 was able to insert into lipid vesicles when incorporating higher levels of anionic phospholipids. Furthermore, they observed that incorporating phospholipids containing the head group phosphatidic acid promoted deeper insertion of CYP1A2 into the vesicle membrane. These studies highlight the importance understanding how membrane lipid composition can affect CYP activity.

Many studies to date have focused on the effects of different lipid head groups on mammalian CYP activity. However, very few studies, if any, addressed the effects of chain length or saturation. In addition, to the best of our knowledge, there have been no studies which directly begin to address questions of CYP thermostability and dynamics in a mixed lipid environment. In order to address these issues, techniques such as DSC and stopped-flow spectroscopy may improve our knowledge as to how lipid composition could influence the behavior and stability of mammalian CYPs. However, a suitable membrane model is crucial in

conjunction with these techniques in order to maximize our understanding and make the system more physiologically relevant.

1.5 Phospholipid Bilayer Nanodiscs

There are now several model membrane systems which can be used to study mammalian CYPs in a more natural environment. Liver microsomes perhaps provide the most native-like environment, as these are vesicles formed from the ER in liver cells, and so the lipid composition is the most natural for the enzyme. However, microsomes contain a mixture of CYP isoforms and so are typically not very useful for studies on a single isoform. Liposomes are another useful model membrane type because these vesicles can be created artificially, and the lipid composition can easily be controlled. In addition, recombinantly expressed protein can be incorporated into liposomes, allowing for a way to control purity of the enzyme. However, the size of the liposomes can be difficult to control, although extruding techniques have improved to allow for greater homogeneity. In addition, there is a risk that some of the enzymes may become internalized during the process of liposome formation, which could result in ambiguous results from a technique such as stopped-flow spectroscopy.

A relatively new model membrane system for studying membrane proteins, including CYPs, is phospholipid bilayer nanodiscs (38-42). Nanodiscs (NDs) are nanoscale discoidal lipid bilayers which are encircled by two ‘belt-like’ membrane scaffold proteins (MSP) (Fig. 3). MSP is an amphipathic α-helical protein that was originally designed using the sequence for human apolipoprotein A-1, the major protein component of high density lipoprotein (HDL) particles, as a template (43). The nanodisc assembly process is essentially the reverse of the process that forms mature HDL particles from nascent discoidal particles. The lipid of choice is mixed with MSP in the presence of a detergent in order to form mixed micelles. The detergent is then

removed, either by dialysis or by the addition of a hydroscopic resin, in order to initiate a self-assembly process into the final discoidal particles.

Nanodiscs provide several key advantages over liposomes as a model membrane system. Because the size of a nanodisc is dictated by the length of MSP, nanodisc samples are highly homogeneous. By contrast, it is generally much more difficult to achieve a high degree of homogeneity in liposome size; much more rigorous and time-consuming techniques are necessary in order to minimize size variability (39). The size constraint is another advantage that nanodiscs have over other model membranes, depending on the goal of the study. The most commonly used nanodiscs for the study of mammalian CYPs use the MSP1D1 construct and are approximately 10 nm in diameter, and this size constraint helps to eliminate oligomerization of protein on the membrane. Liposomes, while their size can vary, are much larger than nanodiscs, typically in the micrometer range (44). This allows for protein oligomerization on the membrane, which could become a complicating factor for some studies. Additionally, nanodiscs are much more stable to sudden perturbations relative to liposomes, making them a more robust system for various techniques. For these reasons, nanodiscs should continue to prove to be a useful *in vitro* model membrane system for the study of membrane proteins and mammalian CYPs in particular. However, it should be noted that there is a likelihood of oligomerization *in vivo*, which could potentially shift the activity of mammalian CYPs (45). Thus, while nanodiscs allow for *in vitro* monomerization of the enzyme in a native-like environment, they may not be fully representative of the *in vivo* environment of mammalian CYPs.

In conclusion, there is a need to understand ligand binding dynamics and the thermal stability of CYPs in a native-like membrane environment. To this end, we have exploited stopped-flow spectroscopy and differential scanning calorimetry in order to extend our

biophysical knowledge of mammalian CYPs. Nanodiscs provide a useful model membrane system due to the ease with which the lipid composition can be manipulated, as well as their constrained size, which allows for monomerization of membrane proteins and removes any ambiguities which may arise from oligomeric states. By incorporating CYP3A4 into nanodiscs as a representative mammalian CYP, we will address CYP3A4's ligand binding dynamics and thermal stability in a more native-like environment.

1.6 Figures

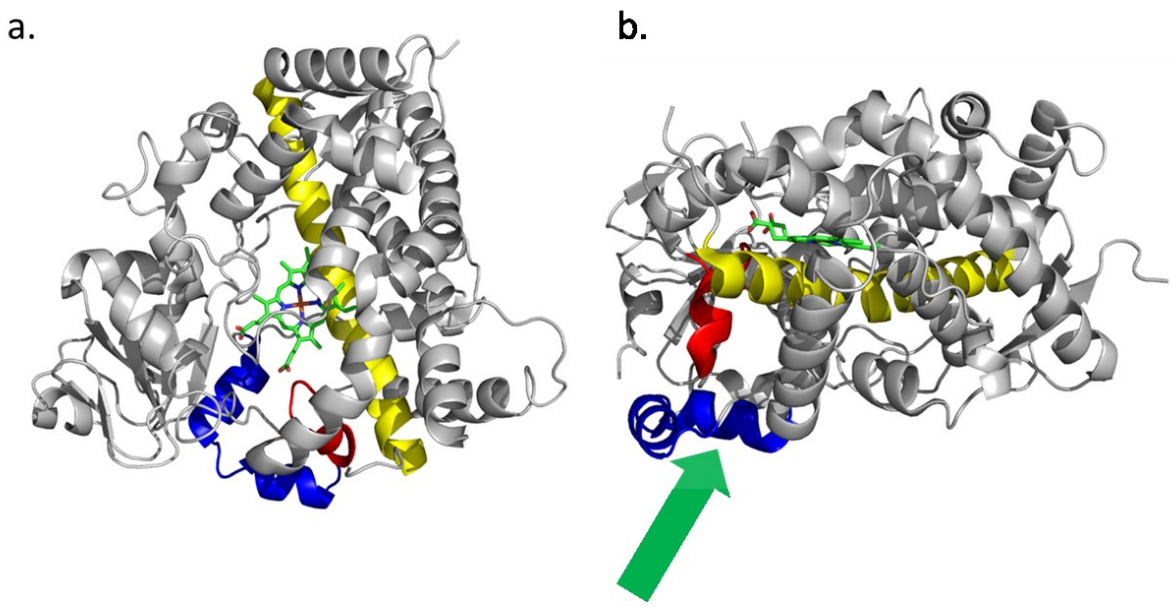

Figure 1. Crystal structure of CYP3A4 (PDB 1TQN) as viewed from the top (a) and from the side (b). Highlighted are the I-helix (yellow), the F/G loop (blue) and the B/C loop (red). The general paradigm has been that hydrophobic ligands utilize a channel(s) in an area adjacent to the F/G and B/C loops (denoted by the green arrow) in order to reach the buried heme active site.

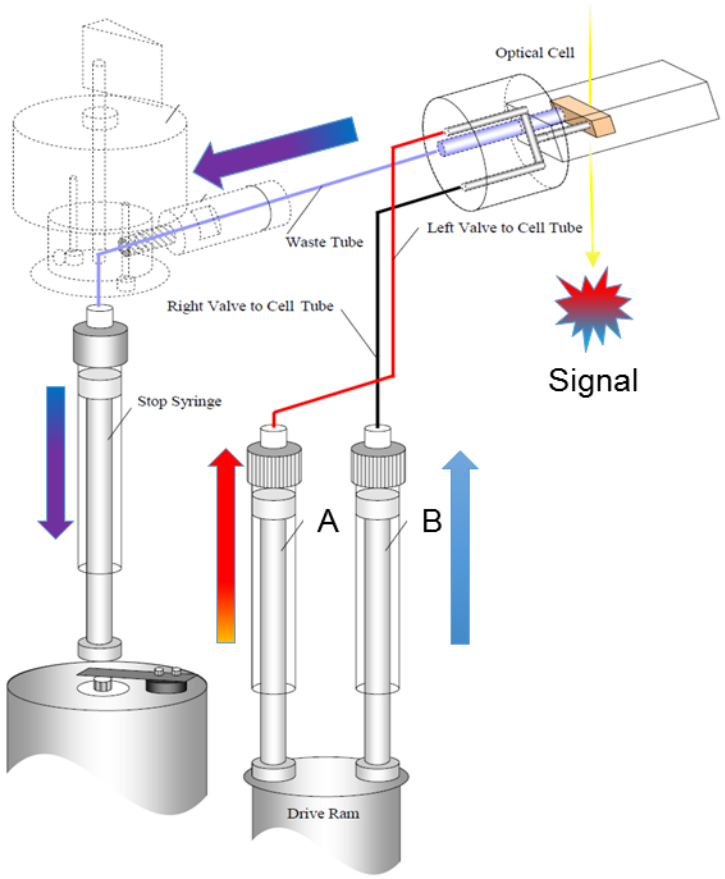

Figure 2. Stopped-flow schematic diagram, adapted from the SX-20 stopped-flow user manual (Applied Photophysics, UK). Two reactants are loaded into syringes A and B. A pneumatic piston then rapidly drives the contents of each syringe through a t-shaped mixer and the resulting solution fills an optical cell. Once the optical cell is full, the mixed solution fills a stop syringe until the syringe triggers an electronic switch, signaling the instrument to begin rapidly collecting absorbance or fluorescence data from the optical cell.

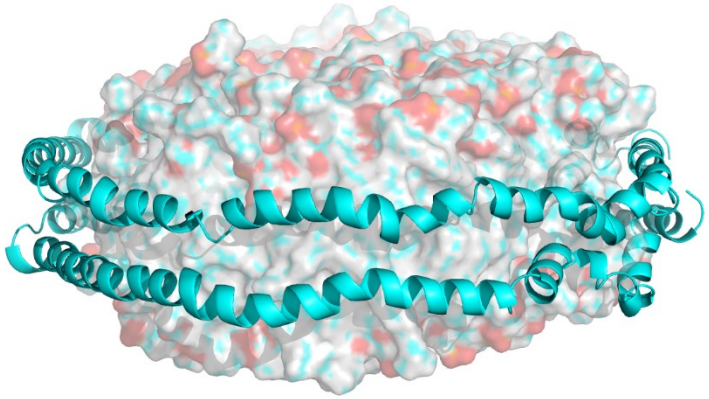

Figure 3. Representative structure of an empty nanodisc. The lipid bilayer is held together by two membrane scaffold proteins (cyan ribbons). Nanodiscs made with the scaffold protein MSP1D1 have a diameter of approximately 10 nm.

Chapter 2

Kinetic Studies of Ligand Binding to Cytochrome P450 3A4 in Nanodiscs

2.1 Introduction

Cytochrome P450s (CYPs) play a critical role in the metabolism of a diverse array of endogenous and xenobiotic compounds. This superfamily of enzymes are responsible for the metabolism of approximately 75% of all currently marketed drugs (6). CYPs have been implicated in the adverse side effects observed for a wide array of drugs currently in the market. This is often due to the production of toxic metabolites and drug-drug interactions. As such, it is widely acknowledged that improving our understanding of the dynamic behavior of CYPs is necessary in order to improve the overall drug design process.

An important question with regards to the dynamic behavior of CYPs is the mechanism of drug binding to the CYP active site. Crystal structures show that the heme active site of CYPs is located in core of the enzyme (Fig. 1), indicating that active site channels must exist in order for drugs to reach the site of catalysis. Therefore, the mechanism by which different drugs bind to the CYP active site may be influenced by the dynamics of the active site channel(s). Experimental insight into this question is extremely limited, however. Molecular dynamics is currently the only technique available for specifically probing the channel dynamics of CYPs. Nevertheless, as noted in chapter 1, molecular dynamics simulations have provided a glimpse into the conformational dynamics of several proteins and location of active site access channels in mammalian CYPs (22).

A key finding of molecular dynamics simulations performed on mammalian CYPs is the identification of a class of channels, deemed ‘pathway 2’ (pw2), which are located proximal to

the F'/G' (Fig. 1) (23). The pw2 channels has been proposed as the most likely route for the majority of larger CYP ligands, as this pathway appears to be most commonly occurring among different isoforms. Furthermore, the nearby B/C loop has previously been proposed to serve as a substrate recognition site (46). Indeed, several separate simulations performed on CYPs also suggest that pw2 is the most predominant pathway for ligand access to the active site (22,24,47). X-ray crystallography has also shown that in the bound state, amlodipine molecules lie in a channel in both CYP2B4 and CYP2B6 channel that would be classified as part of pw2, adding further support that this pathway is a dominant pathway in the binding of larger CYP ligands (48).

Although molecular dynamics simulations have been performed on several CYPs and provide important information about the protein dynamics, until recently the majority of these simulations have been performed in an aqueous environment. However, because mammalian CYPs are membrane proteins, it becomes necessary to study these enzymes in a membrane environment, as the membrane can potentially affect the dynamics of ligand binding and release. For instance, molecular dynamics studies suggest that product release may be the rate-determining step in the CYP2E1-catalyzed metabolism of ethanol, and that this release rate is dictated by the dynamics of the product egress channel (49). However no studies have been conducted to monitor ethanol binding to CYP2E1 in the presence of a membrane.

The topology of mammalian CYPs relative to the membrane has also been a subject of interest as it relates to the mechanism of binding for larger hydrophobic ligands. It has generally been accepted that mammalian CYPs are oriented such that the F'/G' loop interacts with the membrane bilayer. Recently, a crystal structure for CYP51 in a detergent micelle was resolved and suggests that the F'/G' loop interacts with the micelle surface (50). The general orientation

of mammalian CYPs where the F'/G' loop associates with the membrane bilayer has also been observed by others using molecular dynamics simulations on several other CYP isoforms, including, but not limited to, 3A4, 2A6, 2C9, 2E1, and 2D6 (26,51). The predicted orientation of mammalian CYPs on the membrane, as well as the predicted routes of substrate access to the CYP active site, has led to the proposal of the "hydrophobic substrate binding hypothesis" which predicts that mammalian CYPs are oriented on the membrane in such a way that hydrophobic substrates are required to partition into the membrane bilayer in order to reach the necessary CYP active site channel.

It has previously been proposed that the membrane can modulate the dynamic behavior of mammalian CYPs. Molecular dynamics simulations were performed on CYP2C9 in solution and in a model membrane environment. Upon incorporation of CYP2C9 into a membrane, channel 2a, a member of the pw2 class of active site channels, displayed a larger channel radius, relative to the enzyme in a fully aqueous environment (52). This channel passes through a region adjacent to the B/C and F'/G' loop and is believed to lead into the membrane. A similar phenomenon was seen by Baylon and coworkers by performing molecular dynamics simulations for CYP3A4 (27). Incorporation of CYP3A4 into a membrane resulted in significant opening of the pw2 channels 2b and 2e, both of which are believed to be oriented towards the membrane. These data suggest that the membrane may also play a role in modulating channel dynamics, which in turn may affect the dynamics of ligand binding to the active site.

Despite the utility of molecular dynamics simulations in probing CYP conformational dynamics, the results are limited by the fact that they were attained *in silico* and thus do not necessarily represent the true dynamic nature of these enzymes. In addition, while several CYP isoforms have successfully been crystallized, a crystal structure for a mammalian CYP in a

membrane environment has yet to be resolved. As such, the crystal structures used as the basis for molecular dynamics simulations might not be an accurate representative of the native structure of the enzyme. To the best of my knowledge, there has been no experimental investigation into the role of the membrane on the dynamics of hydrophobic ligand binding to mammalian CYPs.

Phospholipid bilayer nanodiscs are a nanoscale model membrane encircled by two "belt-like" membrane scaffold proteins (MSP) (33,38,39,43,53). Other model membrane systems, such as liposomes, do not prevent the oligomerization of CYPs, which has been shown to affect the steady state turnover kinetics of these enzymes (54,55), and are generally less stable than nanodiscs. By contrast, nanodiscs are able to monomerize membrane proteins due to their relatively small diameter (~ 10 nm), and they are relatively more robust compared to other model membrane systems, allowing them to maintain their structural integrity during such techniques as stopped-flow spectrosocpy. Nanodiscs have seen increased use in studying mammalian CYPs. For example, equilibrium binding of ligands to CYP3A4 were performed using nanodiscs as a model membrane (56). They have been used to investigate the intermediates formed during the CYP19A1-catalyzed formation of estrogens from androgens (57). Increased reproducibility of a high-throughput drug screening method was achieved by incorporating CYP2J2 into nanodiscs (58). Nanodiscs have also found use in probing interactions between cytochrome b5 and CYPs using NMR spectroscopy (59).

In order to investigate the dynamic ligand binding behavior of CYPs in a native-like environment, we have utilized stopped-flow spectroscopy to study CYP3A4 in a phospholipid nanodisc membrane. CYP3A4 is one of the most widely studied human CYP isoforms. Because of its catalytic promiscuity and high expression levels in the liver and intestine, it is able to

catalyze the metabolism of a broad range of structurally diverse substrates and plays a critical role in the metabolism of drugs as well as other endogenous and exogenous substrates (1). Herein we investigate the binding of two structurally diverse ligands to monomeric CYP3A4 in a membrane: bromocriptine (BCT) and cyanide anion ($^{-}$CN) (Fig. 2). BCT is a relatively large (MW: 654.6 g/mol), hydrophobic substrate and has a simple 1:1 binding stoichiometry with CYP3A4 (60,61). I hypothesize that BCT must partition into the membrane in order to bind CYP3A4. By contrast, $^{-}$CN is a small (MW: 26.0 g/mol) and hydrophilic CYP ligand that mimics molecular oxygen in the active site (62). I predict that $^{-}$CN does not require partitioning into the membrane in order to reach the CYP3A4 active site.

2.2 Materials and Methods

2.2.1 Reagents.

1-palmitoyl-2-oleoyl-sn-glycero-3-phosphocholine (POPC) was purchased from Avanti Polar Lipids, Inc. (Alabaster, AL). All other reagents were purchased from Sigma-Aldrich, unless otherwise stated and were used without further purification.

2.2.2 Expression and Purification of CYP3A4.

Recombinant CYP3A4 was expressed as described previously with minor modifications (63,64). Briefly, CYP3A4 was expressed in *E. coli* C41(DE3) cells transformed with pCWOri+ vector encoding ampicillin resistance and CYP3A4 modified with an *N*-terminal truncation and the addition of a C-terminal histidine tag. Cells were lysed by incubating with lysozyme for 4 hours at 4°C and centrifuged at 100,000 x g for 1 hour in order to collect the cell lysate. CYP3A4 was purified with a His60 nickel affinity column (Clontech Laboratories, Inc., CA), followed by purification using a hydroxyapatite column (Bio-Rad Laboratories, Inc., CA). Purified protein

was dialyzed into CYP3A4 storage buffer (100 mM potassium phosphate, 20% glycerol, 1 mM EDTA, 500 μM TCEP, pH 7.4) and stored in 1 mL aliquots at -80°C for future use. Protein concentration was determined using the difference absorbance method of Omura and Sato, with an ε_{450} = 91 $mM^{-1}cm^{-1}$ for the ferrous-CO complex. (65).

2.2.3 Expression and Purification of MSP1D1.

Expression and purification of the membrane scaffold protein MSP1D1 was performed as described previously (41,66). Briefly, MSP1D1 was expressed in E. coli BL21-Gold (DE3) cells transformed using a pET expression vector encoding kanamycin resistance with a C-terminal His tag connected to a TEV protease cleavage site. Cells were lysed using a French pressure cell (Thermo Fisher Scientific, Inc., MA) and centrifuged at 100,000 x g for 1 hour at 4°C in order to collect the cell lysate. The lysate was purified with a His60 nickel affinity column (Clontech Laboratories, Inc., CA), followed by dialysis into MSP storage buffer (50 mM Tris/HCl, 100 mM sodium chloride, 0.5 mM EDTA pH 7.4). Protein concentration was determined by absolute absorbance at 280 nm using an extinction coefficient of ε_{280} = 21430 $M^{-1}cm^{-1}$ and stored in 1 mL aliquots at -80°C.

In order to cleave the scaffold protein for CYP3A4-nanodisc preps, purified MSP1D1 was incubated with ProTEV Plus (Promega Corp., Madison, WI) according to the manufacturer's recommendations. Reaction completeness was verified via SDS-PAGE. Cleaved scaffold protein (MSP1D1-), was purified using a His60 nickel affinity column, dialyzed into MSP storage buffer and concentrated. Protein concentration was determined by absolute absorbance spectroscopy at 280 nm using an extinction coefficient of ε_{280} = 18450 $M^{-1}cm^{-1}$ and stored in 1 mL aliquots at -80°C.

2.2.4 Nanodisc Assembly.

Nanodiscs were assembled as described previously with minor modifications (66). Briefly, POPC and MSP1D1 were mixed in a 65:1 ratio with sodium cholate in disc forming buffer (100 mM potassium phosphate, 50 mM sodium chloride, pH 7.4) and allowed to mix on a nutator for 1 hour at 4°C in order to form mixed micelles. Amberlite XAD-2 resin (Sigma-Aldrich, MO) was subsequently added and the sample was allowed to incubate for an additional 4 hours at 4°C in order to remove cholate and initiate the nanodisc self-assembly process. Resin was removed by passing the sample through a 0.2 μm filter. The nanodisc sample was then spin-concentrated using Centriprep centrifugal filters (EMD Millipore Corporation, MA) and injected onto a Superdex 200 10/300 GL size exclusion column (GE Healthcare Life Sciences, UK) at a flow rate of 0.5 mL/min. Nanodisc-containing fractions were collected, pooled, and concentrated. The empty nanodisc concentration was determined by using absolute absorbance spectroscopy with an extinction coefficient of $\varepsilon_{280} = 42000\ M^{-1}cm^{-1}$.

Incorporation of CYP3A4 into nanodiscs followed the above procedure with minor modifications. Briefly, CYP3A4 was mixed with POPC and the His-tag-cleaved variant of MSP1D1 (MSP1D1-) in a ratio of 0.1:63:1 CYP3A4:POPC:MSP. After incubation for 1 hour at 4°C and subsequent removal of cholate over 4 hours with Amberlite XAD-2 resin, the sample was passed through a 0.2 μm filter and then loaded onto a His60 nickel affinity column pre-equilibrated with disc forming buffer. Samples were washed with 5 column volumes of disc forming buffer in order to remove empty nanodiscs before elution with disc forming buffer containing 300 mM imidazole. The eluant was concentrated and loaded onto a Superdex 200 10/300 GL size exclusion column (GE Healthcare Life Sciences, UK), and the CYP3A4-nanodisc-containing fractions were collected. CYP3A4-nanodisc fractions were buffer-

exchanged and concentrated in order to remove excess imidazole. CYP3A4-nanodisc concentration was determined using the difference absorbance spectrum method of Omura and Sato as described above, with an extinction coefficient of ε_{450} = 91 $mM^{-1}cm^{-1}$ (65). For long-term storage, samples were stored in disc forming buffer containing 10% glycerol.

2.2.5 Equilibrium Binding Titrations.

Absolute absorbance spectroscopy was used to monitor changes in the heme Soret peak as ligand was titrated into enzyme. All equilibrium binding data were collected in dual beam mode using an Aminco DW2a spectrophotometer (Olis, Inc., GA). For CYP3A4, the sample cuvette contained 1.4 μM enzyme in disc forming buffer and the reference cuvette contained an equal volume of buffer. For CYP3A4-NDs, the sample cuvette contained 1.4 μM enzyme in disc forming buffer and the reference cuvette contained an equal concentration of empty POPC nanodiscs in the same buffer. Equal aliquots of ligand were added to both cuvettes, and absorbance spectra were recorded from 350 nm to 700 nm after each addition of ligand. All titrations were carried out at 10°C. Data were baseline-corrected and corrected for the change in volume. Difference spectra were calculated by subtracting the initial spectrum for CYP3A4 or CYP3A4-NDs in the absence of ligand from each subsequent spectra.

All data were fit using IgorPro (Wavemetrics, Inc., OR). For cyanide anion, data were corrected for the amount of ligand that exists in solution as the anionic species after dissolving potassium cyanide (KCN) in buffer using the Henderson-Hasselbalch equation, pH = pKa + log([$^-$CN]/[HCN]). At pH 7.4, the ratio of protonated to anionic cyanide ratio ([$^-$CN]/[HCN]) is 0.000251. In other words, there are theoretically 3981 HCN molecules for every 1 molecule of $^-$CN (the pKa of $^-$CN is 11). Because the total cyanide concentration is equal to the sum of the

concentrations of HCN and $^{-}$CN, and the concentration of HCN is equal to 3981 x [$^{-}$CN], the total cyanide concentration is then the concentration of $^{-}$CN multiplied by 3982. Therefore, the concentration of $^{-}$CN at pH 7.4 can be determined by dividing the total concentration of cyanide in solution ([HCN] + [$^{-}$CN]) by 3982.

To determine the dissociation constant K_D, the peak-to-trough absorbance (ΔAbs) was plotted as a function of cyanide anion concentration and fit to the hyperbolic binding equation:

$$\Delta Abs = \frac{Abs_{max}[L]}{K_D+[L]} \qquad \text{Eq. 1}$$

where ΔAbs is the change in peak-to-trough absorbance, Abs_{max} is the maximum absorbance difference at infinite ligand concentrations, L is the concentration of cyanide anion, and K_D is the spectral dissociation constant.

In the case of bromocriptine, a tight binding CYP3A4 substrate, the free ligand approximation does not hold. Therefore the K_D was determined by plotting the peak-to-trough absorbance as a function of bromocriptine concentration, and the curve was fit to a quadratic binding equation:

$$\Delta Abs = \frac{Abs_{max}(K_D+[E]+[L])-\sqrt{(K_D+[E]+[L])^2-4[E][L]}}{2[E]} \qquad \text{Eq. 2}$$

where E is the total enzyme concentration and all other parameters are the same as in Equation 1. All errors are shown as +/- standard deviation.

2.2.6 Stopped-Flow Spectroscopy.

All stopped-flow experiments were carried out at 10°C using an SX-20 stopped-flow apparatus (Applied Photophysics Ltd., UK). Absorbance mixing experiments utilized a 1:10 mixing setup. A 2.5 mL syringe was loaded with either CYP3A4, CYP3A4-nanodiscs, or empty nanodiscs at

an initial concentration of 0.55 μM, and a 250 μL syringe was loaded with the ligand of interest, either bromocriptine, dissolved in 0.1 N hydrochloric acid (ThermoFisher Scientific, Hampton, NH), or potassium cyanide (dissolved in DFB). After allowing 5 minutes for the syringe contents to equilibrate to temperature, 7 to 12 repeat injections were performed to rapidly mix the two samples. The kinetics of ligand binding to the heme active site was monitored by rapidly collecting full absorbance spectra using a photodiode array detector. Kinetic traces were generated by plotting the absorbance difference between the maximum and minimum wavelength changes as a function of time.

Absorbance dilution experiments were also performed using a 1:10 rapid mixing setup. 5.5 μM CYP3A4 or CYP3A4-nanodiscs were incubated with 250 nM cyanide anion at room temperature for 10 minutes. Samples were then further incubated at 10°C for 15 minutes. Samples were then loaded into the 250 μL syringe and DFB was loaded into the 2.5 mL syringe. The contents of each syringe were then rapidly mixed and full spectrum absorbance data were collected and kinetic traces were generated as described above.

In order to determine the rates of bromocriptine binding to and dissociation from empty nanodiscs, stopped-flow data were collected in the fluorescence mode and the intrinsic fluorescence of bromocriptine was monitored. 0.55 μM empty nanodiscs were loaded into the 2.5 mL syringe (final concentration = 0.5 μM after mixing) and varying concentrations of bromocriptine were loaded into the 250 μL syringe. Samples were rapidly mixed and bromocriptine fluorescence quenching was monitored by setting the excitation wavelength to 325 nm and using a 375 nm emissions cutoff filter. For dissociation experiments, 5 μM nanodiscs were allowed to incubate with 5 μM bromocriptine for 10 minutes at room temperature before cooling for an addition 10 minutes at 10°C. Sample was loaded into a 2.5 mL

syringe and a 250 µL syringe was filled with DFB. The contents of both syringes were rapidly mixed and the recovery of bromocriptine fluorescence was monitored using the same settings as in the fluorescence mixing experiment.

Kinetic parameters were determined by globally fitting experimental data to exponential equations using IgorPro. For absorbance mixing experiments, the change in absorbance (ΔAbs) was fit two a sum of two exponentials:

$$\Delta\text{Abs} = \Delta Abs_0 + A_1(1 - e^{-k_1*(t-t_0)}) + A_2(1 - e^{-k_2*(t-t_0)}) \qquad \text{Eq. 3}$$

where ΔAbs_0 is the absorbance change at time 0, A_1 and A_2 are the magnitudes of the first and second phase of the kinetic trace, respectively, k_1 and k_2 are the observed rates for first and second phase of the kinetic trace, respectively, t is time, and t_0 is the start time of the acquired data. All errors are reported as +/- standard deviation.

Absorbance dilution data were fit to a single exponential equation:

$$\Delta Abs = Plateau + Ae^{-k*(t-t_0)} \qquad \text{Eq. 4}$$

where plateau is the absorbance change at infinite times, A is the magnitude of the reaction, k is the observed reaction rate, and ΔAbs and t_0 are the same as in equation 3.

For fluorescence mixing experiments, the data were fit to a sum of two exponentials:

$$\Delta\text{Fluor} = Plateau + A_1e^{-k_1*(t-t_0)} + A_2e^{-k_2*(t-t_0)} \qquad \text{Eq. 5}$$

where ΔFluor is the change in the fluorescence signal, plateau is the change in fluorescence at inifinite times, and all other parameters are the same as in equation 3.

For fluorescence dilution experiments, the data were fit to a single exponential:

$$\Delta\text{Fluor} = \Delta Fluor_0 + A(1 - e^{-k*(t-t_0)}) \qquad \text{Eq. 6}$$

where ΔFluor is the change in the fluorescence signal, ΔFluor_0 is the initial fluorescence at time 0, and all other parameters are the same as in equation 4.

2.2.7 Kinetic Simulations.

Kinetic simulations were performed using COPASI, a COmplex PAthway SImulator (67). Models were built and tested using the parameters obtained from stopped-flow and equilibrium titration experiments. Simulations were set to run over the same time courses as used in the corresponding stopped-flow experiment. For simplification, it was assumed for the induced-fit models that both steps for ligand binding to the active site contributed equally to the overall absorbance signal.

2.3 Results

2.3.1 Equilibrium Binding Titrations.

In order to determine the binding affinity of the ligand to CYP3A4, absorbance equilibrium binding titrations were carried out with CYP3A4 in buffer or CYP3A4-nanodiscs. The binding of $^{-}$CN to CYP3A4 generates a type-II (low-spin) spectral shift in the heme Soret peak, with a maximum absorbance change at 444 nm and a minimum at 414 nm (Fig. 3a). Absorbance spectra from 350 nm to 700 nm were measured at varying concentrations of $^{-}$CN. A binding isotherm was obtained by plotting the difference in absorbance at 444 nm vs. 417 nm as a function of $^{-}$CN concentration, and was then fit to equation 1 to yield a dissociation constant, K_D, of 0.27 ± 0.01 μM for $^{-}$CN binding to CYP3A4 in buffer (Fig. 3b). Although $^{-}$CN is a tight binding CYP3A4 ligand, ligand depletion from solution is minimal and can safely be ignored because there is an excess of hydrogen cyanide (HCN) in solution that can constantly converted

to the anionic form. Binding of $^{-}$CN to CYP3A4-nanodiscs also exhibits a type-II spectral shift in the heme soret peak, with an absorbance maximum and minimum at 444 nm and 414 nm, respectively (Fig. 3c). Fitting of the corresponding binding isotherm to equation 1 yields a K_D of 0.16 ± 0.01 μM (Fig. 3d). This suggests that the nanodisc membrane induces a conformational change in CYP3A4 that results in tighter binding of $^{-}$CN in the active site compared to in the absence of the membrane.

BCT binding is spectrally distinct from $^{-}$CN binding, causing a type-I (high-spin) spectra shift in the heme soret peak with maximum and minimum absorbance changes at 388 and 419 nm, respectively (Fig. 4a). A plot of this absorbance difference as a function of bromocriptine concentration, followed by fitting to equation 2 resulted in a K_D = 1.37 ± 0.07 μM (Fig. 4b). Upon incorporation of CYP3A4 into nanodiscs, a type-I spectral shift is again observed (Fig. 4c). Plotting of these data and fitting to equation 2 results in a K_D = 1.26 ± 0.09 μM, equivalent to the value obtained in aqueous solution (Fig. 4d).

2.3.2 Cyanide Anion Binding and Dissociation Kinetics to CYP3A4 and CYP3A4-nanodiscs.

The kinetics of $^{-}$CN binding to the CYP3A4 heme active site was monitored using stopped-flow absorbance spectroscopy. Upon rapid mixing of $^{-}$CN with CYP3A4 in DFB, a rapid binding is observed that is best fit by an equation with a sum of two exponentials (Fig. 5a-d). A plot of the k_{obs} values as a function of $^{-}$CN concentration reveals a concentration-dependent process that increases linearly with increasing $^{-}$CN, with rate constant k_1 = 10.5 ± 2.1 μM^{-1} s^{-1} (Fig. 5e). In contrast, a plot of the k_{obs} values for the slow components of each kinetic trace reveal a concentration-independent process with a rate constant k_2 = 1.8 ± 0.2 s^{-1} (Fig. 5e). For all concentrations of cyanide anion used, the fast phase contributed 67.7 ± 4.6% to the kinetic

trace. In order to determine the dissociation rate of $^{-}$CN from CYP3A4, dilution stopped-flow experiments were also performed. In contrast to mixing experiments, dilution experiments were best fit to a single exponential equation, resulting in a dissociation rate constant of k_{off} = 1.40 ± 0.02 s^{-1} (Fig. 6). Using the experimentally-determined rate constant for k_1 and k_{off} results in a calculated K_D of 0.13 ± 0.02 μM. The theoretical k_{off} value from the y-intercept of the k_{obs} plot is 7.8 s^{-1}, which would result in a theoretical K_D of 0.74 μM, much higher than what it observed experimentally. This highlights the greater reliability of the dilution experiment in predicting the rate of dissociation of ligand from the active site, versus using the theoretical dissociation rate from the y-intercept, which can be significantly influenced by slight deviations from perfect linearity in the experimental mixing data. It is possible that the slow phase of the $^{-}$CN binding kinetics (a concentration-independent process) may represent a slow conformational change in the enzyme that may occur prior to or after the ligand has reached the active site.

Similar results were observed when monitoring $^{-}$CN binding to CYP3A4 incorporated into nanodiscs. Rapid mixing of $^{-}$CN with CYP3A4-nanodiscs resulted in a very rapid reaction best fit to a sum of two exponentials (Fig. 7a-d). Interestingly, the fast phase contributes approximately 94.4 ± 1.9% to the kinetic trace when CYP3A4 is in a nanodisc membrane. The rate constants for k_1 and k_2 calculated from the k_{obs} plot are in close agreement with the values determined for $^{-}$CN binding to CYP3A4 in DFB (Fig. 7e and Table 1). Stopped-flow dilution reveals a dissociation rate constant of 2.18 ± 0.03 s^{-1} (Fig. 8), also in good agreement with what was observed for CYP3A4 in DFB, and calculation of a dissociation constant from the experimentally determined on and off rates gives a K_D of 0.22 ± 0.01 μM. Taken together, these data suggest that although incorporation of CYP3A4 into the nanodisc appears to induce a conformational change which alters the relative kinetic contributions from the fast and slow

phases, the overall mechanism of $^{-}$CN binding appears to remain unchanged. Alternatively, the difference in rate constants obtained for CYP3A4-nanodiscs could be due to aggregation of CYP3A4 in DFB vs. the monomeric CYP3A4 in nanodiscs.

Table 1. Experimentally determined parameters for ligand binding to CYP3A4, CYP3A4-nanodiscs, and empty nanodiscs.

Sample	K_D (μM)	k_{off} (s^{-1})	k_1 ($\mu M^{-1} * s^{-1}$)	k_2 (s^{-1})	% Fast
CYP3A4 + $^{-}$CN	0.27 ± 0.01	1.40 ± 0.02	10.5 ± 2.1	1.8 ± 0.2	67.7 ± 4.6
CYP3A4-Nanodisc + $^{-}$CN	0.16 ± 0.01	2.18 ± 0.03	10.0 ± 0.2	2.3 ± 0.4	94.4 ± 1.9
CYP3A4 + BCT	1.37 ± 0.07	N.D.	0.003 ± 0.001	0.016 ± 0.002	37.5 ± 2.8
CYP3A4-Nanodisc + BCT	1.26 ± 0.09	N.D.	0.006 ± 0.001	0.020 ± 0.008	75.6 ± 11.3
Nanodisc + BCT	N.D.	497.0 ± 67.0	327.1 ± 11.2	16.5 ± 5.2	91.0 ± 0.8

2.3.3 Kinetics of Bromocriptine Binding to CYP3A4 and CYP3A4-nanodiscs.

Stopped-flow absorbance spectroscopy was used to monitor BCT binding to the CYP3A4 active site in a similar manner to $^{-}$CN. BCT binding to CYP3A4 in DFB exhibits biphasic kinetics (Fig. 9a-d). However, in contrast to $^{-}$CN binding, BCT binding is a much slower process, not approaching equilibrium until roughly 150 seconds. Plotting k_{obs} for both phases as a function of BCT concentration reveals two phase binding reaction, with a concentration-dependent fast phase and a concentration-independent slow phase (Fig. 9e). Dissociation of BCT from the CYP3A4 active site is a very slow process, and as such I could not determine a rate constant for BCT dissociation from the CYP3A4 active site using stopped-flow dilution experiments. Attempting to use a theoretical dissociation constant from the y-intercept of the k_{obs} plot for k_1 (0.13 ± 0.01 s^{-1}) results in a theoretical K_D of 43.3 ± 13.3 μM, significantly larger than the experimentally measured K_D reported in Table 1. As such, the rate of dissociation of BCT from the CYP3A4 active site cannot be determined with the techniques utilized here, due to a

complex binding mechanism likely taking place, as has been previously suggested (60,68). This is addressed in greater detail in the discussion.

Binding of BCT to CYP3A4-nanodiscs also exhibits biphasic kinetics (Fig. 10a-d). The observed rates are plotted in figure 10e. As was the case with CYP3A4 in DFB, BCT dissociation from CYP3A4-nanodiscs is an extremely slow process and it was not feasible to determine an accurate rate constant for BCT dissociation from the enzyme active site using stopped-flow spectroscopy. Using the theoretical dissociation rate of 0.03 ± 0.01 from the y-intercept of k_1 to calculate a theoretical K_D results in a value of 5.0 ± 2.1 μM, which is not in good agreement with the experimentally determined K_D, therefore this value is unreliable.

2.3.4 Bromocriptine Binding to and Dissociation from the Nanodisc Membrane.

Binding of BCT to the nanodisc membrane was monitored using stopped-flow fluorescence spectroscopy. Although relatively weak compared to other fluorophores, it is possible to monitor the quenching of the intrinsic BCT fluorescence as it interacts with a hydrophobic environment, i.e. the hydrophobic core of the nanodisc membrane. Upon rapid mixing of empty nanodiscs with increasing concentrations of BCT, a biphasic process is observed wherein both the fast and slow phases are concentration-independent (Fig. 11a-c). Fitting to a sum of two exponentials yielded rate constants for the fast and slow phases of 327 ± 11 s^{-1} and 17 ± 5 s^{-1}, respectively (Fig. 11d). This is consistent with two distinct binding modes of BCT to the nanodisc membrane, as has been proposed previously (56).This observed concentration-independence suggests that the overall rate of binding in this concentration range is limited by a non-diffusive process. Unfortunately, we were unable to perform stopped-flow fluorescence experiments at much lower concentrations of BCT as the signal to noise ratio becomes poor at lower ligand concentrations. Dilution experiments were also performed in order

to determine the rate of dissociation of BCT from the nanodisc membrane. BCT dissociation from the nanodisc resulted in monophasic kinetics, indicating that a single process is occurring (Fig. 12). A single off-rate of 492 ± 42 s^{-1} was generated from fitting to a single exponential equation.

2.4 Discussion

Although it is well known that mammalian CYPs are membrane proteins, few studies have attempted to address the mechanism by which hydrophobic drugs access the heme active site. It has always been assumed that for mammalian CYPs, large, hydrophobic drugs can only reach the heme active site through an active site channel that is buried beneath the surface of the membrane. Despite this, little has been done experimentally in order to probe possible routes of substrate binding to mammalian CYPs in a membrane environment. While MD simulations have been performed in order to probe the depth of insertion and topology of mammalian CYPs on a membrane, which have given us a greater initial understanding of the CYP-membrane interaction (26,27), studies such as these ultimately are limited by a few unavoidable caveats. These studies must rely on crystal structures attained in the absence of the membrane, which, as our data suggest, may not be truly representative of the native structures of mammalian CYPs *in vivo*. Epitope mapping, while useful for probing the general topology of mammalian CYPs, may miss other regions of the enzyme that are also exposed to the aqueous solvent, which can lead to the incorrect assignment of buried regions of the enzyme. MD simulations themselves may at times over- or under-predict membrane-protein interactions, depending on how the simulations were performed (e.g. starting position of the enzyme relative to the membrane, model membrane types, etc.). Further experimental studies are therefore

necessary in order to compliment and ultimately refine predictions which are based on molecular dynamics simulations.

Utilizing stopped-flow spectroscopy, we have investigated the mechanism of binding for $^{-}$CN and BCT, two structurally distinct ligands with contrasting aqueous solubility. $^{-}$CN is a small, hydrophilic ligand which has the ability to form interactions in the CYP active site similar to molecular oxygen, making it a useful O_2 mimetic, whereas BCT is a large, hydrophobic substrate of CYP3A4. Based on the hydrophobic substrate binding hypothesis, it was proposed that BCT would undergo a necessary partitioning into the membrane in order to reach the CYP3A4 active site whereas CN would be able to bind directly from aqueous solution. The results of our equilibrium and kinetic experiments are summarized in Table 1.

In order to evaluate the stopped-flow spectroscopy results for $^{-}$CN, it is necessary to recall the two simplest mechanisms of ligand binding for a biphasic process: conformational selection (Scheme 1) and induced-fit (Scheme 2). In the conformational selection mechanism, CYP3A4 exists in an equilibrium between what we are referring to here as either a "closed" or an "open" conformer, in the absence of ligand. Assuming that $^{-}$CN can only bind to the "open" conformer, the fast phase monitored by absorbance would then correspond to $^{-}$CN binding to CYP3A4 in a concentration-dependent manner in the first step, and the slow phase would correspond to a conformational switch from "closed" to "open," a process which would occur independently of $^{-}$CN concentration. By contrast, in the induced-fit mechanism, it is assumed that the enzyme will initially exist as single population which is able to bind $^{-}$CN in a concentration-dependent manner. Binding of $^{-}$CN in the CYP3A4 active site will then induce a conformational change in the enzyme. Therefore, in the induced-fit mechanism, the fast phase is assumed to

correspond to the initial $^{-}$CN binding event, and the slow phase would then correspond to a ligand-induced conformational change.

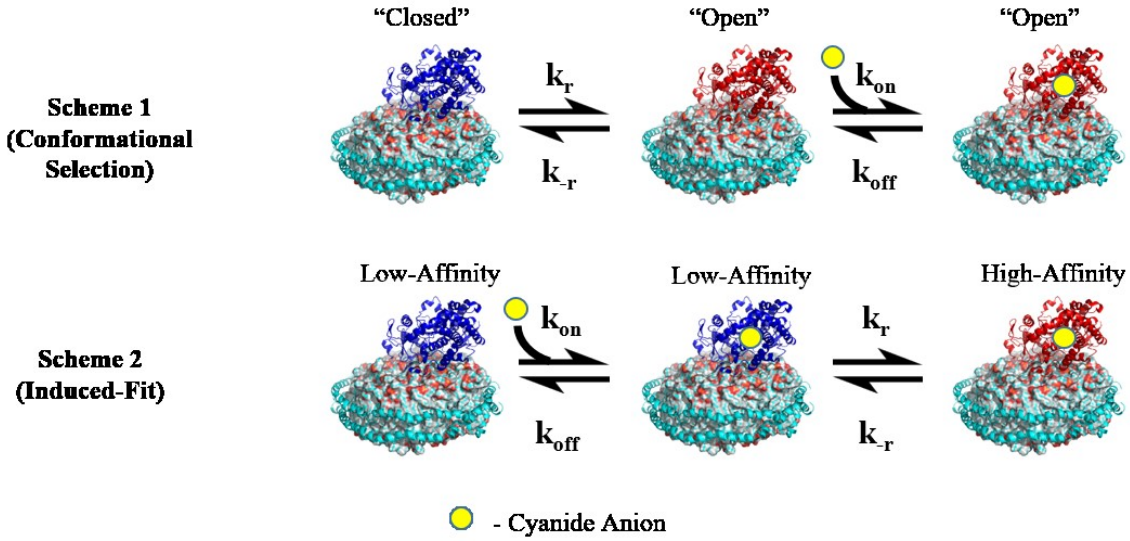

Studies carried out by Vogt and coworkers have provided a better understanding of the kinetic properties of the induced-fit and conformational selection mechanisms (69). A key finding that was demonstrated is that while the slow phase rate of the conformational selection mechanism can either increase, decrease, or remain unchanged with increasing ligand concentration, the slow phase rate of the induced-fit model will increase with increasing ligand. In other words, a slow phase rate that either remains unchanged or decreases with increasing ligand is strong evidence of a conformational selection mechanism. However, because both the conformational selection and induced-fit mechanisms can display an increasing slow phase rate with increasing ligand concentration, it becomes much more difficult to prove that ligand binding is proceeding via an induced-fit mechanism.

The kinetic behavior of $^{-}$CN active site binding remains unchanged upon incorporation of CYP3A4 into a nanodisc membrane, as expected if the channel being utilized is near the cytosol-

exposed surface of the enzyme. It is interesting to note that upon incorporation into a nanodisc we observed a ~30% increase in the fast fraction of the binding process across all $^{-}$CN concentration used, suggesting that the nanodisc membrane is in some way facilitating the binding process, likely by inducing a conformational change in the ligand-free enzyme. The kinetics of $^{-}$CN binding to both CYP3A4 and CYP3A4-nanodiscs have an apparent concentration-independent slow phase (Fig. 5 and Fig. 7). Recall that a concentration-independent slow phase is likely indicative of a conformational selection mechanism. The theoretical K_D calculated from the fast on-rate from mixing experiments and the off-rate from dilution experiments is ~0.17 μM for CYP3A4 in DFB and ~0.22 μM for CYP3A4 in nanodiscs. This is in good agreement with the experimentally determined values (Table 1), suggesting that $^{-}$CN binds to CYP3A4 via a conformational selection mechanism (Scheme 1).

Kinetic simulations were performed in order to distinguish between these two possible models and to predict theoretical rate constants for the slow step. A simple conformational selection model for $^{-}$CN binding to CYP3A4 is shown in Scheme 1. In order to simulate the conformational selection model, the experimentally determined k_{fast} was assumed to correspond to the binding of $^{-}$CN to the "open" conformer of CYP3A4. Because the observed k_{slow} rate was independent of $^{-}$CN concentration, this was assigned to the forward conformational change relaxation rate, k_r ("closed" to "open"). Assuming that the fraction of the fast and slow phases corresponds to the relative initial concentrations of the enzyme conformers, and under the assumption that the observed slow phase is equal to the rate of the forward relaxation, k_r, the theoretical reverse relaxation rate k_{-r} can be calculated using the theoretical initial concentrations of the "open" and "closed" conformers. Doing so results in a $k_{-r} = 1.1\ s^{-1}$ for CYP3A4 in DFB and a $k_{-r} = 0.20\ s^{-1}$ for CYP3A4-nanodiscs (Table 2). As can be seen from Fig. 13, the

conformational selection model agrees well with the experimental data, and this mechanism is consistent with what has been proposed previously by others (54). Therefore, it is proposed for a conformational selection mechanism that, in addition to opening of the $^{-}$CN channel, the membrane promotes the "open" conformer, which is reflected by an increase in the forward relaxation rate and a simultaneous decrease in the reverse relaxation rate.

Simulations were also performed using an induced-fit mechanism in an attempt to model the experimental data (Scheme 2 and Fig. 14). Recall that stopped-flow dilution experiments resulted in a monophasic kinetic trace. As such, it is necessary to assume that the experimentally measured off-rate corresponds to the off-rate for the first step, k_{off}, and that the reverse rate for the second step is greater than or equal to that of the first step ($k_{-r} \geq k_{off}$). Additionally, the experimentally observed k_{slow} must be equal to the sum of k_r^L and k_{-r}^L in the induced-fit model (69). It is also necessarily assumed that the experimentally measured K_D represents the K_D of the overall binding mechanism (ligand binding followed by a ligand-induced conformational change). The experimentally determined k_{fast} was assigned as the rate of initial binding of $^{-}$CN to the CYP3A4 active site. When performing simulations under these conditions, it is observed that this model is less accurate overall in predicting the experimental data. For CYP3A4 in DFB, while the predicted rates mimic the experimentally observed rates relatively well, there is a large discrepancy between the predicted and observed fast fraction (% fast) for the kinetic traces. This makes much it less likely that $^{-}$CN binding to CYP3A4 occurs via an induced-fit mechanism. While a mixed conformational selection/induced-fit mechanism cannot be completely dismissed, it is likely that even in such a case, the conformational selection mechanism dominates the overall binding process. As mentioned previously, $^{-}$CN can serve as a useful mimetic of O_2 in the

active site. Thus, the mechanism of $^{-}$CN binding may provide clues as to the mechanism of O_2 binding to the CYP3A4 active site.

Table 2. Theoretical CYP3A4 Relaxation Rates for $^{-}$CN Binding via Alternate Mechanisms

	Conformational Selection			**Induced-Fit**		
Sample	k_r (s^{-1})	k_{-r} (s^{-1})	% Fast Fraction	k_r (s^{-1})	k_{-r} (s^{-1})	% Fast Fraction
CYP3A4	1.8	1.1	62	0.9	1.4	99
CYP3A4-ND	2.3	0.2	92	1.1	0.8	98

Binding of BCT to the CYP3A4 active site is a very slow and biphasic process. The k_{obs} plot for the absorbance kinetic traces suggests that for both CYP3A4 in buffer and CYP3A4-nanodiscs, the observed rate of the fast phase is apparently increasing with increased ligand concentration, whereas the slow phase appears to remain relatively constant. For both phases, the dissociation constant calculated using the theoretical off-rate from the k_{obs} plot is not in agreement with the experimentally determined value, suggesting a more complex binding mechanism for BCT relative to $^{-}$CN, as has been suggested previously by others (60,68).

Interestingly, the kinetics of BCT binding to the CYP3A4 active site remain largely unchanged upon incorporation of the enzyme into a nanodisc membrane, perhaps suggesting that BCT binding is proceeding via the same or an identical mechanism in both cases. The changes in the relative contributions of the fast phase for the absorbance measurements highlights how nanodiscs alter the kinetics of ligand binding to CYP3A4, similar to what was observed for $^{-}$CN binding (Table 1). However, it remains unclear if this is a result of CYP-membrane interactions or monomerization of the enzyme, or both. It is notable that in the BCT concentration range used, binding to the nanodiscs occurs independently of concentration. Work done by Denisov and coworkers has suggested the existence of a boundary layer of lipid within the nanodisc,

perhaps adjacent to the encircling membrane scaffold proteins (53). As noted earlier, BCT binding to empty nanodiscs exhibited biphasic kinetics (Fig. 11). Considering that the rate of these binding events remain unchanged at the BCT concentrations utilized, a possible explanation for the biphasic nature of the reaction is that the observed fast and slow rates may be representative of the intrinsic rates of BCT partitioning into the central region of the membrane and the putative boundary layer, respectively. This interconversion is apparently rate-limiting for BCT binding to the membrane at the concentrations used. BCT may be forming an encounter complex with the nanodisc membrane at a rate greater than the fluorescence-observed rate.

Despite the observation that the rate of BCT binding to the nanodisc membrane remains constant in the concentration range investigated, a concentration-dependence was observed in the fast phase for BCT binding to the CYP3A4 active site as monitored by absorbance stopped-flow experiments (Fig. 9 and Fig. 10). Assuming that previously proposed models of BCT binding to CYP3A4 are accurate, this apparent concentration-dependence may be indicative of an induced-fit mechanism, where BCT first interacts with CYP3A4 to form an initial-encounter complex in a concentration-dependent manner, prior to entry into the active site (Scheme 3) (60,68). The hydrophobic substrate binding hypothesis suggests that a relatively large and hydrophobic drug such as BCT may only reach the CYP3A4 active site via partitioning through the membrane, i.e., no other pathways exist for hydrophobic drug entry into the active site where membrane partitioning is not required (Scheme 4). My experimental results do not suggest that BCT binds to CYP3A4 via the mechanism in scheme 4. At the ligand concentrations utilized in these experiments, the process of BCT partitioning into the membrane has become saturated. This would have the effect of preventing all subsequent steps in the binding reaction from exhibiting a dependence upon concentration at the BCT concentrations used here. However, I clearly

observed a concentration-dependence in the fast phase of BCT binding to CYP3A4 by stopped-flow absorbance measurements, indicating that the ligand must be accessing CYP3A4 via a route that does not involve obligate membrane partitioning. Furthermore, BCT dissociation from the nanodisc membrane was unexpectedly fast ($497 \pm 67\ s^{-1}$). Due to this rapid dissociation from the nanodisc, if BCT were required to partition into the nanodisc membrane in order to bind CYP3A4, a much slower active site binding rate would be expected for CYP3A4-nanodiscs, relative to CYP3A4 in DFB. However, the rates of BCT binding to CYP3A4 in nanodiscs and DFB (as measured by stopped-flow absorbance spectroscopy) were identical, suggesting that the mechanism of BCT binding had not been significantly altered by the membrane, and that the mechanism is unlikely to require BCT partitioning into the membrane, regardless if BCT binding to the CYP3A4 active site occurred via induced-fit or conformational selection. Even in a case where BCT accumulates within the membrane prior to interacting with CYP3A4, the rapid dissociation of BCT from the nanodisc membrane would prevent accumulation of the ligand at the concentrations used here, and a concentration-dependence should not be observed. It should be noted that we cannot exclude the possibility that there are other routes of BCT entry into the CYP3A4 active site in which ligand partitioning into the membrane is a strictly required event. For instance, there could potentially be two or more CYP3A4 active site channels that BCT could utilize, with at least one of them facing the membrane, while another is oriented towards the cytosol. Additionally, this observation may only hold for BCT; it is still possible that other hydrophobic drugs may obey the strict definition of the hydrophobic substrate binding hypothesis.

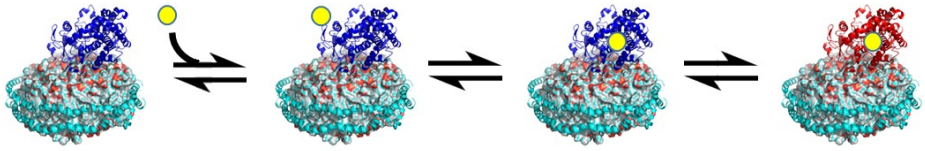

Scheme 3.
(Direct Binding to CYP3A4)

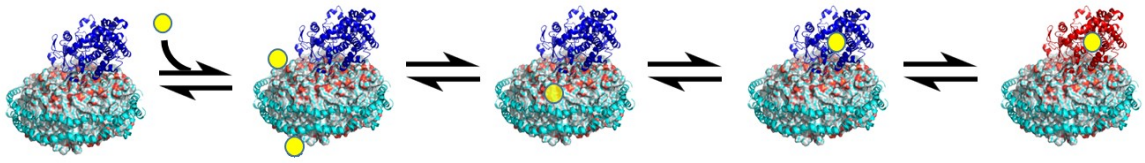

- Bromocriptine

Scheme 4.
(Hydrophobic Substrate Binding Hypothesis)

Nevertheless, this result is unexpected. If the region proximal to the F'/G' and B/C loops is indeed the only location whereby BCT can gain access into the buried CYP active site, then these data perhaps are suggesting that CYP3A4 may not be as deeply embedded within the membrane as previously thought. Alternatively, separate cytosol-exposed channels may exist that cannot be captured by MD simulations based on the currently available CYP3A4 crystal structures. This will remain unclear until such time as structures of mammalian CYPs in a membrane-environment can be attained. Considering the rapid rate of dissociation of BCT from the nanodisc membrane, the CYP-membrane complex may function such that a hydrophobic substrate is rapidly recruited to the membrane. Rapid release from the membrane may then follow, allowing for timely metabolism of the substrate by the local CYP. In this way, the membrane may be acting to funnel hydrophobic substrates to mammalian CYPs without requiring ligand partitioning into the membrane in order to reach the CYP active site. This could

potentially be modified by factors such as membrane fluidity or hydrophobicity of the ligand, and these factors should be investigated further.

2.5 Conclusion

Utilizing phospholipid bilayer nanodiscs as a model membrane system, it has been demonstrated that while the membrane alters the relative populations of different CYP3A4 conformers, the binding mechanisms of CN and BCT remain unaffected. CN binding is explained well by a simple conformational switching mechanism, whereas BCT binding is a more complex process. In the case of BCT, both binding to and dissociation from the nanodisc membrane are rapid processes. However, it appears that this ligand does not obey the hydrophobic substrate binding hypothesis and does not require partitioning into the membrane in order to bind the CYP3A4 active site. While it remains unclear whether this holds for other hydrophobic substrates of CYP3A4, the rapid association and dissociation of BCT from the nanodisc membrane suggests that the membrane may serve as a 'sink' to recruit certain hydrophobic substrates into closer proximity of mammalian CYPs, followed by rapid ligand dissociation from the membrane so that it may begin to interact with and be metabolized by various CYPs. This process may be affected by lipid composition and could potentially influence the substrate-selectivity of various CYP isoforms.

2.6 Figures

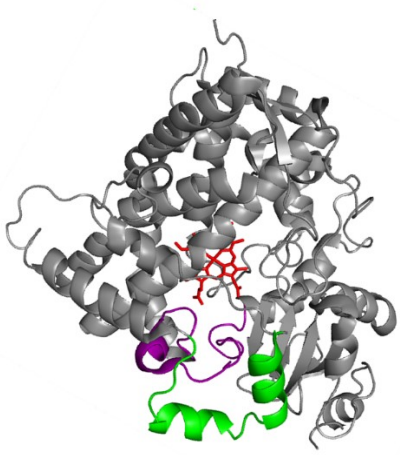

Figure 1. Crystal structure of CYP3A4 (PDB: 1TQN). The buried heme is highlighted in red, the F'/G' loop is highlighted in green, and the B/C loop is highlighted in purple. It is believed that the F'/G' loop and the B/C loop may exist in contact with the membrane *in vivo*.

a.

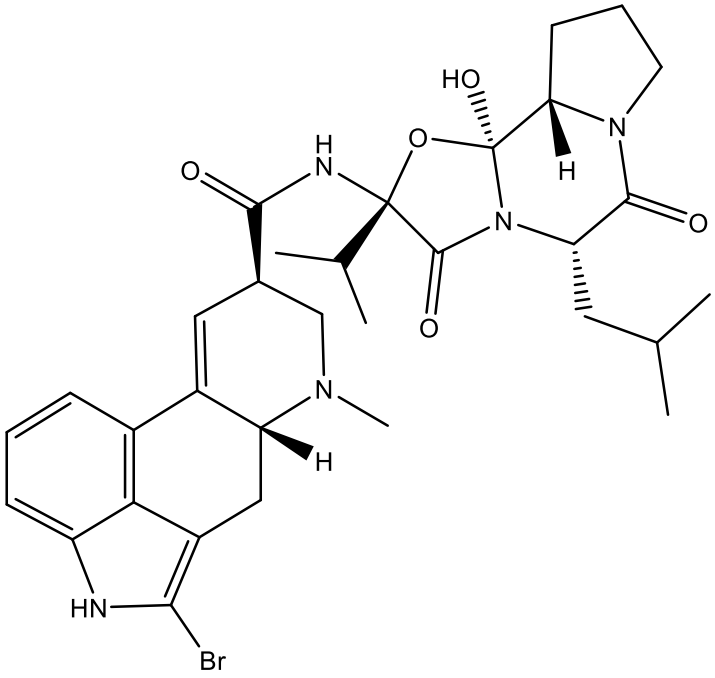

Bromocriptine (BCT)

b.

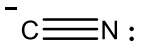

Cyanide Anion ($^{-}$CN)

Figure 2. The chemical structures for bromocriptine (a), a ligand which induces a 'high-spin' state in CYP3A4, and cyanide anion (b), a ligand which induces a 'low-spin' state in CYP3A4.

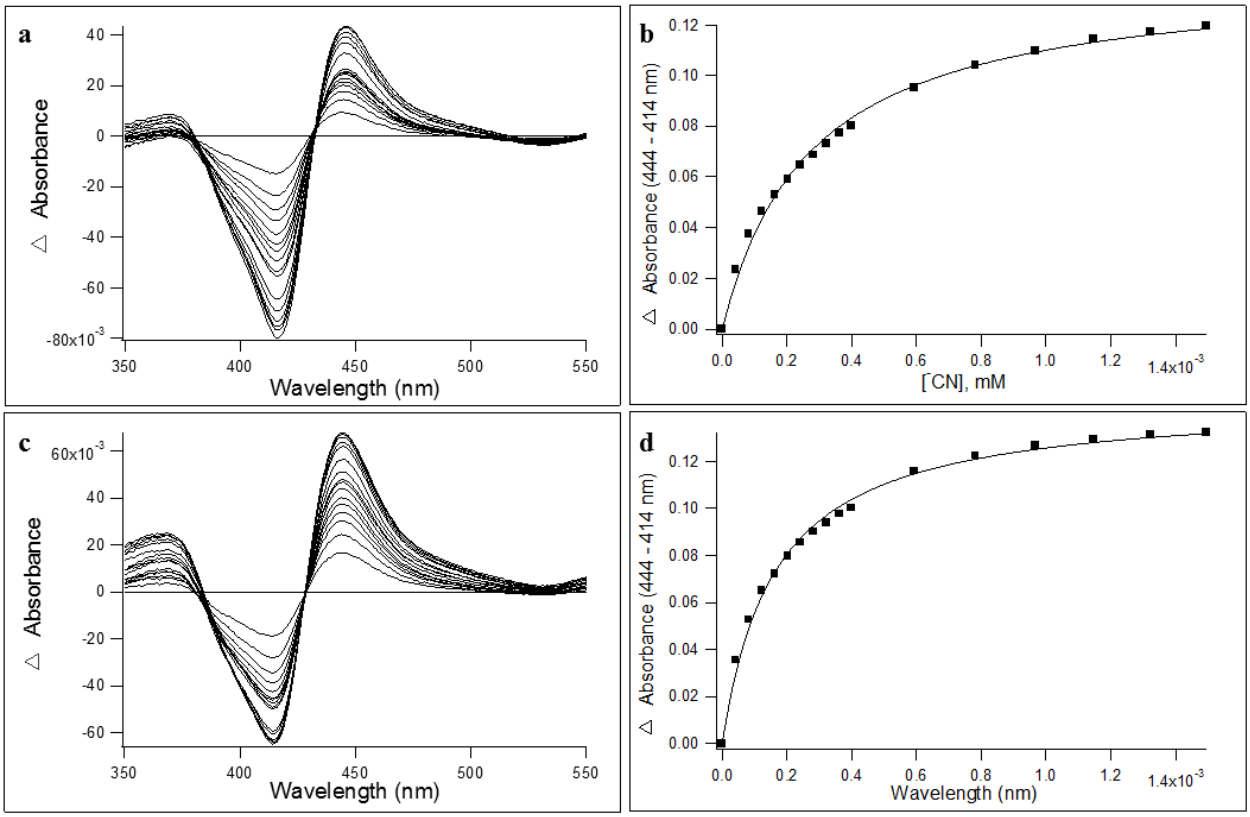

Figure 3. Difference absorbance spectra for $^{-}$CN binding to CYP3A4 in DFB (a) and CYP3A4-nanodiscs (c). Corresponding binding isotherms are shown for CYP3A4 in DFB (b) and CYP3A4-nanodiscs (d). Solid lines in binding isotherms are fits to equation 1.

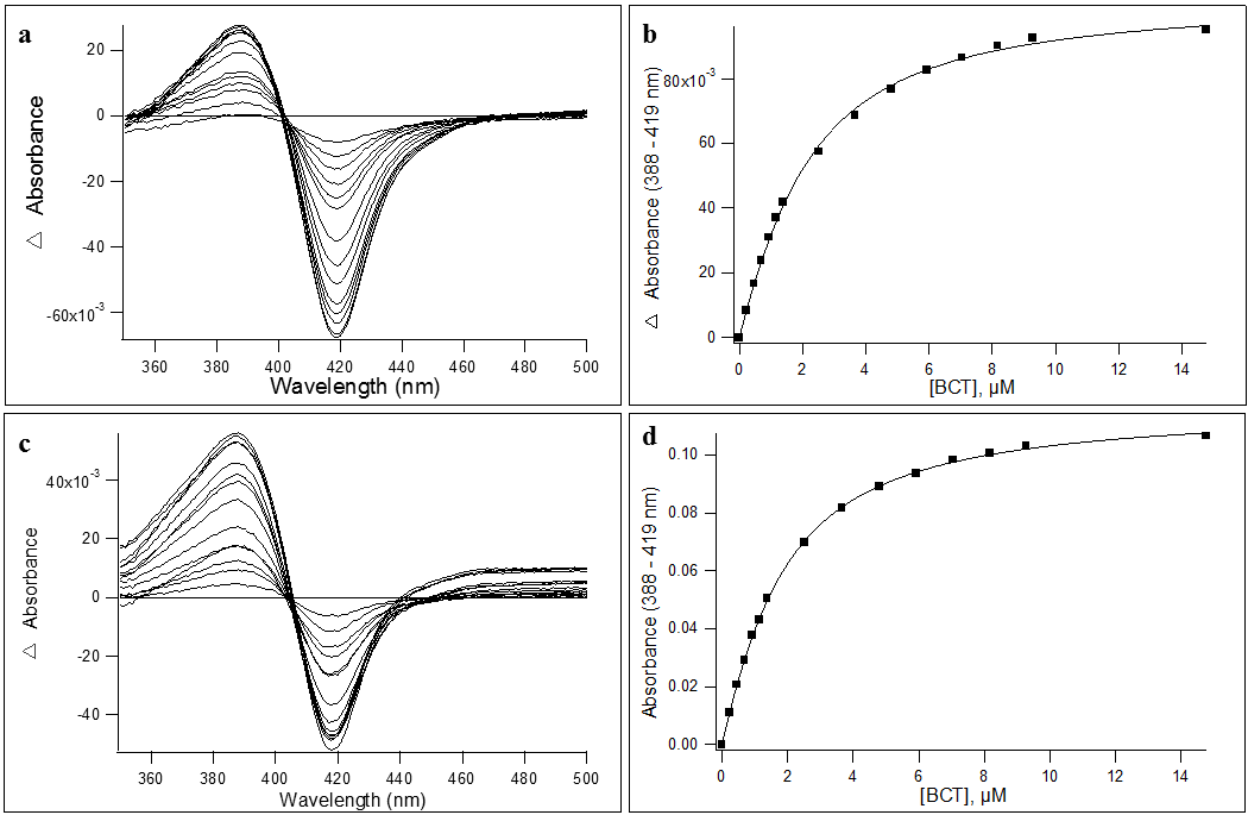

Figure 4. Difference absorbance spectra for BCT binding to CYP3A4 in DFB (a) and CYP3A4-nanodiscs (c). Corresponding binding isotherms are shown on the right for CYP3A4 in DFB (b) and CYP3A4-nanodiscs (d). Solid lines in binding isotherms are fits to equation 2.

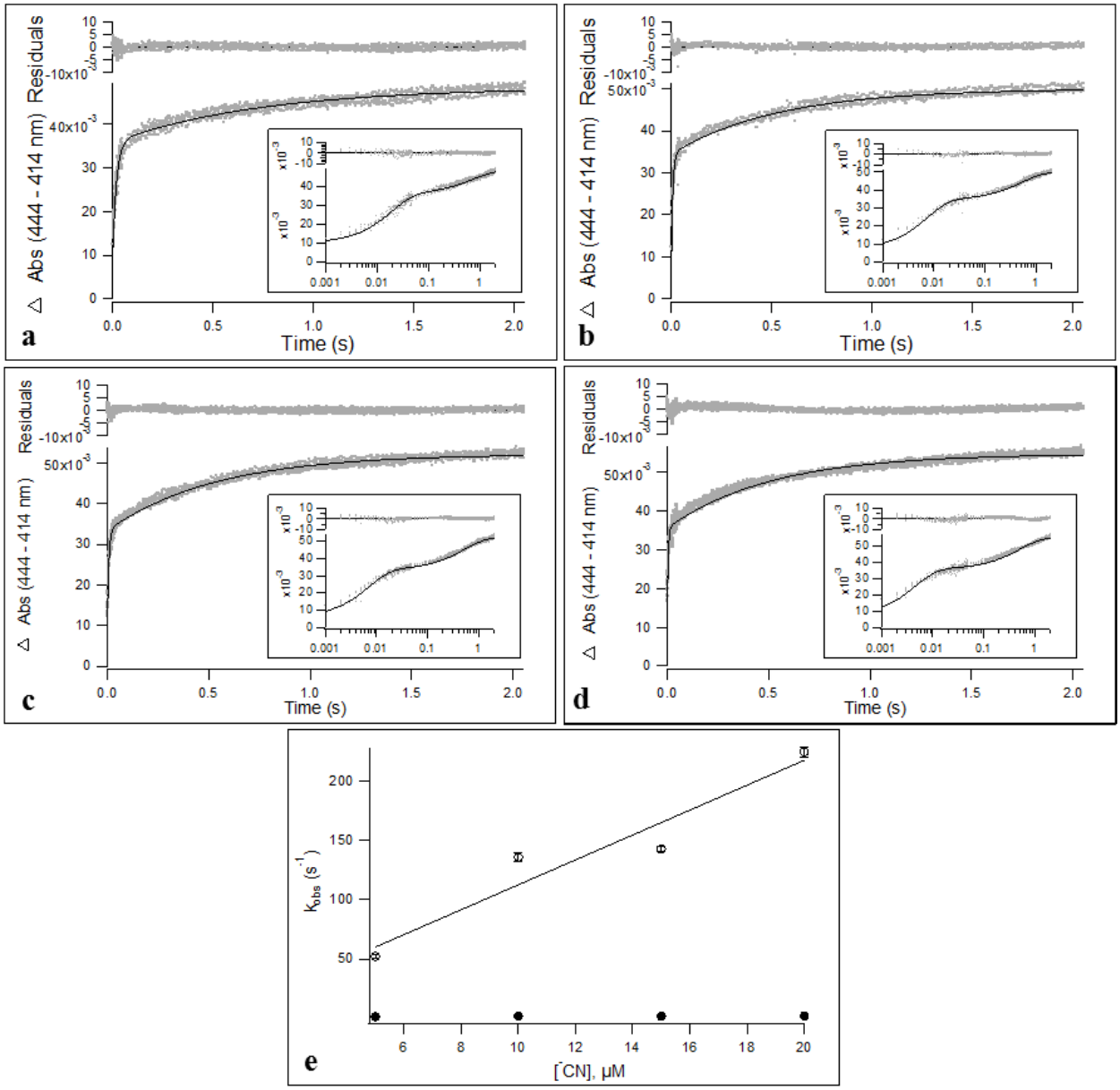

Figure 5. Kinetic traces and fit residuals for CN binding to CYP3A4 in DFB. CYP3A4 was mixed with 5 µM (a), 10 µM (b), 15 µM (c), or 20 µM CN (d). Solid lines represent the fits of the data to equation 4. (Inset: kinetic traces plotted on a logarithmic timescale). e) The resulting k_{obs} plot for the first phase (open circles) and second phase (closed circles). Error values for each concentration after fitting to equation 4 were minimal.

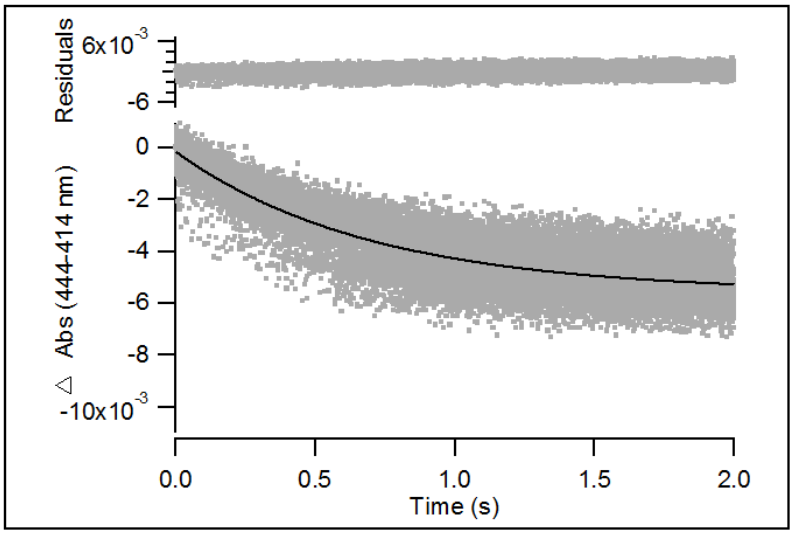

Figure 6. Repeat injections from stopped-flow dilution experiments for the dissociation of $^{-}$CN from CYP3A4 in DFB. The solid line is the resulting global fit of the data to equation 3.

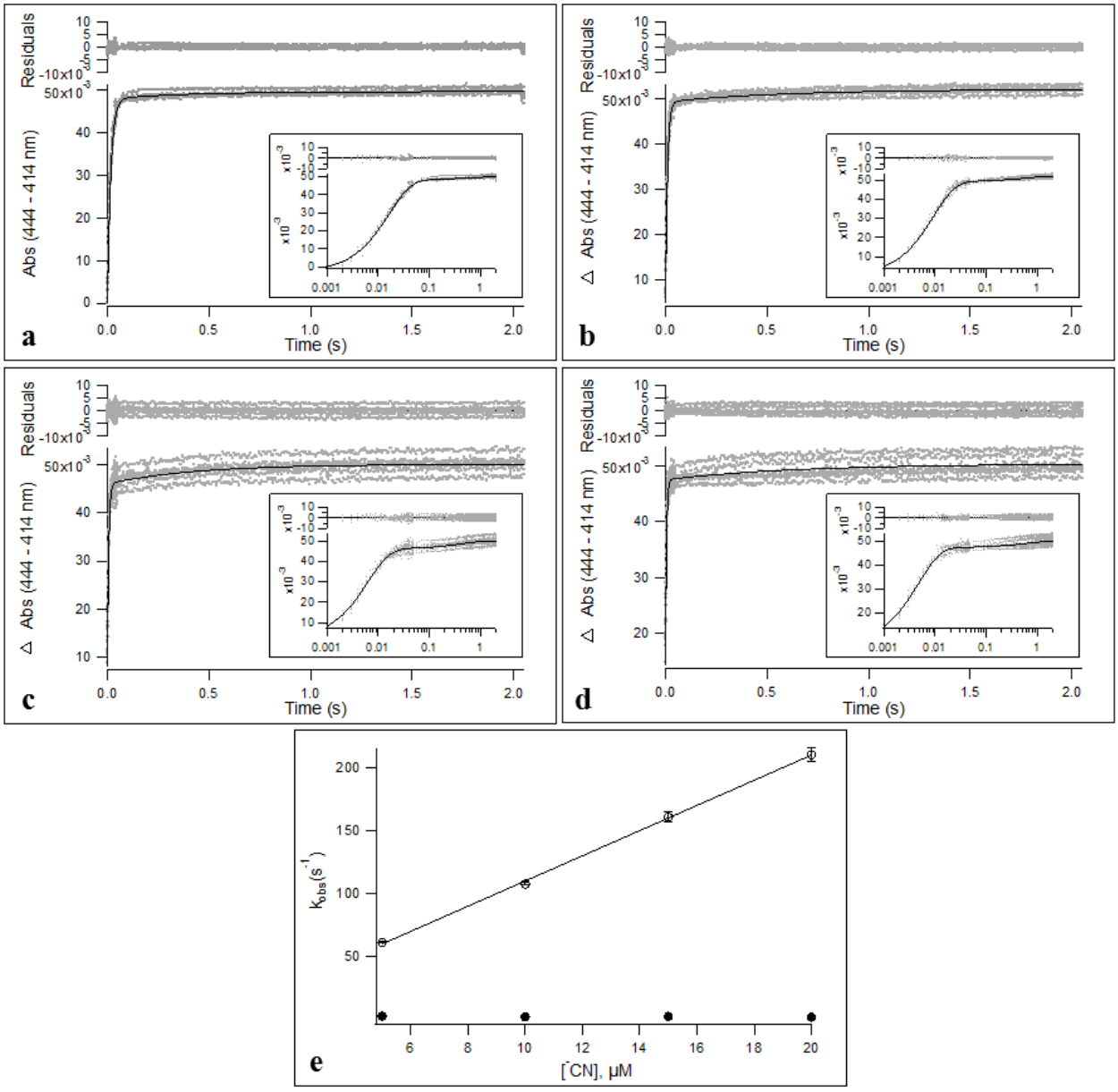

Figure 7. Kinetic traces and fit residuals for $^{-}$CN binding to CYP3A4-nanodiscs. CYP3A4-nanodiscs were mixed with 5 μM (a), 10 μM (b), 15 μM (c), or 20 μM $^{-}$CN (d). Solid lines represent the fits of the data to equation 4. (Inset: kinetic traces plotted on a logarithmic timescale). e) The resulting k_{obs} plot for the first phase (open circles) and second phase (closed circles). Error values for each concentration after fitting to equation 4 were minimal.

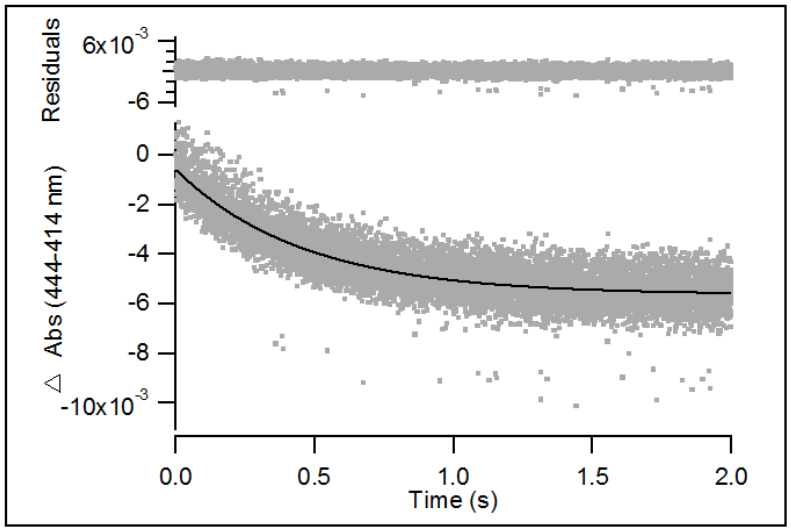

Figure 8. Kinetic traces from stopped-flow dilution experiments of CYP3A4-nanodiscs pre-incubated with $^{-}$CN. The solid line is the resulting global fit of the data to equation 3.

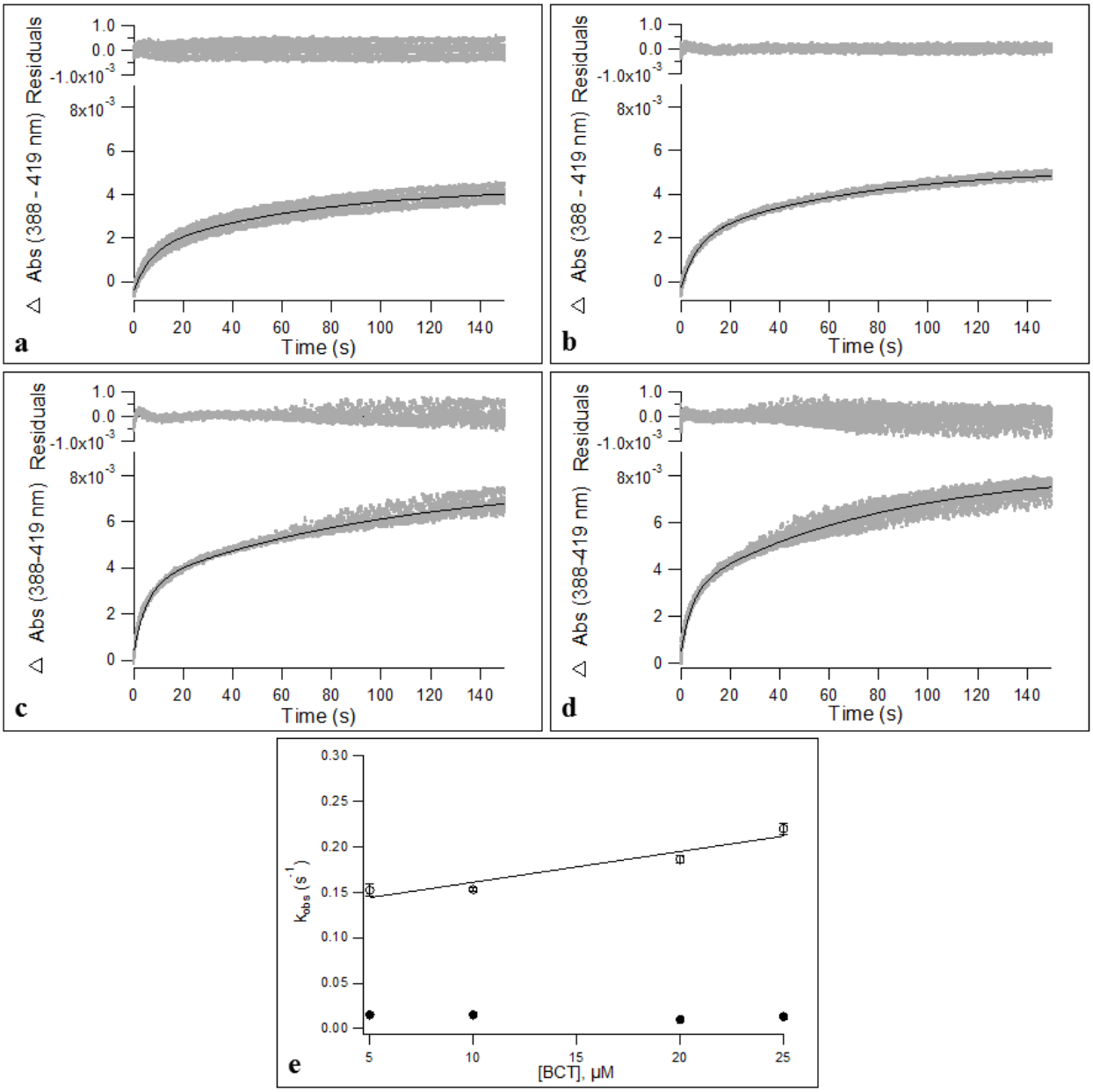

Figure 9. Kinetic traces and fit residuals for BCT binding to CYP3A4 in DFB. CYP3A4 were mixed with 5 μM (a), 10 μM (b), 20 μM (c), or 25 μM BCT (d). Solid lines represent the fits of the data to equation 4. e) The resulting k_{obs} plot for the fast phase (open squares) and slow phase (closed squares). Error values for each concentration after fitting to equation 4 were minimal.

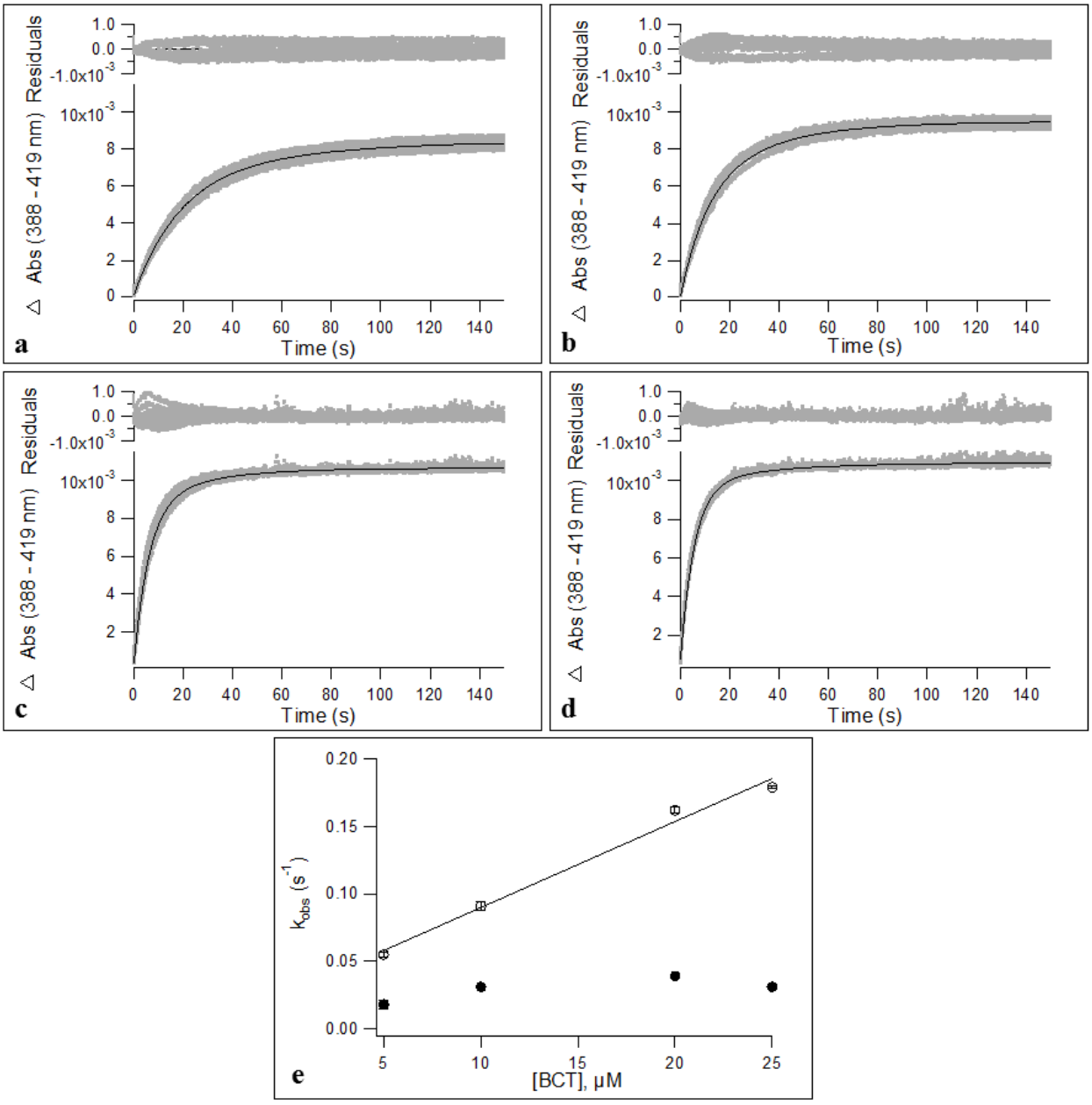

Figure 10. Kinetic traces and fit residuals for BCT binding to CYP3A4-nanodiscs. CYP3A4-nanodiscs were mixed with 5 µM (a), 10 µM (b), 20 µM (c), or 25 µM BCT (d). Solid lines represent the fits of the data to equation 4. e) The resulting k_{obs} plot for the fast phase (open squares) and slow phase (closed squares). Error values for each concentration after fitting to equation 4 were minimal.

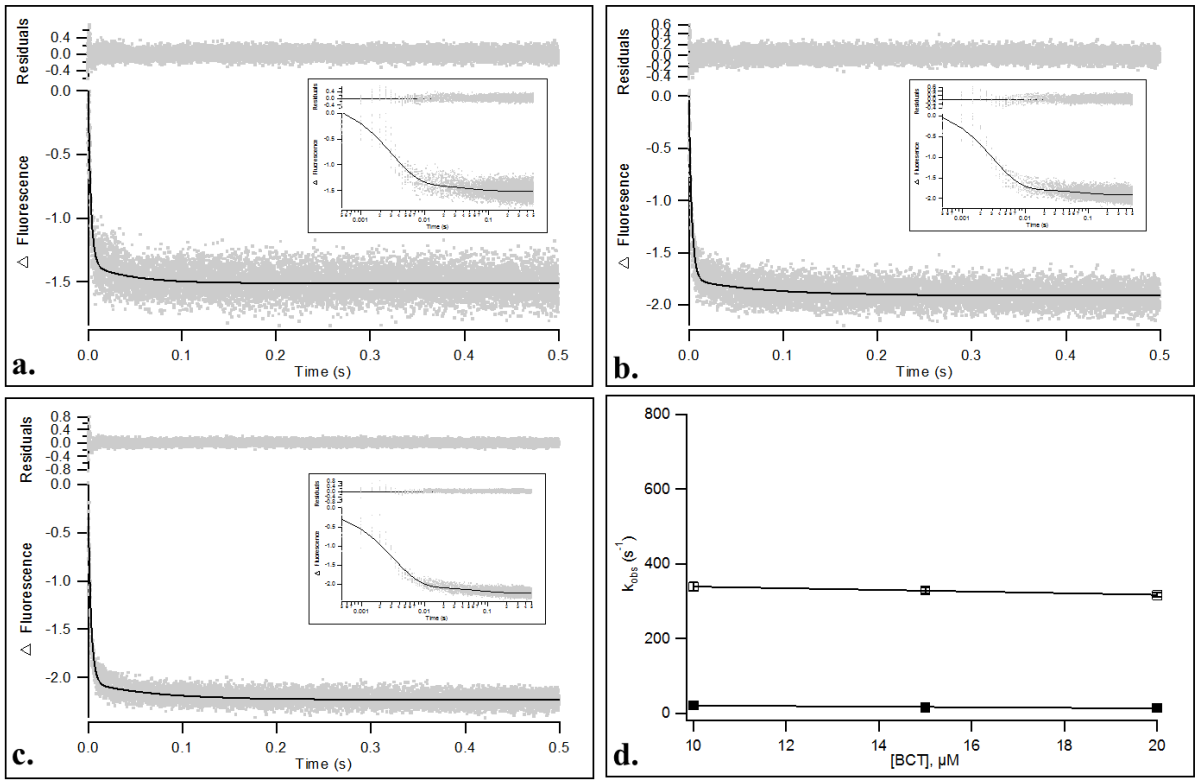

Figure 11. Kinetic traces for the fluorescence quenching of 10 μM (a), 15 μM (b), and 20 μM (c) BCT upon rapid mixing with empty nanodiscs. (d) The k_{obs} plot for the fast phase (open squares) and the slow phase (closed squares) after fitting to equation 4.

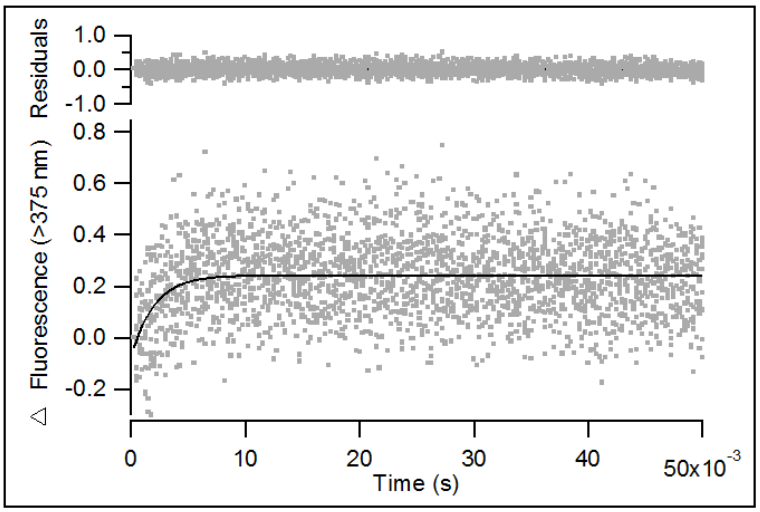

Figure 12. The dissociation of BCT from empty nanodiscs exhibited monophasic kinetics, as monitored by stopped-flow spectroscopy. The solid line represents the global fit of the data to equation 3 and fit residuals are shown at the top of the figure.

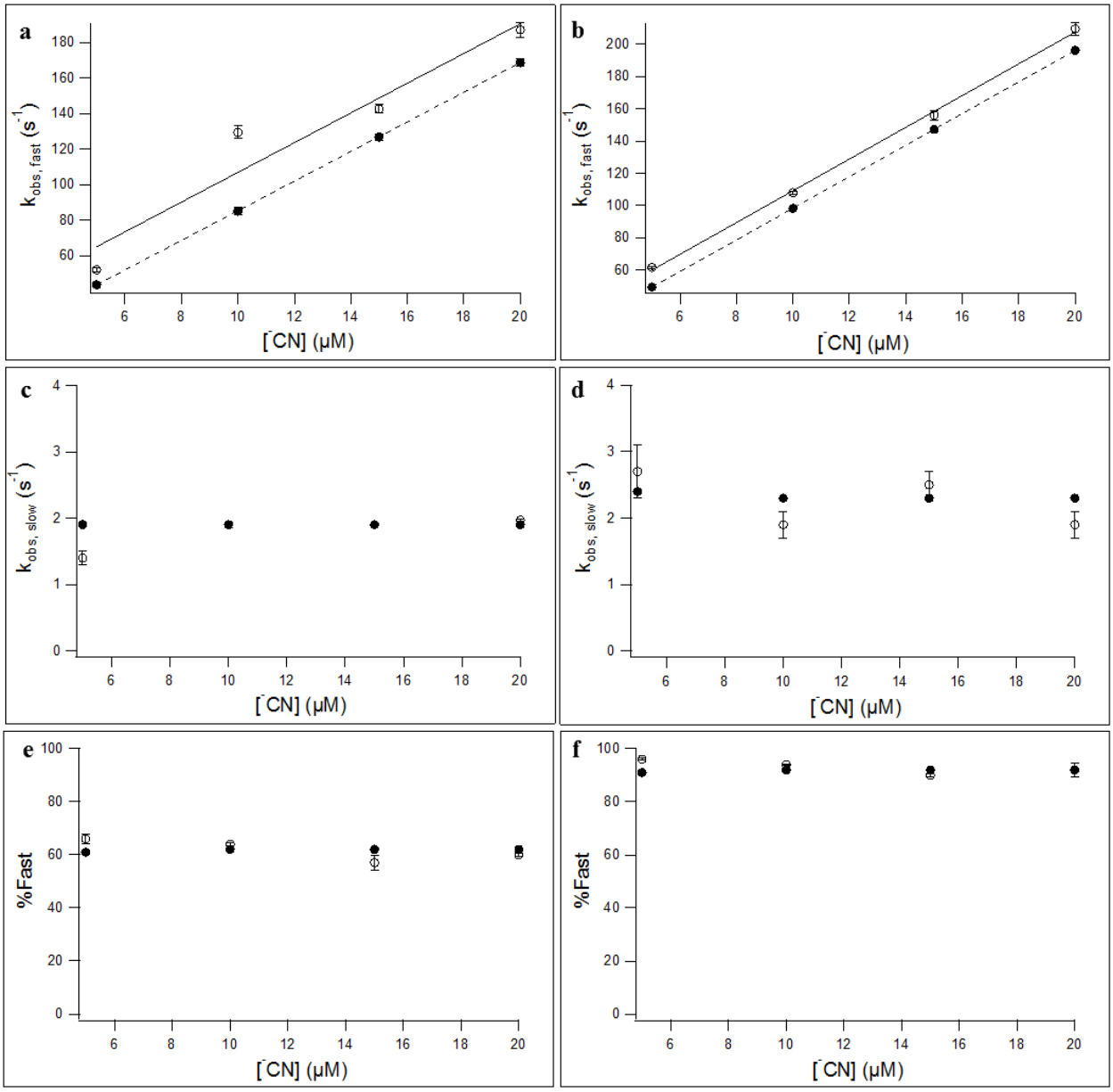

Figure 13. Comparison of experimental parameters (open squares) with simulated parameters (closed squares) for $^{-}$CN binding to CYP3A4 utilizing scheme 1. Comparisons for the fast phase, the slow phase, and the percent contribution of the fast phase for $^{-}$CN binding CYP3A4 in DFB are shown in a, c, and e, respectively. Comparisons for the fast phase, the slow phase, and the percent contribution of the fast phase for $^{-}$CN binding to CYP3A4-nanodiscs are shown in b, d, and f, respectively.

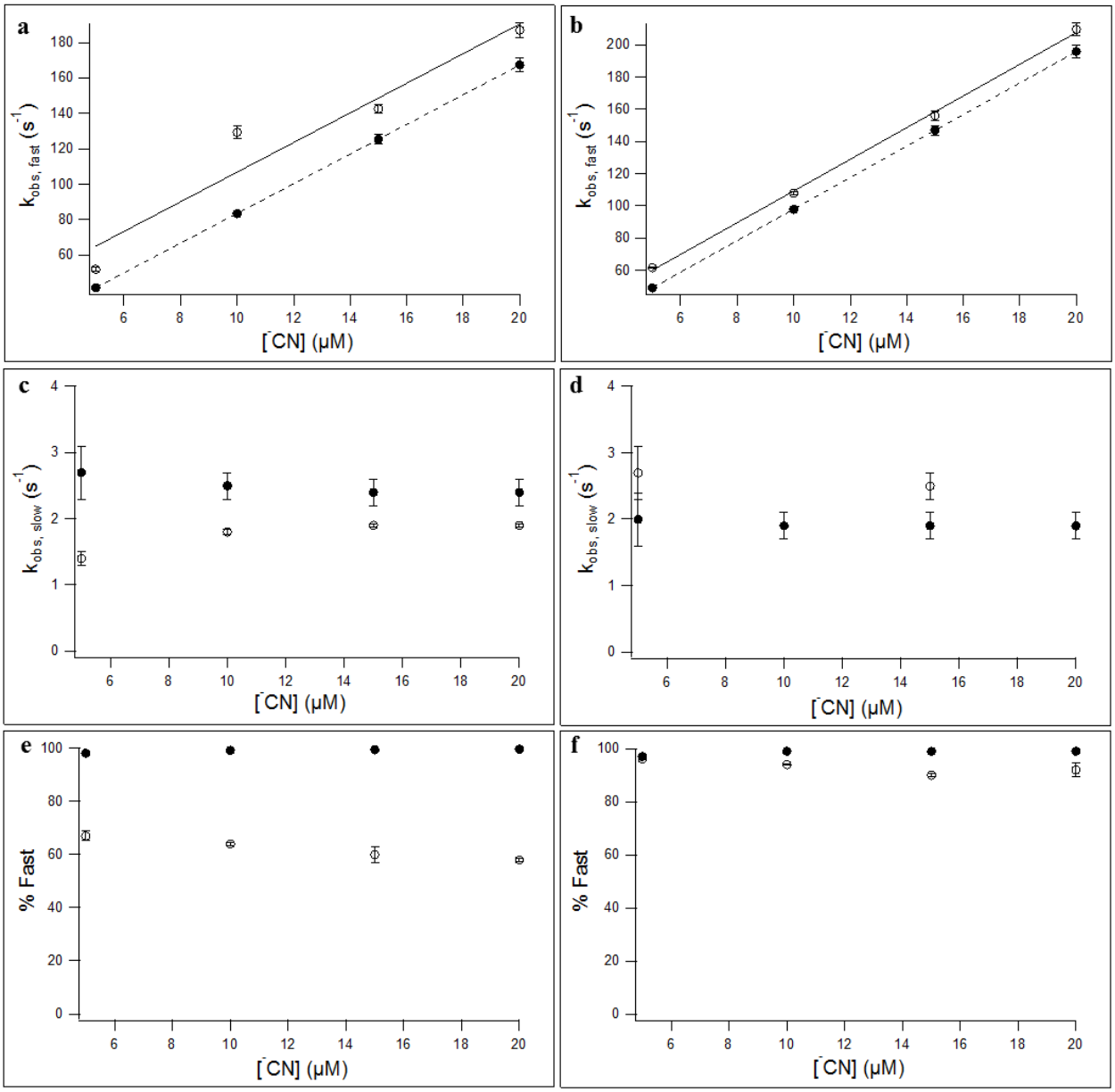

Figure 14. Comparison of experimental parameters (open squares) with simulated parameters (closed squares) for $^{-}$CN binding to CYP3A4 utilizing scheme 1. Comparisons for the fast phase, the slow phase, and the percent contribution of the fast phase for $^{-}$CN binding CYP3A4 in DFB are shown in a, c, and e, respectively. Comparisons for the fast phase, the slow phase, and the percent contribution of the fast phase for $^{-}$CN binding to CYP3A4-nanodiscs are shown in b, d, and f, respectively.

Chapter 3

Thermal Unfolding of Cytochrome P450 3A4 in Nanodiscs

3.1 Introduction

As noted in previous chapters, the mammalian cytochrome P450 monooxygenases (CYPs) are membrane proteins that serve a critical role in the metabolism of a wide array of structurally distinct endogenous and xenobiotic compounds, and the isoform CYP3A4 accounts for roughly half of all CYP-mediated drug metabolism (1). In addition to uncertainties about the effects of the membrane on ligand binding, the overall effects of the membrane on CYP3A4 stability remain undetermined. As such, the importance of understanding the role of CYP3A4 and other mammalian CYP isoforms in drug metabolism has become a subject of great importance during the drug design process. In fact, although it is now known that ~26% of the protein-coding genes in the human genome code for membrane proteins (70), it remains difficult to measure protein stability in actual lipid bilayers. This chapter describes the application of methods to study CYP3A4 stability in lipid nanodiscs, and possibly provides a template for studying other membrane proteins.

The resolution of several mammalian CYP crystal structures has improved our understanding of CYP structure and function. It is now suggested that the interactions between mammalian CYPs and the membrane are likely to be an important determinant in CYP conformation and function. As noted in chapter 2, epitope mapping and molecular dynamics simulations suggest a general orientation of mammalian CYPs where the F'- and G'- helices are associated with the membrane, as illustrated in Figure 1 (26,27,51). Those simulations also suggested that the membrane may promote the opening of several CYP active site access channels. A separate study by Denisov and coworkers demonstrated that, *in silico*, the F'-G' loop

can undergo significant motions when CYP3A4 is incorporated into a membrane (71). However, due to the difficulties in obtaining crystal structures of mammalian CYPs in a membrane environment, the simulations in these studies were performed using crystal structures of enzyme in bulk aqueous solvent, and as such may not necessarily represent the true conformations of the CYP *in vivo*. Furthermore, although molecular dynamics simulations are a powerful *in silico* technique, they may not necessarily be able to predict the full extent of dynamic motion a protein may undergo *in vivo*. Because of these inherent limitations, experimental methods are necessary to characterize CYP-membrane interactions.

Studying the thermal unfolding of proteins can provide information about the interactions which contribute to maintaining folded state. For example, Maves and coworkers used combinatorial mutagenesis of CYP119 (from *Sulfolobus solfataricus*) in conjunction with thermal unfolding in order to determine the relative contribution of different residues to the overall stability of the enzyme (72). In another example, rhomboid intramembrane proteases were tested for reversibility of unfolding, providing information pertaining to the mechanism of unfolding (73). Extending thermal unfolding studies to mammalian CYPs in a membrane can thus provide important information about the contributions of the membrane to CYP structure and function.

Differential scanning calorimetry (DSC) is a powerful method for measuring the thermal unfolding and stability of a protein, and can be applied to lipid-protein systems to investigate how the membrane affects the protein and vice versa (32,74,75). The earliest example of DSC being used to characterize the stability of mammalian CYPs was a study performed by Anzenbacher and colleagues in 1982 (34). In this study, they found that the general range of the CYP melting transition spanned from roughly 50-60 °C. However, this study was performed

using CYP isolated from rat whole liver microsomes rather than a single isoform and therefore made it is impossible to distinguish between individual CYPs. In another example, DSC was used to study CYP119, with the overarching goal of harnessing this isoform as a potential bioreactor in an industrial setting (76). While a single isoform was used to perform this study, however, CYP119 is a thermophilic enzyme with a melting temperature of ~90 °C, making it difficult to draw meaningful comparisons between this isoform and human CYP isoforms.

The thermal unfolding of CYP3A4 in a membrane environment has not been well characterized. In order to improve our understanding of the thermal unfolding of mammalian CYPs, CYP3A4 was incorporated into phospholipid bilayer nanodiscs. Nanodiscs are small, discoidal lipid bilayers surrounded by two 'belt-like' membrane scaffold proteins (40). They have been used to study of several membrane proteins, including several mammalian CYP isoforms (77-80). Nanodiscs have an added advantage over other model membrane systems in that they are able to monomerize membrane proteins due to their constrained size (nanodiscs formed using the membrane scaffold protein MSP1D1 are ~10 nm in diameter). This eliminates ambiguities which may arise from protein-protein interactions from an aggregated species.

Herein, we investigated the thermal unfolding of CYP3A4 incorporated into phospholipid bilayer nanodiscs using a combination of circular dichroism (CD) spectroscopy and DSC. Our results suggest a stabilizing effect of the membrane on CYP3A4. Furthermore, we present evidence that incorporation of the enzyme into a nanodisc membrane results in complexity in the unfolding process which was previously unseen. This study represents the first characterization of the thermal unfolding of a mammalian CYP in a nanodisc using DSC and provides a basic groundwork for future thermal unfolding studies of nanodisc-incorporated CYPs.

3.2 Materials and Methods

3.2.1 Protein Expression and Nanodisc Self-Assembly.

CYP3A4 and MSP1D1 expression and purification, and CYP3A4-nanodisc assembly were carried out as described in Chapter 2.

3.2.2 Size Exclusion Chromatography.

Size exclusion chromatography was performed on a Superdex™ 200 10/300 GL column (GE Healthcare) equilibrated with disc forming buffer (DFB; 100 mM potassium phosphate, 50 mM sodium chloride, pH 7.4). POPC nanodiscs, CYP3A4, CYP3A4-nanodiscs, and a 1:1 mixture of CYP3A4 and POPC nanodiscs (incubated together for 1 hour at room temperature), were prepared to 10 μM in disc formation buffer. 80 μL of each sample was injected on to the size exclusion column, and absorbance was monitored at 280 nm and 420 nm over the course of 60 minutes using a flow rate of 0.5 mL/min.

3.2.3 Variable Temperature Circular Dichroism (VT-CD).

Circular Dichroism (CD) Spectroscopy was performed using a Jasco 720 Circular Dichroism Spectrophotometer (Jasco, Inc., Easton, Maryland). The instrument was allowed to pre-equilibrate at 25 C for 10 minutes prior to insertion of the sample cuvette. In order to prevent the dynode from exceeding 700 volts, CYP3A4 and CYP3A4-nanodiscs were diluted to a total CYP3A4 concentration of 1 μM with CD buffer (25 mM potassium phosphate, 50 mM sodium fluoride, pH 7.4) prior to analysis. Phosphate and chloride absorb in the far-UV region of interest, and as such it was necessary to lower the phosphate concentration as well as substitute sodium chloride in our buffer with sodium fluoride. Sample was loaded into a 0.1 cm pathlength quartz cuvette and allowed to equilibrate inside the CD spectrophotometer for 5 minutes at 25 °C prior to data collection. The instrument was set to record data from 25 to 85 °C with increments

of 10 °C. 8 replicate scans were collected from 195 to 270 nm in continuous scanning mode for each temperature, with a scan speed of 100 nm/min and a 2 nm bandwidth. The temperature slope was set to 1 °C per minute, and samples were allowed to equilibrate for an additional 5 minutes after the instrument reached a new temperature increment prior to data collection.

Data were smoothed, buffer-subtracted, corrected for CYP3A4 concentration, and corrected for the 511 residues in our CYP3A4 construct. For CYP3A4-nanodiscs, in order to correct for the contribution of the MSP1D1 from the nanodisc, CD spectra were collected using empty nanodiscs in the same manner as above. Assuming that CYP3A4 does not significantly alter MSP1D1 secondary structure, the nanodisc raw spectra was then scaled for concentration and subtracted from the raw spectra of the CYP3A4 nanodisc. The CYP3A4 nanodisc spectra was then corrected for CYP3A4 concentration and corrected for the number of CYP3A4 residues.

Assuming that CYP3A4 unfolding was essentially complete at 85 °C, melting temperatures were estimated from plots of fraction unfolded at 222 nm vs. temperature by fitting to the logistic function:

$$f(T) = \frac{1}{1 + e^{-k*(T-T_m)}} \qquad \text{Eq. 1}$$

Where T is the sample temperature, T_m is the melting temperature, and k is a general measure of the cooperativity of unfolding, with larger values indicating a higher cooperativity.

Secondary structural content was estimated for far-UV CD spectra collected at 25 °C using CONTINLL, CDSSTR, and SELCON3 from the CDPro software package and averaging the results from the three programs (81,82).

3.2.4 Ketoconazole Binding Titrations.

Binding titrations were carried out at 25 °C with a scan range of 350-700 nm using an Aminco DW2a spectrophotometer (Olis, Inc., GA). Ketoconazole (KTZ) was purchased from Sigma-Aldrich (St. Louis, MO), and 75 μM and 125 μM stocks were prepared in 50% methanol. A sample cuvette was filled with CYP3A4 or CYP3A4-nanodiscs diluted to 1.4 μM with DFB. A reference cuvette was filled with DFB for CYP3A4, or an equivalent concentration of empty nanodiscs in DFB for CYP3A4-nanodiscs in order to minimize any contributions from binding of ligand to the nanodisc membrane. The cuvettes were allowed to equilibrate to temperature for 10 minutes. Prior to the addition of KTZ, a ligand-free absolute absorbance spectrum was recorded. Binding of KTZ to the enzyme was then monitored by titrating equal volumes of ligand into each cuvette and recording absolute spectra after each addition of ligand. The final concentration of methanol in both cuvettes did not exceed 2%. Data were baseline-adjusted such that there is zero absorbance at 700 nm. The data was then corrected for the change in total volume, and difference spectra were calculated by subtracting the ligand-free spectrum for CYP3A4 or CYP3A4-NDs from the spectra collected from each subsequent addition of ligand. Binding isotherms were generated by plotting the difference between the absorbance maximum and minimum of the spectra as a function of ligand concentration, and data were fit to the quadratic binding equation using IgorPro (Wavemetrics, Inc., OR), allowing all parameters to float, in order to estimate the dissociation constant, K_D, as described in chapter 2.

3.2.5 Differential Scanning Calorimetry.

Differential Scanning Calorimetry (DSC) experiments were performed using a MicroCal Capillary DSC System (MicroCal, Northampton, MA). CYP3A4, CYP3A4-nanodiscs, or empty nanodisc samples were dialyzed overnight against DFB and diluted to a final concentration of 5 μM. KTZ-bound CYP3A4 and CYP3A4-nanodisc samples were prepared in the same manner as

above, and KTZ (dissolved in 100% methanol) was added to a final concentration of 50 μM immediately prior to performing DSC scans (the final methanol co-solvent concentration did not exceed 1%). A thermal history for the instrument was established by performing three consecutive scans with DFB alone prior to the analysis of a single sample. In the case of KTZ-containing samples, the presence of the methanol co-solvent increases the heat capacity of the buffer, therefore a thermal history was established using DFB supplemented with 50 μM KTZ. CYP3A4 endotherms were measured by scanning samples from 10 to 130 °C at a scan rate of 60 °C/h. Thermograms were baseline corrected, and transition temperatures (T_m) and total calorimetric enthalpies of unfolding (ΔH_{cal}) of endotherms were determined using the software package Origin (MicroCal). Due to the nature of the analysis by the Origin software, T_m and total ΔH_{cal} are determined based on the maximum of the endotherm as well as the integrated area of the endotherm, and as such, does not report error values. Additionally, CYP3A4 endotherms were deconvoluted using the Origin analysis software in order to determine melting temperatures (T_m), calorimetric enthalpies (ΔH_{cal}), and van't Hoff enthalpies (ΔH_{vH}) of potential unfolding events within the endotherm. In contrast to ΔH_{cal}, which is calculated by integrating the DSC endotherm and as such represents the total change in enthalpy for all melting processes within the endotherm, ΔH_{vH} assumes a two-state process, and thus only a single melting process, according to the van't Hoff equation:

$$\Delta H_{vH} = ln\,(\alpha/K) * RT \qquad \text{Eq. 2}$$

where K is the equilibrium constant for unfolding, R is the ideal gas constant, T is temperature, and α is a constant(83). Directly comparing ΔH_{cal} and ΔH_{vH} thus allows for verification of a two-state model of protein unfolding.

3.3 Results

3.3.1 Size-Exclusion Chromatography.

Size-exclusion chromatography was utilized in order to characterize the aggregation status of CYP3A4 and nanodisc samples. At 280 nm, empty nanodiscs (150 kDa) have a characteristic peak retention time of 25 minutes (Fig. 2a) (42). By contrast, CYP3A4 (57 kDa) shows a peak retention time of 21 minutes (Fig. 2a). That the CYP3A4 retention time is much earlier than the empty nanodisc retention time indicates that the enzyme is oligomeric in aqueous solution. CYP3A4-nanodiscs (207 kDa) show a peak retention time of 23 minutes (Fig. 3), consistent with what has been reported previously by others and demonstrating the elimination of the apparent oligomeric state of CYP3A4 in aqueous buffer (42).

CYPs display a heme Soret absorbance signature at 420 nm, making it possible to specifically monitor the elution of CYP3A4 from the size-exclusion column while eliminating absorbance contributions from other non-heme-containing signatures, such as the membrane scaffold protein of the nanodisc or free lipid. The elution profile of CYP3A4 mixed with pre-formed empty nanodiscs is represented by the green trace in Figure 1a. It can be seen that when monitoring total protein content at 280 nm, two distinct species are observed, corresponding to CYP3A4 in aqueous solution (21 minutes) and empty nanodiscs (25 minutes). When the same sample is monitored at 420 nm, only a peak with a 21 minute retention time corresponding to CYP3A4 is observed, and there is no apparent shift to a later retention time (Fig. 1b). CYP3A4-nanodiscs, however, show a peak retention time at 23 minutes when monitored at either 280 nm or 420 nm (Fig. 3). Taken together, these data confirm that CYP3A4 does not spontaneously insert into, or dissociate from, the membrane of preformed nanodiscs.

3.3.2 Variable Temperature Circular Dichroism.

Because the thermal unfolding of mammalian CYPs has remained largely uncharacterized, CD spectroscopy was used to monitor the unfolding of CYP3A4 in aqueous solution and in a nanodisc membrane. As expected, at room temperature both CYP3A4 in buffer and CYP3A4-nanodiscs yield a double minima characteristic of a protein that is largely α-helical in structure (Figure 4 a & b). The secondary structure analysis results for CYP3A4, CYP3A4 in nanodiscs (corrected for the contribution from MSP1D1), and empty nanodiscs are presented in Table 1. While the α-helicity of CYP3A4-nanodiscs remained unchanged relative to CYP3A4 in buffer, the β-sheet content showed a slight but significant increase from 3.5% for CYP3A4 in DFB to 5.3% for CYP3A4 in nanodiscs. Available crystal structures of CYP3A4 indicate a secondary structure content of approximately 50% α-helix and 8% β-sheet (8,84-87). This is in relatively good agreement with our experimental results, and the discrepancies in secondary structure content may likely be explained due to the fact that the available crystal structures were obtained in the absence of the helical N-terminal membrane anchor, whereas as our CYP3A4 construct maintains much of this anchor. Also shown are CD spectra for empty POPC nanodiscs (Figure 4b, inset). The mean residue ellipticity of empty nanodiscs changes minimally over the temperature range analyzed, therefore the contribution of the unfolding of the nanodisc complex to the unfolding of CYP3A4 is minimal.

Table 1. Estimates of CYP3A4 secondary structure content at 25 °C

Component	CYP3A4	CYP3A4-Nanodisc	Empty Nanodisc
% α-helix	63.7 ± 1.5	64.0 ± 1.8	43.5 ± 1.7
% β-sheet	3.5 ± 1.0	5.3 ± 0.5	13.5 ± 1.3
% Random Coil	33.0 ± 2.3	30.9 ± 1.9	43.4 ± 2.5

For CYP3A4 and CYP3A4 in nanodiscs, as the temperature increases, the mean residue ellipticity at 222 nm increases, or becomes less negative, as expected, corresponding to an apparent loss in α-helix content. Plots of fraction unfolded vs. temperature indicate that unfolding of CYP3A4 in buffer is a highly cooperative process (Figure 4c). In contrast, the unfolding of CYP3A4 in POPC nanodiscs is much less cooperative. An estimate of Tm for CYP3A4 in POPC nanodiscs based on my CD spectra is 56.8 ± 1.1 °C, vs. 49.8 ± 0.5 °C for the CYP3A4 in buffer, indicating that incorporation of CYP3A4 into the nanodisc membrane results in a significant increase in CYP3A4 stability. While, to the best of my knowledge, there are no reported literature values for the melting temperature of CYP3A4 either in aqueous buffer or in a membrane, these values do fall within the ~40 – 60 °C range predicted for the melting of mammalian CYPs, as suggested by Anzenbacher and colleagues (34).

3.3.3 Spectral Binding Titrations.

KTZ binding titrations were performed in order to determine how incorporation of CYP3A4 into a nanodisc membrane affects the ligand binding affinity. KTZ is a tight-binding CYP3A4 inhibitor that induces a type-II (low spin) shift in the heme Soret peak (88). Titrating ketoconazole into CYP3A4 results in the expected low spin shift, with an absorbance maximum at 434 nm and a minimum at 409 nm (Fig. 5, inset). A plot of the difference of the absorbance maxima and minima as a function of ligand concentration results in the binding isotherm shown in Figure 5. Fitting of the data to a quadratic equation (described in Chapter 2) results in a K_D of 0.080 ± 0.010 μM, in good agreement with what has been previously reported for KTZ binding to CYP3A4 (88).

Binding of KTZ to CYP3A4-nanodiscs was also monitored, and empty nanodiscs were included in the reference cuvette in order to correct for the effect of KTZ binding to the nanodisc

membrane. KTZ again induced a type-II shift in the heme Soret peak with minima and maxima again at 434 and 409 nm, respectively (Fig. 6, inset). A binding isotherm was generated from the absorbance difference between the maxima and minima, and fitting to a quadratic equation yields a K_D of 0.127 ± 0.010 μM (Fig. 6). Thus, incorporation of CYP3A4 into nanodiscs appears to induce a conformational change which lowers the apparent affinity of KTZ for the enzyme active site.

3.3.4 Differential Scanning Calorimetry.

DSC was used to monitor the unfolding of CYP3A4, CYP3A4-nanodiscs, and empty nanodiscs. DSC monitors the thermal unfolding properties of a protein sample. However, it differs from VT-CD in that DSC directly monitors changes in the heat capacity (C_p) of a system as a function of sample temperature, which can then be used to determine the calorimetric enthalpy of unfolding (ΔH_{cal}). The ΔH_{cal} provides an indirect measure of the combined van der Waals interactions, hydrogen bonding, and electrostatic interactions contained in the sample. The heat capacity is related to calorimetric enthalpy of unfolding (ΔH_{cal}) by the equation:

$$\Delta H_{cal} = \int C_p dT \qquad \text{(Eq. 3)}$$

where T is temperature. Thus, by integrating the DSC thermogram, we can determine ΔH_{cal} for each transition.

Figure 7 shows the resulting thermograms from DSC experiments performed with empty nanodiscs, CYP3A4 in DFB, and CYP3A4 incorporated into nanodiscs. Unfortunately, due to limitations in sample quantity, reversibility of CYP3A4 unfolding is currently not known. As such, the thermodynamic interpretations of the data should currently be viewed with a degree of caution. The transition temperatures and total ΔH_{cal} for each sample are summarized in Table 2.

The observed transition temperature for CYP3A4 in DFB was 51.9 °C, in good agreement with the T_m from VT-CD experiments. Incorporation of CYP3A4 into a nanodisc membrane results in an increase in the T_m to 54.8 °C, also consistent with the stability increase observed with VT-CD. The ΔH_{cal} for the CYP3A4 endotherm increased relative to that observed for CYP3A4 in DFB, indicating an increase in the relative abundance of stabilizing forces upon incorporation of CYP3A4 into the nanodisc membrane (Table 2).

Table 2. Melting temperatures and changes in the calorimetric enthalpy of unfolding.

	T_m (°C)		ΔH_{cal} (cal/mol)[a]	
Sample	CYP3A4	Nanodiscs[b]	CYP3A4	Nanodiscs[b]
CYP3A4 in DFB	51.9	-	8.9×10^4	-
CYP3A4-Nanodiscs	54.8	85.8	1.5×10^5	5.5×10^5
CYP3A4 in DFB + KTZ[c]	54.4	-	9.0×10^4	-
CYP3A4-Nanodiscs + KTZ[c]	61.2	87.9	2.4×10^5	5.0×10^5
Empty Nanodiscs	-	76.8	-	7.9×10^4

[a]Calorimetric enthalpy
[b]Nanodisc complex transition
[c]50 μM ketoconazole

A late transition was also observed in the CYP3A4-nanodisc sample with a T_m of 85.8 °C. This late transition most likely represents the melting of the nanodisc membrane complex. In empty nanodiscs the only transition observed within the scan range has a T_m of 76.8 °C, which is ~9 °C lower than the late transition in CYP3A4-nanodiscs. Additionally, there is an increase in the ΔH_{cal} for the nanodisc transition upon incorporation of CYP3A4, relative to empty nanodiscs (Table 2). Thus, incorporation of CYP3A4 into nanodiscs appears to stabilize the nanodisc complex. This may be due to alterations in membrane fluidity which may result in the enhanced stability of the MSP, and thus, the nanodisc itself.

In order to probe the effects of a tight-binding ligand on CYP3A4 unfolding, DSC experiments were also performed in the presence of 50 μM KTZ, and the results are also presented in Table 2. The addition of KTZ caused an increase of ~2 °C in the T_m of CYP3A4 in DFB while not greatly affecting ΔH_{cal}. Interestingly, CYP3A4-nanodiscs exhibited a relatively large T_m increase of ~6 °C and a 1.6-fold increase in ΔH_{cal} upon the addition of KTZ. These differing responses to the addition of KTZ highlights the effect of the membrane on the thermodynamics properties of CYP3A4.

In order to investigate the complexity of CYP3A4 unfolding further, the CYP3A4 transition was deconvoluted for both the DFB and nanodisc-incorporated CYP3A4 samples using the DSC analysis software package Origin (Microcal). Figure 8 shows the deconvoluted spectra for CYP3A4 and CYP3A4-nanodiscs in the presence and absence of KTZ. Melting temperatures (T_m) calorimetric enthalpies (ΔH_{cal}), van't Hoff enthalpies (ΔH_{vH}), and the ΔH_{vH}/ ΔH_{cal} ratio for the deconvoluted transitions have been summarized in Table 3. ΔH_{vH} is a theoretical change in enthalpy of unfolding which assumes a two-state transition (75). Analyzing the $\Delta H_{vH}/\Delta H_{cal}$ ratio is commonly used as an indirect analysis of the nature of transitions observed by DSC. A ratio = 1 indicates a simple two-state transition. Ratios of $\Delta H_{vH}/\Delta H_{cal} > 1$ have been interpreted to indicate the formation of aggregate species; the unfolding of protein aggregates tends to be a cooperative process, resulting in a sharper transition in the DSC endotherm, and therefore a larger value for ΔH_{vH}. By contrast, ratios of $\Delta H_{vH}/\Delta H_{cal} < 1$ have been interpreted to indicate the existence of a species with multiple domains that undergo unfolding, resulting in a broader DSC endotherm and a smaller value for ΔH_{vH}.

Table 3. Recovered melting temperatures, calorimetric and van't Hoff enthalpies for deconvoluted thermograms.

System	T_m (°C)	ΔH_{cal} (cal/mol)[a]	ΔH_{vH} (cal/mol)[b]	$\Delta H_{vH}/\Delta H_{cal}$
CYP3A4 (DFB)	48.1	4.1×10^4	8.5×10^4	2.08
	52.6	5.0×10^4	1.2×10^5	2.47
CYP3A4-nanodiscs	49.2	7.8×10^4	8.4×10^4	1.08
	53.6	7.1×10^4	1.4×10^5	1.93
	56.7	3.5×10^4	2.1×10^5	5.94
CYP3A4 (DFB) + KTZ[c]	50.9	3.3×10^4	9.7×10^4	2.95
	54.4	5.8×10^4	1.6×10^5	2.82
CYP3A4-nanodiscs + KTZ[c]	51.6	6.6×10^4	7.9×10^4	1.19
	56.9	6.3×10^4	1.2×10^5	1.85
	60.5	6.5×10^4	2.0×10^5	3.08
	62.8	3.0×10^4	3.1×10^5	10.33

[a] calorimetric enthalpy
[b] van't Hoff enthalpy
[c] 50 μM ketoconazole

The endotherm for CYP3A4 in DFB was best fit to two transitions in both the presence and absence of KTZ, and analysis of the $\Delta H_{vH}/\Delta H_{cal}$ ratio gives a value > 1 for each, suggesting the formation of an aggregate species. This is consistent with what was observed by size-exclusion chromatography (Figure 2). Upon incorporation of CYP3A4 into nanodiscs, the endotherm is best predicted by three transitions: a low temperature transition that appears two-state in nature ($\Delta H_{vH}/\Delta H_{cal} = 1$), as well as an intermediate and a high temperature transition, both with $\Delta H_{vH}/\Delta H_{cal}$ ratios greater than 1. Although it is typically thought that a $\Delta H_{vH}/\Delta H_{cal}$ ratio greater than 1 indicates that the protein exists as an aggregate species prior to unfolding, based on size-exclusion chromatography results, this is unlikely to be the case for CYP3A4 in

nanodiscs. It cannot be ruled out that aggregate species may also be forming after unfolding of the enzyme at higher temperatures, which could potentially affect the apparent $\Delta H_{vH}/\Delta H_{cal}$ ratios observed here. An alternative explanation may be the formation of an "aggregate-like" species formed within the CYP3A4-nanodisc complex (see discussion).

Addition of KTZ to CYP3A4-nanodiscs adds further complexity to the unfolding of CYP3A4. The corresponding DSC thermogram is best fit to four transitions, and on the basis of the $\Delta H_{vH}/\Delta H_{cal,}$ the lowest melting temperature in the deconvolution appears to be a multimeric species. It should be noted for deconvolution of all CYP3A4 endotherms that currently it is not possible to assign these apparent transitions to any specific unfolding regions of the enzyme as there are no previous experimental benchmarks with which to rely upon. Nevertheless, deconvolution of the CYP3A4 endotherm reveals the complexity that is introduced to CYP3A4 unfolding upon incorporation into a membrane. Furthermore, the addition of KTZ resulted contrasting effects on the unfolding of CYP3A4 in DFB and in nanodiscs; the overall unfolding of CYP3A4 in DFB exhibited an increase in apparent cooperativity upon KTZ binding, while the overall unfolding of CYP3A4 in nanodiscs decreased in apparent cooperativity and becomes a more complex process upon KTZ binding.

3.4 Discussion

Despite the dominant role of mammalian CYPs in drug metabolism, little is known about the thermal unfolding characteristics of CYP isoforms in a membrane environment. Therefore, we utilized CD spectroscopy and DSC to investigate how a model membrane (phospholipid bilayer nanodiscs) influences the thermal unfolding properties of CYP3A4. To the best of my knowledge, this study represents the first in-depth investigation into the thermal unfolding properties of an individual mammalian CYP isoform using DSC, as well as the first investigation

of the unfolding of a membrane protein in a nanodisc membrane analyzed by DSC. These experiments serve as the basic framework for future studies of CYP3A4 in nanodiscs of controlled lipid composition, as well as other mammalian CYP isoforms.

Based on size-exclusion chromatography, in aqueous solution, CYP3A4 exists as an aggregate species. However, because there has been no previous characterization of CYP3A4 thermal unfolding, our initial goal was to observe the behavior of a monomeric CYP in a membrane environment while eliminating potential protein-protein interactions. Therefore, in order to investigate the effects of a membrane on monomeric CYP, it was necessary to utilize phospholipid bilayer nanodiscs as our model membrane system as they allow for the monomerization of membrane proteins in a more native-like lipid environment (42). Unfortunately, the use of detergents to solubilize CYP3A4 in aqueous solution was not a viable option because the detergents commonly used to solubilize mammalian CYPs have also been shown to bind to the active site, which can potentially alter the conformation and affect the thermal unfolding properties of these enzymes (68,89,90). Therefore, the thermal unfolding of oligomeric CYP3A4 in solution was investigated for a general comparison to monomeric CYP3A4 in nanodiscs.

CD experiments at varying temperature revealed that CYP3A4 unfolding in DFB has a high degree of apparent cooperativity, as revealed by a sharp transition from the folded to the unfolded state (Figure 4a). This high degree of apparent cooperativity may be explained due to the protein existing in an aggregate state in aqueous buffer in the absence of a membrane or detergent, which typically results in the appearance of a sharper unfolding transition. Upon the initial unfolding of one or a small number of units in the CYP3A4 aggregate, stabilizing interactions are lost, resulting in subsequent rapid unfolding of the rest of the aggregate species.

By contrast, CYP3A4 incorporated into nanodiscs exhibited a much lower degree of apparent cooperativity. Typically, it would be expected that the monomeric CYP would have a lower T_m than the aggregate species due to the absence of other stabilizing CYP molecules. However, an increase in the T_m of CYP3A4 in nanodiscs was observed, despite its much lower degree of cooperative unfolding. This would indicate that although CYP3A4 is monomeric in the nanodisc, the nanodisc membrane serves to stabilize the CYP to a greater degree than the aggregate species.

Incorporation of CYP3A4 into nanodiscs results in an increase in the T_m for the CYP3A4 transition. This is not surprising as CYP3A4 is a membrane protein and has likely been adapted to function optimally in the membrane. It is interesting to note that the addition of KTZ produced a much more pronounced effect on the thermal denaturation of CYP3A4-nanodiscs compared to CYP3A4 in DFB. A slight increase (~2 °C) in the T_m of CYP3A4 in DFB was observed upon the addition of KTZ, however the ΔH_{cal} remained relatively unchanged. By contrast, CYP3A4-nanodiscs exhibited a large increase (~6 °C) in T_m accompanied by an increase in ΔH_{cal}. There is precedent in the literature for a wide variety of ligands inducing conformational changes in several CYP isoforms, including, but not limited to, human CYP3A4, CYP119 of *Sulfolobus acidocaldarius*, and P450cam of *Pseudomonas putida* (56,91,92). Previously our group has demonstrated by hydrogen-deuterium exchange mass spectrometry that upon binding of KTZ to CYP3A4 in nanodiscs, portions of the G helix and H helix become less solvent accessible (93). It is likely that the addition of saturating KTZ induces a conformational change in CYP3A4 which promotes deeper insertion of the G helix in the nanodisc membrane, resulting in my experimentally observed increases in T_m and ΔH_{cal}. In the absence of a membrane, CYP3A4 may

be undergoing a similar conformational change upon KTZ binding, however it is unable to form new stabilizing interactions that would result in a large increase in the T_m and ΔH_{cal} of unfolding.

The complexity of CYP3A4 unfolding is revealed by the spectral deconvolution of the DSC data. As evidenced by the appearance of a third transition, CYP3A4 unfolding becomes more complex in a nanodisc membrane. Although we currently lack the ability to assign these deconvoluted transitions to any specific regions of the CYP, the $\Delta H_{vH}/\Delta H_{cal}$ ratio can be used to gain some insight as to their nature, assuming that these values are indeed accurate. In the case of CYP3A4 prepared in DFB, the $\Delta H_{vH}/\Delta H_{cal}$ ratio greater than 1 for both transitions suggests aggregation of the enzyme prior to unfolding, which would not be unexpected in aqueous solution based on size-exclusion chromatography. Interestingly, in the case of CYP3A4-nanodiscs, while a low transition with $\Delta H_{vH}/\Delta H_{cal}$ approximately equal to 1 was observed, suggesting a two-state transition, the two higher temperature transitions in the CYP3A4 endotherm each had a $\Delta H_{vH}/\Delta H_{cal}$ ratio greater than 1. Although there is no well-documented theoretical framework for membrane proteins, according to dogma for soluble proteins in the absence of a membrane, a ratio greater than 1 suggests the presence of an aggregate species prior to unfolding (74). However, this is unlikely for CYP3A4 in nanodiscs because size-exclusion chromatography indicates that this complex is monomeric and does not form aggregates in aqueous buffer at the concentrations used here. Additionally, because an aqueous solvent is being used, CYP3A4 is unlikely to form aggregates on its exposed hydrophilic surface prior to unfolding. An alternative explanation for a $\Delta H_{vH}/\Delta H_{cal}$ ratio greater than 1 may be that the presence of the hydrophobic membrane may promote unfolding of the enzyme by stabilizing the unfolded state at higher temperatures (Scheme 1). This would increase the apparent cooperativity of thermal unfolding and result in a larger ΔH_{vH} than expected, giving the appearance of an

aggregate state when analyzed by DSC. In the future, DSC experiments should be performed at varying CYP3A4-nanodisc concentrations in order to test this; a lack of a concentration-dependent shift in the T_m of CYP3A4 in nanodiscs would indicate that individual molecules of CYP3A4-nanodiscs are not forming aggregates after unfolding, further supporting this idea. Furthermore, SEC should be performed on CYP3A4-nanodisc samples after they have been allowed to incubate above the CYP3A4 melting temperature (but below the nanodisc complex melting temperature) in order to determine whether protein aggregation is occurring after unfolding. Again, it should be noted that currently it is unclear whether the deconvoluted melting transitions correspond to any specific regions of the CYP3A4 structure, and as such, this interpretation is purely speculative.

The addition of KTZ did not change the number of components when deconvoluting the CYP3A4 transition in DFB, and the ΔH_{vH} and ΔH_{cal} values were not greatly altered. However, the unfolding of CYP3A4-nanodiscs became more complex upon the addition of KTZ. As noted above, the deconvoluted unfolding transitions cannot be assigned to any specific regions of CYP3A4 due to a lack in the literature of the thermal unfolding properties of this enzyme. Nevertheless, it is evident from these data that in addition to increasing the stability of the enzyme, KTZ adds further complexity to the unfolding of CYP3A4 in a nanodisc, suggesting distinct conformational differences upon binding of this ligand.

3.5 Conclusion

This chapter provides the first characterization of the thermal unfolding properties of CYP3A4 in a nanodisc utilizing DSC and circular dichroism. The data are consistent with the monomerization of CYP3A4 in nanodiscs and suggest that incorporation into a membrane adds further complexity to the unfolding process. As such, a mechanism is proposed whereby the

globular domain of CYP3A4 must partially release interactions with the membrane without fully dissociating from the nanodisc, prior to an unfolding event (Scheme 1). After unfolding has taken place, the denatured enzyme is then stabilized by the hydrophobic nanodisc membrane. Addition of KTZ may induce a conformational change that results in the formation of new contacts between the enzyme and the membrane, contributing to the observed increase in thermal stability and ΔH_{cal}. Alterations in membrane composition may potentially affect the stability of the enzyme and shall be investigated further in chapter 4.

3.6 Figures

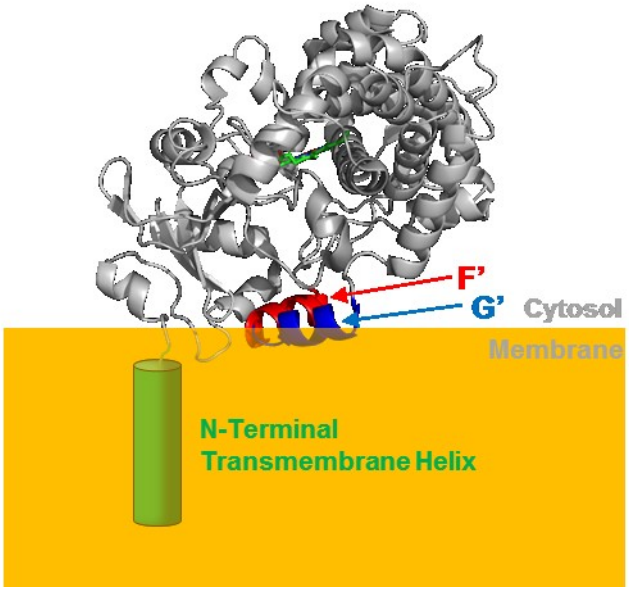

Figure 1. Putative orientation of CYP3A4 in the lipid bilayer. This representation is consistent with many MD simulations and H/DX mass spectrometry. The N-terminal helix (green) is expected to insert deeply into the membrane, whereas the F'- (red) and G'-helices (blue) insert less deeply.

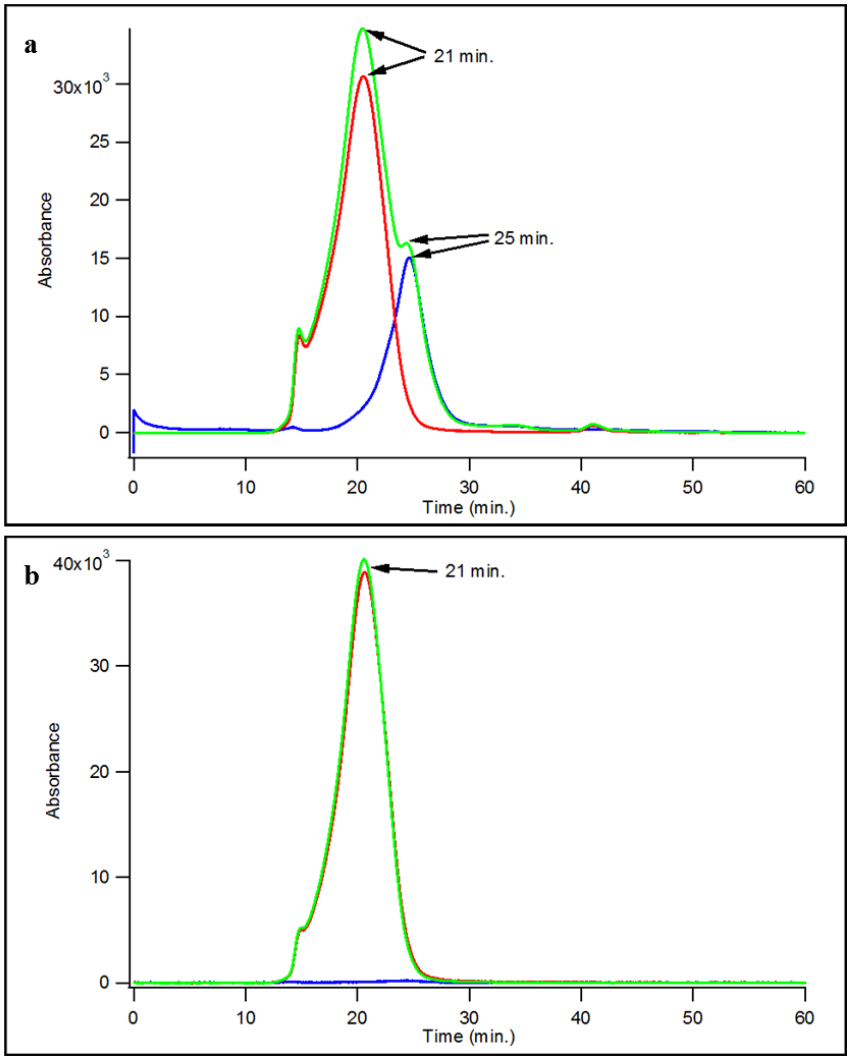

Figure 2. Size-exclusion chromatograms for CYP3A4 (red), empty nanodiscs (blue), and a mixture of CYP3A4 and pre-formed empty nanodiscs (green). Samples were monitored at 280 nm (A) and 420 nm (B). CYP3A4 has a characteristic peak retention time of 21 minutes, whereas empty nanodiscs have a characteristic peak retention time of 25 minutes. Mixing of CYP3A4 with empty nanodiscs does not result in spontaneous insertion of the enzyme into the membrane.

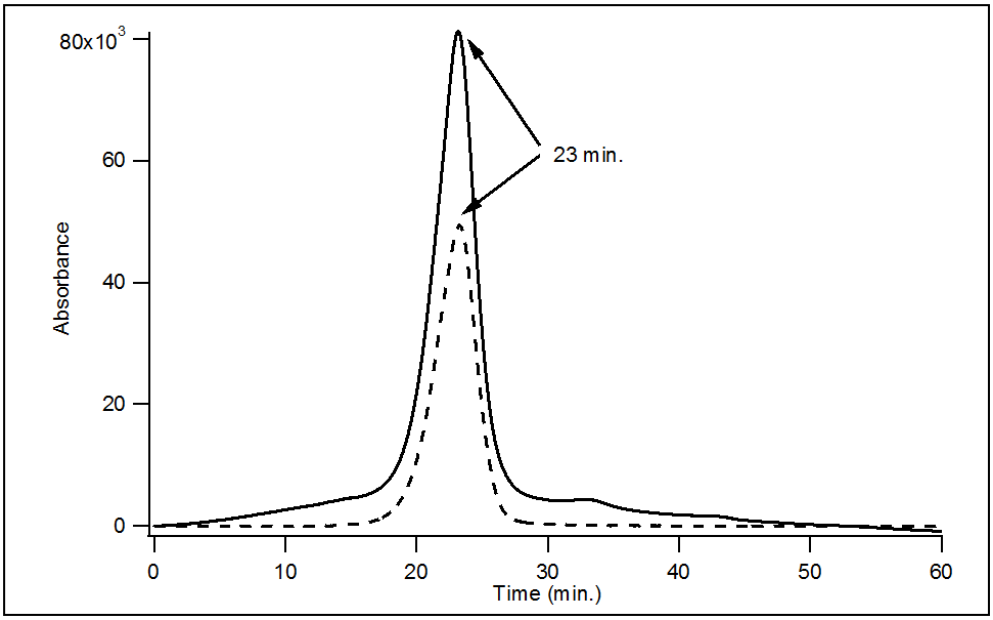

Figure 3. Size exclusion chromatogram of purified CYP3A4-nanodiscs, monitored at 280 nm (solid line) and 420 nm (dashed line). CYP3A4-nanodiscs have a characteristic single peak retention time of 23 minutes.

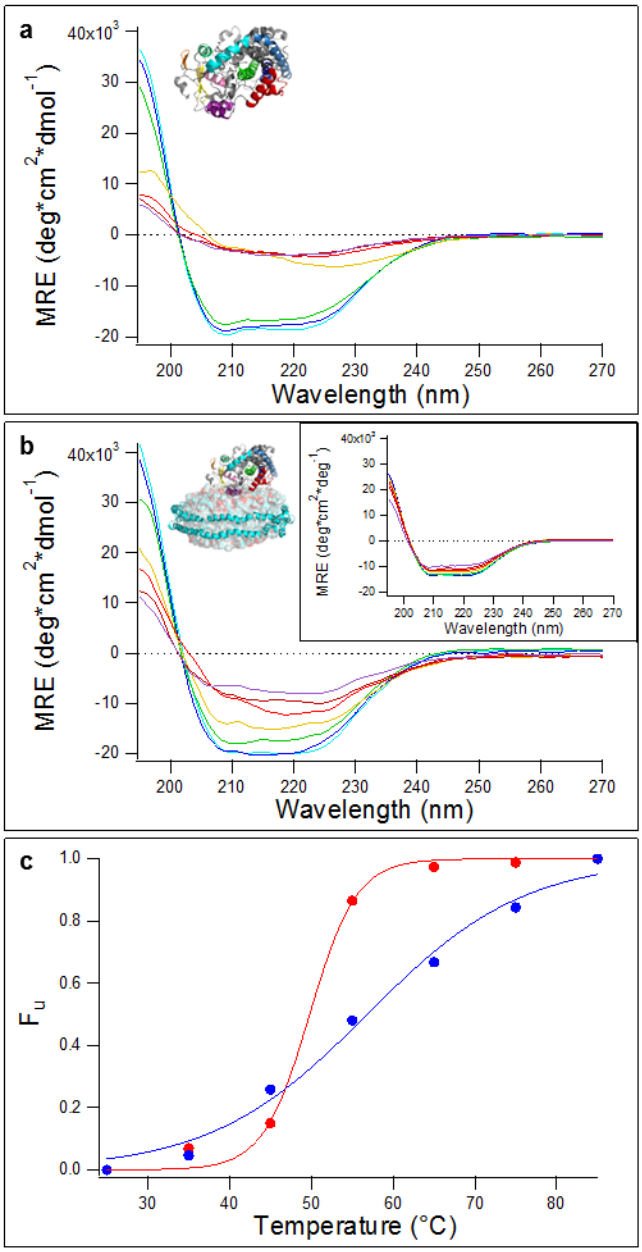

Figure 4. Circular dichroism spectroscopy for samples collected at varying temperatures. CD spectra were recorded at temperatures between 25 C and 80 C for (a) CYP3A4 in DFB and (b) CYP3A4 incorporated into 100% POPC nanodiscs (inset: CD spectra for empty POPC nanodiscs). (c) The fractional change in ellipticity is shown with increasing temperature. red = CYP3A4 in buffer, blue = CYP3A4 in 100% POPC nanodiscs. Solid lines are fits to a logistic function to estimate T_m.

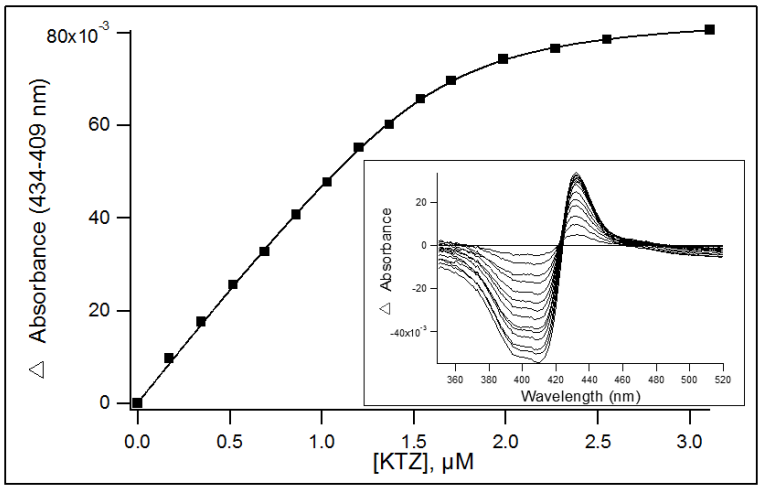

Figure 5. Ketoconazole binding titrations to CYP3A4 in DFB. The absorbance difference between 434 nm and 409 nm was plotted as a function of KTZ concentration. Data were fit to the quadratic binding equation for tight binding ligands to yield a K_D = 0.081 ± 0.010 µM. (Inset: calculated difference absorbance spectra collected for each addition of KTZ).

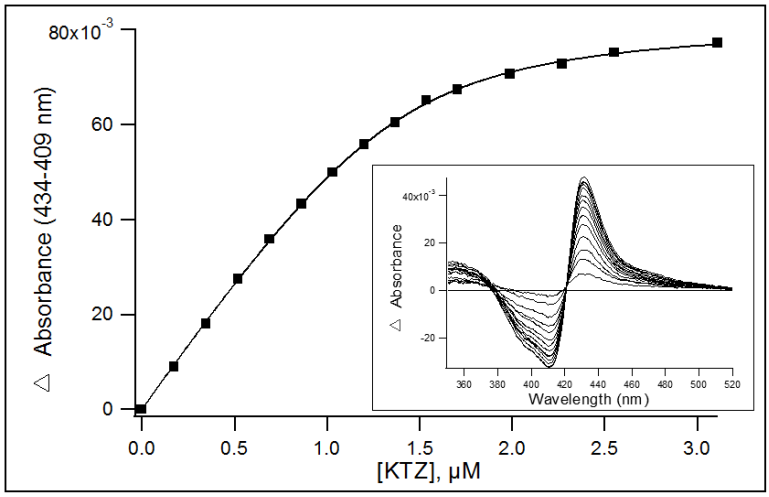

Figure 6. Ketoconazole binding titrations to CYP3A4-nanodiscs. The absorbance difference between 434 nm and 409 nm was plotted as a function of KTZ concentration. Data were fit to the quadratic binding equation for tight binding ligands to yield a K_D = 0.127 ± 0.010 µM. (Inset: calculated difference absorbance spectra collected for each addition of KTZ).

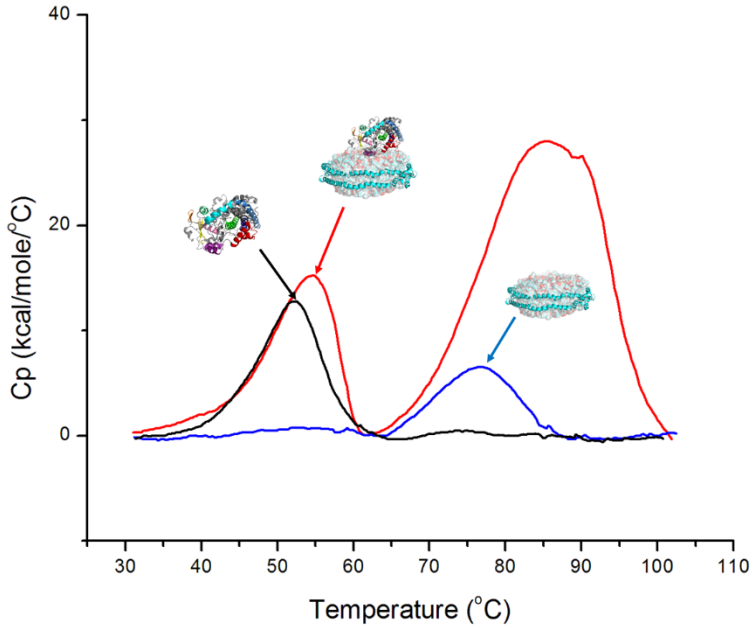

Figure 7. DSC thermograms recorded for empty nanodiscs (blue), CYP3A4 in DFB (black), and CYP3A4-nanodiscs (red). CYP3A4 thermal denaturation occurs at a lower temperature than melting of the nanodisc complex.

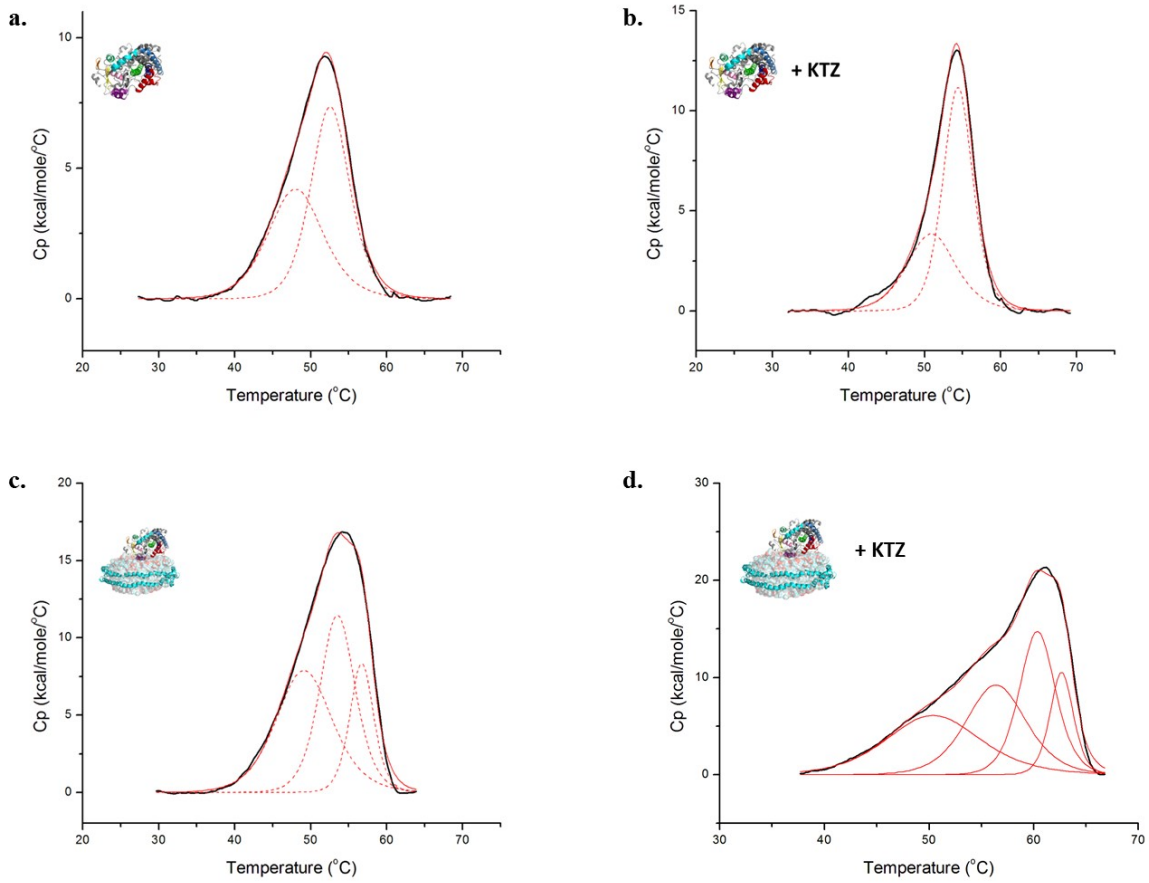

Figure 8. Deconvolution of the DSC thermogram attained for the CYP3A4 transition under varying conditions. (a) CYP3A4; (b) CYP3A4 + 50 μM ketoconazole; (c) CYP3A4-nanodiscs; (d) CYP3A4-nanodiscs + 50 μM ketoconazole. All samples were analyzed at a concentration of 5 μM.

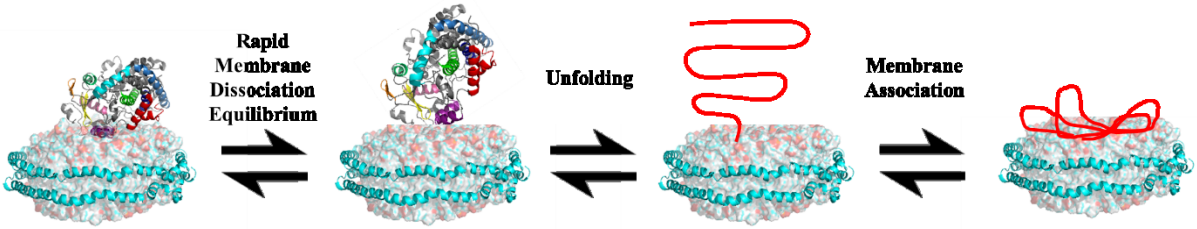

Scheme 1. Possible mechanism of unfolding for CYP3A4 incorporated into a nanodisc membrane. CYP3A4 may exists in very rapid equilibrium between a fully associated and partially dissociated state with the nanodisc membrane. In the partially dissociated state, unfolding can take place as the temperature is increased, and the unfolded protein can then be stabilized by associating with the nanodisc membrane, increasing the apparent cooperativity of unfolding.

Chapter 4

Effects of Lipid Composition on Cytochrome P450 3A4 Function and Stability

4.1 Introduction

Mammalian CYPs are membrane proteins, and are primarily located in the endoplasmic reticulum (E.R.) and mitochondrial membranes (94). CYP structure and function has been an area of intense research focus, especially as it pertains to drug development. Membranes *in vivo* are a mixture of different lipid types as well as membrane components (35,95). However, many *in vitro* studies of mammalian CYPs are performed using a single type of lipid, and there is relatively few data which systematically investigate the effects of lipid composition on CYP structure and function.

The composition of biological membranes can have a profound effect on several different types of membrane proteins *in vivo* and *in* vitro (96). There is evidence that biological membrane composition can influence the opening and closing of voltage-gated ion channels (97), the functional stability of G-protein coupled receptors (98), and even contribute to signal transduction by modulating the location of signal transduction proteins (99). Several studies have investigated the effect of lipid composition on mammalian CYP functionality. Ingelman-Sundberg and coworkers demonstrated that CYP3A4 activity is enhanced by the presence of anionic lipids in the membrane (36), and Kim and coworkers observed that CYP3A4 more readily bound to membranes containing relatively high levels of anionic phospholipid (100).

Lipid composition effects have also been investigated for other mammalian CYP isoforms. For instance, it was observed that alterations in lipid composition significantly affected the conformation of CYP1A2, as well as its efficiency of insertion into a membrane (37,101). A

similar effect of lipid composition had been observed for CYP1B1 in a separate study (102). Further, Cho and coworkers demonstrated that reactive oxygen species formation by CYP2E1 is reduced by the presence of increasing amounts of anionic phospholipids (103). It is evident that lipid composition serves an important role in modulating CYP structure and function and is an important factor to consider for *in vitro* models. However, it should be noted these studies primarily focused on the charge of the phospholipid head group. Furthermore, these studies were not performed using larger model membranes such as liposomes, increasing the potential for contributions from CYP-CYP interactions as well.

Molecular dynamics has been used to probe the effects of membrane composition on CYP3A4 structural dynamics. Cholesterol is well known to be an important modulator of membrane lipid order (104). Navratilova and coworkers performed molecular dynamics simulations for CYP3A4 in a DOPC membrane containing varying amounts of cholesterol (105). They observed an increase in membrane order and a concomitant decrease in CYP3A4 structural flexibility. Furthermore, they observed that cholesterol lowered the flexibility of the membrane-immersed parts of CYP3A4. Although cholesterol itself is not a phospholipid, this observation demonstrates the potential for membrane composition to play an important role in modulating CYP active site channel flexibility and warrants further investigation.

Here, we investigate the thermal unfolding properties of human CYP3A4 in membranes of various lipid compositions. Whereas many previous studies of CYP-membrane interactions investigated the effects of the charge of the phospholipid head groups on enzyme structure and function, this study focuses on the effects of phospholipid acyl chain length and saturation. Similar to the well-documented effects of cholesterol on membranes, the use of lipids of different acyl chain structure could potentially alter the lipid packing properties of the

membrane, which in turn may have a profound effect on CYP3A4 structure, stability, and dynamics. Phospholipid bilayer nanodiscs as a model membrane system allow for monomerization of CYP, eliminating potential protein-protein interactions and simultaneously providing a system in which the lipid composition can be easily manipulated. Here we incorporate CYP3A4 into mixed lipid phospholipid bilayer nanodiscs in order to investigate the effects of lipid composition on the thermal unfolding and channel dynamics of the CYP monomer.

4.2 Materials and Methods

4.2.1 Reagents.

All reagents were purchased from Sigma-Aldrich (St. Louis, MO), unless otherwise stated.

4.2.2 Protein Expression and Purification.

CYP3A4 and membrane scaffold protein (MSP1D1) was expressed and purified as described in Chapter 2. The MSP1D1 his-tag was cleaved and removed with ProTEV Plus (Promega Corp., Madison, WI) as described in Chapter 2.

4.2.3 Mixed Lipid Nanodisc Assembly.

1-palmitoyl-2-oleoyl-*sn*-glycero-3-phosphocholine (POPC) and 1,2-dimyristoyl-*sn*-glycero-3-phosphocholine (DMPC) were purchased from Avanti Polar Lipids, Inc. (Alabaster, AL). Chloroform stocks of lipid were mixed in varying POPC:DMPC ratios prior to drying down of the lipid films and overnight desiccation. Nanodiscs were then formed as described as in Chapter 2 using disc forming buffer (DFB; 100 mM potassium phosphate, 50 mM sodium chloride, pH 7.4). Lipid films were resuspended in DFB and mixed with MSP1D1 in the presence of sodium

cholate and incubated at 4°C with gentle nutation for 4 hours prior to the addition of Amberlite XAD-2 resin. Samples were allowed to incubate for an additional 4 hours prior to removal of resin. Nanodiscs were analyzed by size exclusion chromatography (SEC) using a Superdex 200 10/300 GL size exclusion column (GE Healthcare Life Sciences, UK) in order to assess nanodisc quality. The total lipid:MSP ratio for each nanodisc composition was empirically optimized on the basis of peak retention time and shape. After optimization of the lipid:MSP ratio, CYP3A4-nanodiscs were assembled and purified as described in Chapter 2. Small aliquots of CYP3A4-nanodiscs samples were analyzed for proper assembly using SEC, and for enzyme integrity using CO-binding spectroscopy by the method of Omura and Sato (65).

4.2.4 Laurdan Nanodisc Assembly.

The fluorescent probe Laurdan (6-dodecanoyl-2-dimethylaminonaphthalene) was purchased from Invitrogen (Eugene, OR). Laurdan was mixed with lipid in a lipid:laurdan ratio of 200:1 prior to drying of the lipid film for each mixed lipid nanodisc sample. Laurdan-containing lipid films were then resuspended in disc forming buffer (DFB; 100 mM potassium phosphate, 50 mM sodium chloride, pH 7.4), and mixed with MSP1D1 in the presence of sodium cholate according to the optimized lipid to scaffold protein ratios determined above. The assembly of the empty nanodiscs is as described in Chapter 2.

4.2.5 Equilibrium Binding Titrations.

Equilibrium binding titrations using ketoconazole (KTZ) and mixed lipid CYP3A4-nanodisc samples were performed and analyzed essentially as described in Chapter 3 using an Aminco DW2a spectrophotometer (Olis, Inc., GA). All binding titrations were carried out at 25 °C using a scan range of 350-700 nm. A sample cuvette containing 1.4 μM CYP3A4-nanodiscs and a reference cuvette containing an equivalent concentration of empty nanodiscs of matching lipid

composition were placed inside the spectrophotometer and allowed to equilibrate to temperature for 10 minutes before a ligand-free absorbance spectrum was collected. KTZ was prepared in 75 μM and 125 μM stocks dissolved in 50% methanol. 1 μL of KTZ was added to both cuvettes prior and absolute spectra were recorded for each addition of ligand. The final methanol concentration did not exceed 2%. Data were baseline-corrected and corrected for the change in volume, and difference spectra were calculated by subtracting the ligand-free spectrum for CYP3A4 or CYP3A4-NDs from the spectra collected from each subsequent addition of KTZ. Binding isotherms were generated by plotting the difference between the absorbance maximum and minimum of the spectra as a function of ligand concentration, and data were fit to the quadratic binding equation using IgorPro (Wavemetrics, Inc., OR) in order to determine the dissociation constant K_D, as described in chapter 2.

4.2.6 Differential Scanning Calorimetry.

Differential scanning calorimetry (DSC) experiments were performed in the same manner as described in Chapter 3. Nanodisc samples were diluted to 2.5 μM and dialyzed overnight in DFB prior to analysis. The melting temperature T_m, calorimetric enthalpy of unfolding (ΔH_{cal}), heat capacity (ΔC_p), and spectral deconvolution for each sample was analyzed using the analysis software package Origin (MicroCal).

4.2.7 Fluorescence Spectroscopy.

Fluorescence Spectroscopy was performed using an Aminco-Bowman Series 2 Spectrometer (Thermo Scientific, Waltham, MA) equipped with a temperature-controlled water bath. For each mixed lipid nanodisc sample, the cuvette was filled with laurdan-nanodiscs at a concentration of 5 μM and allowed to equilibrate at 25 °C for 10 minutes. The sample was then excited at 340 nm

and fluorescence emissions were collected from 400-600 nm. The laurdan generalized polarization (G.P.) function was used to determine the G.P. at each temperature (106):

$$G.P. = \frac{I_{440} - I_{490}}{I_{440} + I_{490}} \qquad \text{Eq. 1}$$

where I_{440} and I_{490} are the fluorescence intensities of the sample at 440 nm and 490 nm, when excited at 340 nm respectively. G.P. was plotted as a function of temperature in order to estimate the membrane transition temperature.

4.2.8 Stopped-Flow Spectroscopy.

Stopped-flow spectroscopy was performed using an Applied Photophysics SX-20 stopped-flow apparatus (Surrey, UK). All stopped-flow experiments were performed at 25 °C using a 1:10 mixing setup. A 250 µL syringe was filled KTZ in methanol co-solvent which was diluted to 55 µM with DFB, and a 2.5 mL syringe was filled with CYP3A4-nanodiscs of varying lipid composition diluted to an initial concentration of 0.55 µM with DFB. This results in final KTZ and CYP3A4/CYP3A4-nanodisc concentrations of 5 µM and 0.5 µM, respectively. The contents of both syringes were rapidly mixed and absorbance data were rapidly collected using a photodiode array detector. The absorbance difference between 434 nm and 409 nm was plotted as a function of time (t) and best fit to an equation for a biphasic process:

$$Abs = Abs_{max} - A_{fast}e^{-k_{fast}*(t-t_0)} - A_{slow}e^{-k_{slow}*(t-t_0)} \qquad \text{Eq. 2}$$

where Abs_{max} is the maximum absorbance change, t_0 is the earliest time point that is fit to the equation, A_{fast} and A_{slow} are the magnitudes of the fast and slow phases of the curves, respectively, and k_{fast} and k_{slow} are the observed rates for the fast and slow phases, respectively.

4.3 Results

4.3.1 Optimization of Mixed Lipid Nanodiscs.

Prior to performing thermodynamic and kinetic studies, it was necessary to empirically optimize the amount of total lipid required in order to form nanodiscs containing a mixture of the lipids POPC and DMPC. Structurally, POPC and DMPC differ in chain length and degree of saturation (Fig. 1). The acyl chains of POPC are longer than in DMPC, and POPC also contains a site of unsaturation whereas the DMPC acyl chains are fully saturated. The optimized lipid:MSP1D1 ratios for the formation of nanodiscs containing pure POPC or pure DMPC has been reported previously by Bayburt and Sligar (40). Size-exclusion chromatograms for the optimized empty nanodiscs are shown in Figure 2a. Pure POPC nanodiscs have an optimized lipid:MSP1D1 ratio of 65:1, whereas in pure DMPC nanodiscs the ratio is 80:1. When forming mixed lipid nanodiscs, the optimized total lipid:MSP1D1 ratio did not follow a linear trend as initially expected. Rather, an initial decrease in the lipid:MSP1D1 ratio was seen, with an apparent minimum occurring when the DMPC content reaches 50% (Fig. 2b). After the minimum was reached, the amount of lipid necessary to properly form nanodiscs increased with increasing DMPC content until the optimized ratio for pure DMPC nanodiscs was reached (80:1). Because the lipid:MSP1D1 ratio did not follow a linear trend with increasing DMPC, this is an indicator that there is a difference in packing of the mixed lipids which must be dictated by acyl chain length and/or saturation.

After optimization of the total lipid:MSP ratio, CYP3A4 was incorporated into mixed lipid nanodiscs. CYP3A4 was successfully incorporated into nanodiscs containing 0%, 25%, 50%, and 75% molar DMPC content, as verified by SEC and CO-binding spectroscopy (Fig. 3, a and b). However, although it was possible to incorporate CYP3A4 into pure DMPC nanodiscs (Fig. 3c), the CO-binding spectroscopy indicated that the enzyme was largely inactive. As such,

further experiments with CYP3A4-nanodiscs containing 100% DMPC content were not performed.

4.3.2 Ketoconazole Equilibrium Binding Titrations.

Prior to performing DSC or stopped-flow spectroscopy experiments with KTZ, we wished to investigate any effects of the nanodisc lipid composition on the equilibrium binding affinity of KTZ to the CYP3A4 active site. Figure 4 shows the absolute spectra and binding isotherms generated from the titration of CYP3A4-nanodiscs (containing 25%, 50%, or 75% DMPC with KTZ). The measured dissociation constants for the mixed lipid nanodisc samples, as well as the reported dissociation constants for pure POPC CYP3A4-nanodiscs and CYP3A4 in DFB from Chapter 3, are summarized in Table 1. KTZ binds with a lower affinity to the CYP3A4 active site after incorporation into a membrane. However, no significant differences are observed in the KTZ binding affinity between nanodiscs of different lipid composition. This likely indicates that the membrane induces similar conformational changes in CYP3A4 regardless of chain length and saturation. This may also suggest that CYP3A4 conformational differences could be dominated by interactions with the phospholipid head groups, an idea which should be investigated further.

Table 1. Dissociation constants for KTZ binding to CYP3A4 samples.

Sample	K_D (μM)
CYP3A4[a]	0.081 ± 0.010
0% DMPC[b]	0.127 ± 0.010
25% DMPC[b]	0.138 ± 0.008
50% DMPC[b]	0.130 ± 0.009
75% DMPC[b]	0.134 ± 0.006

[a] Analyzed in DFB in the absence of a membrane.
[b] CYP3A4-nanodiscs

4.3.3 Differential Scanning Calorimetry – Empty Nanodiscs.

Prior to performing thermodynamic studies of CYP3A4 in mixed lipid nanodiscs, it was necessary to verify the formation of a well-mixed lipid bilayer within empty nanodiscs via DSC. Empty nanodiscs prepared using POPC, DMPC, or a 1:1 mixture of POPC:DMPC were analyzed using DSC. The gel-to-liquid transition temperatures for the lipids POPC and DMPC are -2 °C and 24 °C, respectively. Each nanodisc sample displayed a reversible gel-to-liquid phospholipid transition. At the lowest temperature analyzed, the POPC lipid transition in nanodiscs is nearly complete (Fig. 5). In contrast, the full DMPC transition at ~25 °C was observed. If the mixed lipid nanodisc preparations were not forming heterogeneous membranes, but rather had formed an ensemble mixture of pure POPC and pure DMPC nanodiscs, then it would be expected that both the tail end of the POPC transition as well as the full DMPC transition at ~25 °C would be present. However, the empty 50% DMPC nanodisc samples show a lipid transition temperature which is approximately halfway between the transition temperatures for POPC and DMPC. Furthermore, I did not observe the appearance of any transitions at the DMPC transition

temperature of ~25 °C appear in this range, confirming that the mixed lipid nanodiscs contain a heterogeneous lipid composition. In addition, the lipid transitions do not significantly overlap with the expected temperature range for the CYP3A4 endotherm (~40 – 65 °C), thus eliminating potential ambiguity in the DSC results discussed in the following section.

4.3.4 Differential Scanning Calorimetry – CYP3A4 Mixed Lipid Nanodiscs.

As was alluded to in Chapter 3, lipid composition could potentially affect the stability of CYP3A4 in the nanodisc. To further investigate this, CYP3A4-nanodiscs with varying POPC and DMPC content were assembled and analyzed using DSC. The DSC thermograms for CYP3A4-nanodiscs containing 0%, 25%, 50%, and 75% molar DMPC content in the absence of ligand are shown in Figure 6a. A relatively large increase in the CYP3A4 melting temperature was observed when 50% DMPC content was reached, relative to CYP3A4 nanodiscs containing 0% and 25% DMPC (Fig. 7a). When the DMPC content was further increased from 50% to 75%, a decrease in the CYP3A4 melting temperature was observed that was slightly lower than the transition observed in the 25% DMPC sample. This follows a trend similar to what was observed for the optimized total lipid:MSP ratios for mixed lipid nanodisc samples discussed above and indicates that CYP3A4 stability is maximized in POPC nanodiscs when the DMPC content is 50%. This same trend is observed when comparing ΔH_{cal} for each lipid composition, with maximum values observed at 50% DMPC content (Fig. 7b).

Calorimetric enthalpy (ΔC_p) was also analyzed. ΔC_p has been shown to be correlated with changes in the solvent accessibility, with larger values corresponding to a less solvent-exposed protein (107). Here, ΔC_p is used as an estimate of the degree of CYP3A4 insertion into the membrane. Similar to what was observed for ΔH_{cal}, ΔC_p showed an increase with increasing DMPC content, with an apparent maximum at 50% DMPC (Fig. 7c). Further increasing DMPC

content to 75% resulted in a decrease in ΔC_p. The experimentally observed parameters have been summarized in Table 2.

Table 2. Comparison of melting temperatures for CYP3A4 nanodiscs in the presence and absence of ketoconazole.

	T_m (°C)		Total ΔH_{cal} (cal/mol)		ΔC_p (cal/mol/°C)	
System	-KTZ	+KTZ[a]	-KTZ	+KTZ[a]	-KTZ	+KTZ[a]
CYP3A4[b]	50.1	51.8	8.9×10^4	9.0×10^4	7.6×10^3	4.6×10^3
0% DMPC[c]	54.8	61.2	1.5×10^5	2.4×10^5	3.3×10^3	1.1×10^4
25% DMPC[c]	54.3	60.1	2.0×10^5	2.2×10^5	5.0×10^3	8.1×10^3
50% DMPC[c]	59.5	60.8	2.4×10^5	2.6×10^5	1.2×10^4	1.8×10^4
75% DMPC[c]	54.0	60.5	1.5×10^5	1.6×10^5	1.8×10^3	2.0×10^3

[a]50 μM ketoconazole.
[b]Analyzed in the absence of nanodiscs.
[c]CYP3A4-nanodisc samples.

In order to test the effects of a hydrophobic ligand on unfolding, KTZ was added to each nanodisc sample prior to DSC analysis (Fig. 6b), and the resulting experimental parameters can be found in Table 2. In addition to the added complexity of the unfolding transition (as observed for pure POPC nanodiscs reported in Chapter 3), the inclusion of KTZ results in an increase of the CYP3A4 melting temperature to ~60 °C for all nanodisc samples, regardless of the corresponding ligand-free melting temperature. Except in the case of 75% DMPC, the addition of KTZ causes ΔH_{cal} and ΔC_p to have identical values across all nanodisc lipid compositions analyzed. The discrepancy in the data for 75% DMPC may be related to effects of lipid packing on CYP3A4 membrane insertion (see discussion).

4.3.5 Generalized Polarization of Laurdan-Nanodiscs.

The observed differences in the T_m, ΔH_{cal}, and ΔC_p values suggests differences in the ordering of the lipids within the nanodisc bilayer. In order to investigate this further, Laurdan

fluorescence was used to study the membrane phase of empty mixed lipid nanodiscs. Laurdan is a small, hydrophobic fluorescent probe of the membrane lipid phase and readily incorporates into both ordered and disordered lipid phases equally (106). This fluorescent probe displays a phase-dependent shift in its emission spectra, and using equation 1, Laurdan generalized polarization (G.P.) can be calculated based on this spectral shift, providing information about the membrane lipid phase (G.P. decreases with increasing lipid order). Plotting the G.P. value as a function of nanodisc DMPC content reveals information about how lipid composition affects the nanodisc membrane phase. Laurdan was incorporated into nanodiscs containing various ratios of DMPC. Figure 8 shows the G.P. values for mixed lipid nanodiscs of various DMPC content at 25 °C. As the amount of DMPC in the nanodisc is increased, the Laurdan G.P. is increased. Therefore, there is a continuous increase in the ordering of the lipids at increasing levels of DMPC.

4.3.6 Stopped-Flow Spectroscopy.

In order to test the effects of nanodisc lipid composition on the dynamics of ligand binding to CYP3A4, stopped-flow spectroscopy was used to monitor the binding kinetics of 5 μM KTZ to CYP3A4-nanodiscs containing various lipid compositions. As can be seen from figure 9, binding of KTZ to CYP3A4 is biphasic both in DFB and for all nanodisc lipid compositions analyzed. The extracted kinetic parameters for k_1 are summarized in Table 3. Upon incorporation of CYP3A4 into pure POPC nanodiscs, a ~2.6-fold increase in the fast phase for KTZ binding is observed. The observed rate for the fast phase is further increased with increasing DMPC content, up to 50%, where it exhibited a ~2-fold increase in the fast phase relative to pure POPC nanodiscs (Fig. 9f). Further increasing DMPC content to 75% resulted in a ~1.4-fold decrease in the fast phase relative to nanodiscs containing 50% DMPC. This follows the general trend which was observed for the DSC results above, as well as in the optimized total

lipid:MSP ratio for the mixed lipid nanodiscs. The slow phase increased upon incorporation of CYP3A4 into pure POPC nanodisc relative to CYP3A4 in DFB. However, in nanodiscs, the slow phase for KTZ binding to CYP3A4 decreased with increasing DMPC content.

Table 3. Observed rates of 5 μM KTZ Binding to CYP3A4.

Sample	k_{fast} (s^{-1})	k_{slow} (s^{-1})	A_{fast} (x 10^{-4})	A_{slow} (x 10^{-4})	% Fast
CYP3A4[a]	1.84 ± 0.04	0.152 ± 0.003	32.7 ± 0.4	17.9 ± 0.2	64.7
0% DMPC[b]	4.80 ± 0.18	0.939 ± 0.141	54.7 ± 1.3	6.5 ± 1.3	89.3
25% DMPC[b]	8.73 ± 0.28	0.363 ± 0.044	57.3 ± 1.1	4.0 ± 0.4	93.5
50% DMPC[b]	9.51 ± 0.16	0.349 ± 0.033	57.8 ± 0.5	2.5 ± 0.2	95.9
75% DMPC[b]	6.61 ± 0.13	0.172 ± 0.019	56.6 ± 0.7	2.7 ± 0.2	95.5

[a]Analyzed in the absence of nanodiscs.
[b]CYP3A4-nanodisc samples.

In addition, the fast fraction of the kinetic traces increased from ~65% to ~90% upon incorporation of CYP3A4 into nanodiscs, consistent with what was observed for bromocriptine and cyanide anion in Chapter 2. This is likely reflective of a more conformationally homogeneous CYP3A4 population upon monomerization by the nanodisc membrane.

4.4 Discussion

The endoplasmic reticulum membrane *in vivo* is a heterogeneous mixture of lipids and other protein components. Despite this, there has not been a lot of emphasis placed on understanding how lipid composition affects mammalian CYP stability and function. It has previously been demonstrated by several groups that membrane charge affects insertion and activity of several mammalian CYP isoforms (37,100-103). However few studies have specifically investigated how acyl chain length and saturation influences CYP-membrane interactions, and to the best of our knowledge, no lipid composition studies have been performed

on a monomeric CYP using phospholipid bilayer nanodiscs. In order to begin addressing this question, I prepared CYP3A4-nanodiscs with varying ratios of POPC:DMPC for analysis by several biophysical techniques.

Because the optimal lipid:MSP1D1 ratios for POPC and DMPC nanodiscs are 65:1 and 80:1, respectively, it was initially expected that the total lipid required to make mixed lipid nanodiscs would increase linearly as the DMPC content is increased in pure POPC nanodiscs. However, an initial decrease in total required lipid content was observed with increasing DMPC, with an apparent minimum at 50% DMPC, followed by an increase in the total lipid at DMPC levels above 50%. That less lipid is required to form mixed lipid nanodiscs than initially expected indicates that lipid packing has overall become more efficient. Laurdan fluorescence experiments show that the lipid phase becomes more ordered with increasing DMPC content (Figure 7). Membrane hydration may be a critical factor in the efficiency of lipid packing in mixed lipid nanodiscs. The concept of membrane hydration affecting lipid packing was initially proposed by White and King (108). Their studies suggest that water molecules form electrostatic interactions with the charged head groups of the lipids in the membrane, causing an increase in its molecular volume. Laurdan fluorescence is dependent upon the reorientation of water molecules near its fluorescent moiety (106). The Laurdan fluorescence emissions maxima shifts to longer wavelengths as more water molecules are able to reorient in the membrane, resulting in lower GP values. Here, it is proposed that as the lipid composition of the nanodisc membrane becomes more heterogeneous, the molecular volume of the lipid head groups is increased due to an increase in their hydration state, resulting in the observed decrease in total lipid content. Despite the lipids occupying more space in the membrane, the lipid order appears to be dictated

by the presence of DMPC, with this lipid inhibiting the rate of reorientation of water molecules within the membrane.

I have characterized the thermal unfolding of CYP3A4 in mixed lipid nanodiscs using DSC to investigate lipid composition effects on the enzyme transition. Unfortunately, I was unable to form CYP3A4 nanodiscs using pure DMPC as the enzyme was largely inactive after completing the nanodisc assembly protocol (Fig 3d). This may be due to the tight-lipid packing of DMPC as observed by Laurdan generalized polarization (Fig. 8). Work done by Monk and co-workers suggest the possibility that electrostatic interactions are formed between the N-terminal anchor of CYP51 and its catalytic domain, which may influence stability and channel dynamics (50). Although it remains unclear whether a similar interaction could potentially form in CYP3A4, a possible explanation for inactive CYP3A4 in pure DMPC nanodiscs may be that, due to the physical constraints the tightly-packed DMPC membrane places on the N-terminal anchor, it is unable to interact with the CYP3A4 catalytic domain, and structural integrity is lost.

Although it was impossible to study the thermal unfolding of CYP3A4 in pure DMPC nanodiscs, it was possible to perform studies on nanodiscs up to 75% DMPC content. CYP3A4 stability initially increases with increasing heterogeneity of the nanodisc membrane (Figure 6). Similar to what I observed for the optimized total lipid content, a maximum melting temperature was observed at 50% DMPC. The corresponding ΔH_{cal} and ΔC_p values followed a similar trend: at 50% DMPC content, CYP3A4 has the least amount of aqueous solvent-accessible surface area. Lipid composition is the only component of the nanodisc samples that is being altered, indicating that the changes in thermodynamic properties of CYP3A4 unfolding are due to the increased lipid heterogeneity of the membrane. The increase in the membrane-associated surface area presumably can also cause an increase in the relative amount of stabilizing van der Waal's

interactions, resulting in a more stable enzyme. Membranes *in vivo*, including the endoplasmic reticulum and the mitochondrial membranes in which mammalian CYPs are primarily located, naturally contain a complex mixture of lipids and other membrane components (35,95). These data reflect the likelihood that CYP3A4 and other mammalian CYPs have evolved to take advantage of the complexities of the membrane in order to maximize their stability and function.

The effects of saturating CYP3A4 with KTZ, a tight-binding CYP3A4 inhibitor, were also investigated using DSC. Typically, the binding of ligands to proteins results in an increase in thermostability of the protein due to an increase in the free energy of unfolding, which is a result of the additional stabilizing interactions formed between the protein and the ligand (109-111). Indeed, KTZ enhanced the stability of CYP3A4 both in DFB and in my mixed lipid nanodisc samples. Notably, for all CYP3A4-nanodisc samples, CYP3A4 transition was increased to ~60 °C, regardless of lipid composition. Recalling that the KTZ binding affinity remains relatively unchanged amongst CYP3A4 nanodiscs containing varying ratios of POPC:DMPC, this result suggests a similar ligand-induced conformational change occurring among all of the nanodiscs. It is possible that more heterogeneous lipid compositions cause CYP3A4 to appear in a conformer more closely resembling that of the KTZ-bound state, which could explain why the T_m of CYP3A4 does not shift to the same degree for the varying mixed lipid nanodisc samples.

The increased stability of CYP3A4 in the more heterogeneous nanodisc membranes could also be explained by a membrane-induced decrease in enzyme flexibility. Ligand binding to CYPs is a complex process that is to some degree dependent upon the dynamics of active site access channels ((22,26,27). Altering the flexibility of CYP3A4 may therefore significantly alter the dynamics of ligand binding to the buried active site. To this end, stopped-flow spectroscopy was used to monitor the binding of KTZ to CYP3A4. The observed rates for k_{fast} increased with

increasing DMPC content up to 50%, followed by a decrease in rate at 75%, indicating that lipid composition is affecting KTZ binding dynamics. By contrast, the observed rates for k_{slow} show a steady decrease with increasing DMPC content. On the basis of previous observations with cyanide and bromocriptine binding to CYP3A4 (Chapter 2), it appears likely that the slow phase corresponds to a conformational change event in CYP3A4. It is therefore hypothesized that the changes observed for k_{fast} in nanodiscs of varying DMPC content may be the result of alterations in flexibility of channel opening. At 50% DMPC content, the dominant channel(s) utilized by KTZ may have the widest diameter and/or fluctuate between an 'open' and 'closed' state with the greatest frequency. The observed changes in the k_{slow} values may be reflective of the interconversion rate between different CYP3A4 conformers being altered as the lipid compositions is changed. Further kinetic studies and modeling using a range of KTZ concentrations are necessary in order to investigate this further.

4.5 Conclusion

This work is the first study of the effects of lipid composition on monomeric CYP3A4 using nanodiscs. The data indicate that lipid acyl chain length composition plays a critical role in modulating the thermal unfolding properties of CYP3A4. Additionally, membrane heterogeneity modulates the kinetics of KTZ binding to the CYP3A4 active site, which could potentially have a significant effect on the kinetics of CYP-mediated drug metabolism. This study highlights the importance of taking into consideration lipid composition when performing studies using membrane-bound CYPs. It would be interesting to investigate how the binding of different ligand types (inhibitors, substrates, modulators) of various sizes affects the thermal unfolding of CYP3A4 as this may provide further insight into how ligand structure and/or type may affect CYP structure. The effects of other lipids (e.g. DPPC, which has a long and fully saturated acyl

chain, or DOPC, which has two sites of unsaturation) should be studied in the future in order to establish any possible correlations between acyl chain length and saturation on CYP stability and function. Using mixed lipid nanodiscs in conjunction with other techniques, such as hydrogen-deuterium exchange mass spectrometry, may also provide insight as to the relative flexibility of the enzyme with varying lipid compositions. Mixed lipid nanodiscs can be used to systematically study the effects of lipid composition on other mammalian CYP isoforms and membrane proteins in general.

4.6 Figures

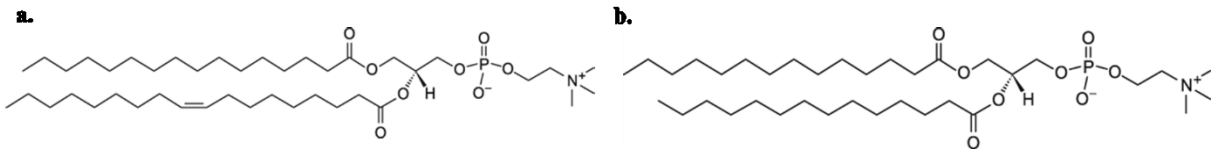

Figure 1. Chemical structures for the longer, unsaturated lipid POPC (a), and the shorter, fully saturated lipid DMPC (b).

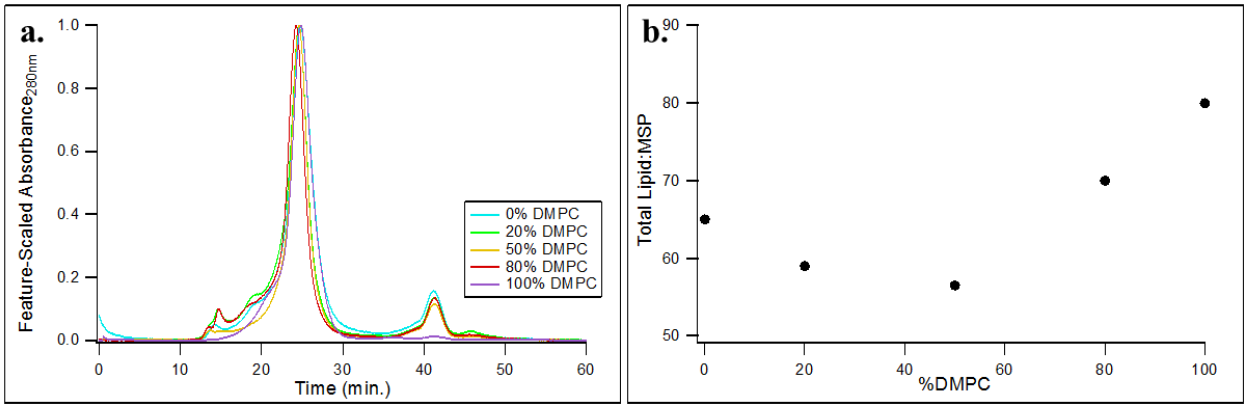

Figure 2. (a) Size-exclusion chromatograms for empty optimized mixed lipid nanodiscs. (b) Optimized total lipid ratios for POPC nanodiscs containing 0, 20, 50, and 80% DMPC or pure DMPC nanodiscs (100%) optimized.

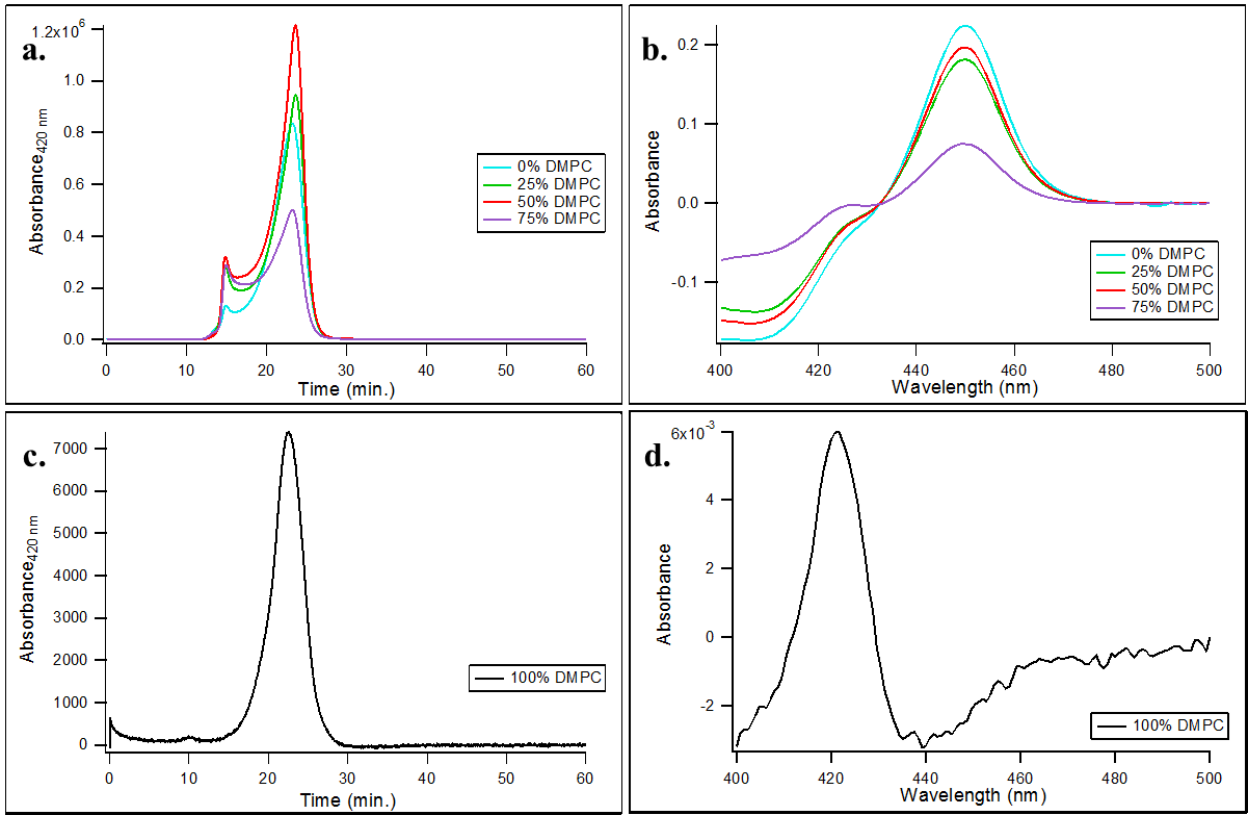

Figure 3. (a) Size exclusion chromatograms for CYP3A4-nanodisc containing 0%, 25%, 50%, and 75% DMPC membrane content. Nanodisc fractions were collected from 22 – 28 minutes. (b) The corresponding CO-binding spectra for the mixed lipid CYP3A4-nanodiscs samples in part a. (c) Size-exclusion chromatogram for CYP3A4-nanodiscs containing 100% DMPC membrane content. (d) Corresponding CO-binding spectra for the CYP3A4-nanodisc sample in part c.

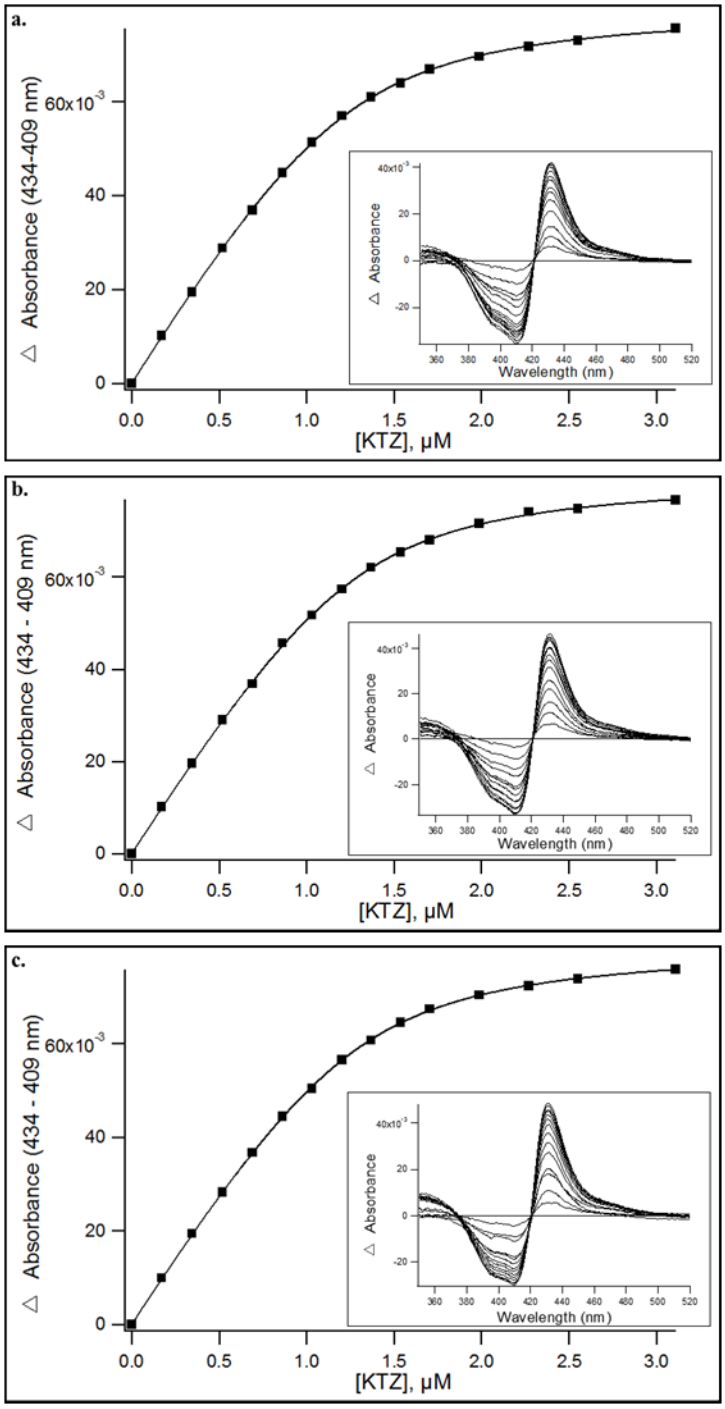

Figure 4. Binding isotherms and the corresponding fit to a quadratic equation for KTZ titrated into CYP3A4-nanodiscs containing (a) 25%, (b) 50%, or (d) 75% DMPC content. (Inset: calculated difference absorbance spectra). The binding of KTZ to CYP3A4-nanodiscs containing 0% DMPC is reported in Chapter 3.

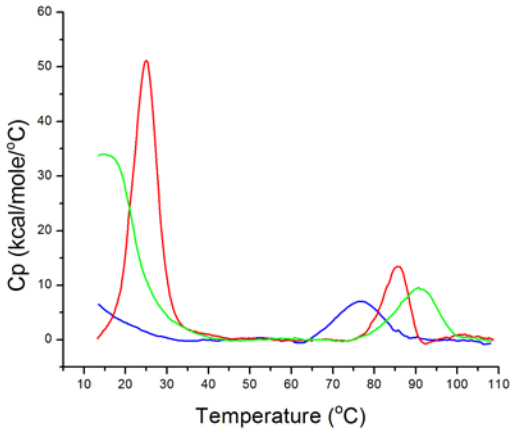

Figure 5. DSC thermogram for empty mixed lipid nanodiscs. Blue – pure POPC nanodiscs (0% DMPC content). Green – Mixed lipid nanodiscs (50% DMPC content). Red – pure DMPC nanodiscs (100% DMPC content).

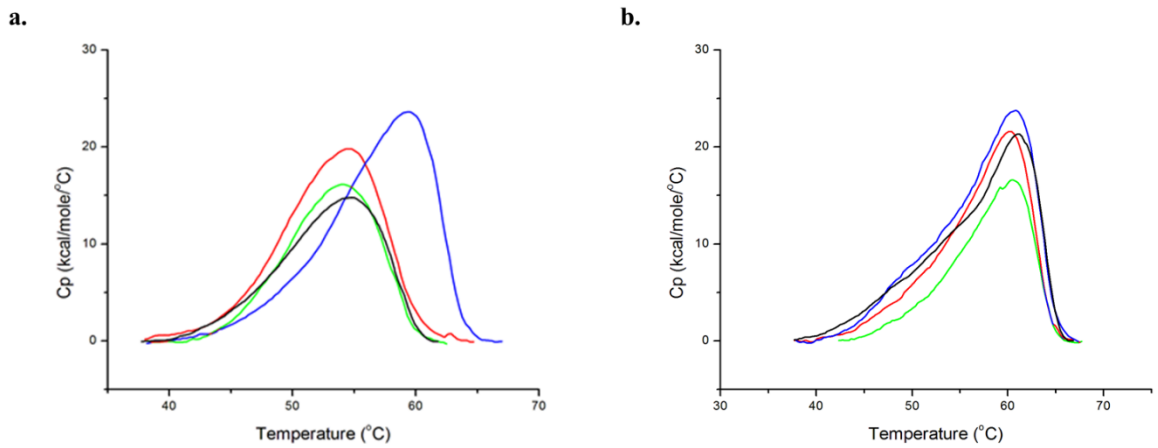

Figure 6. DSC endotherms for the transition of CYP3A4 in nanodiscs containing 0% (black), 25% (red), 50% (blue), or 75% (green) molar DMPC content. Endotherms are shown in the absence (a) or presence (b) of 50 μM KTZ.

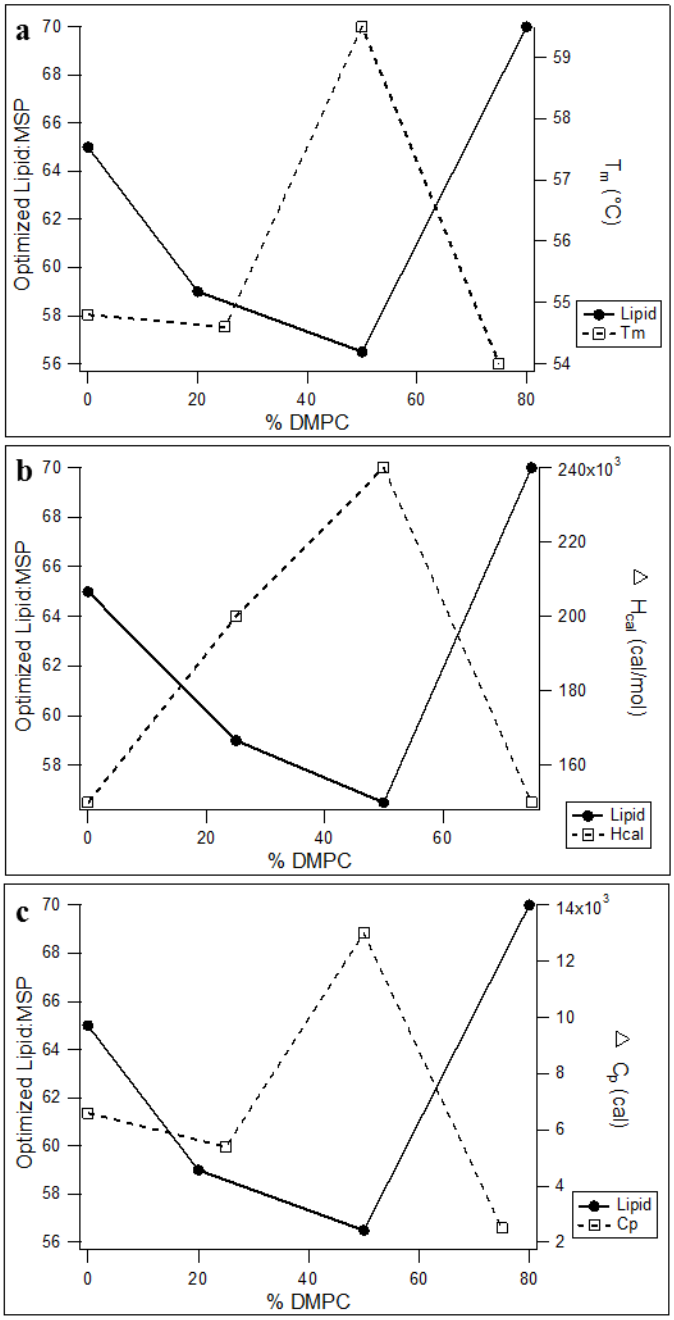

Figure 7. Comparison of the optimized lipid:MSP ratio for mixed lipid nanodiscs with melting temperatures (a), change in calorimetric enthalpy of unfolding (b), and change in heat capacity (c) recovered from differential scanning calorimetry.

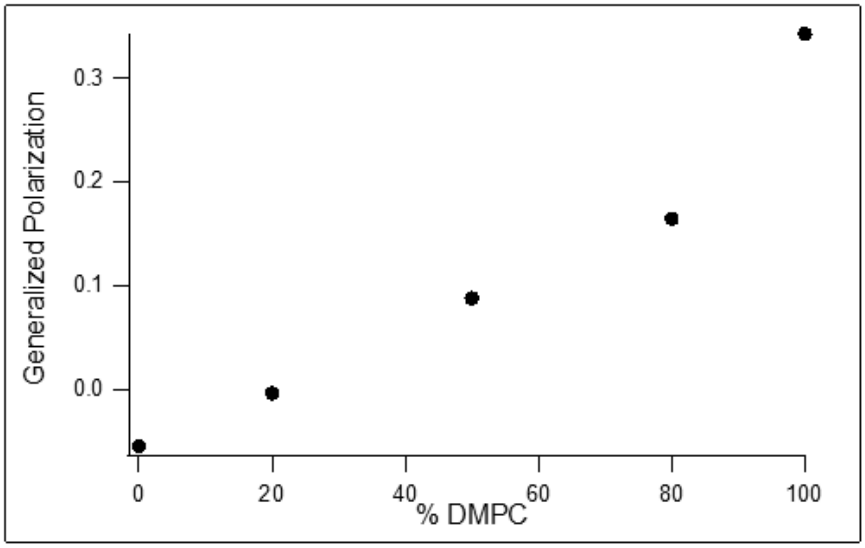

Figure 8. Plot of the Laurdan generalized polarization (G.P.) for POPC nanodiscs with varying DMPC content at 25 °C. Larger G.P. values correspond to a more lipid-ordered membrane.

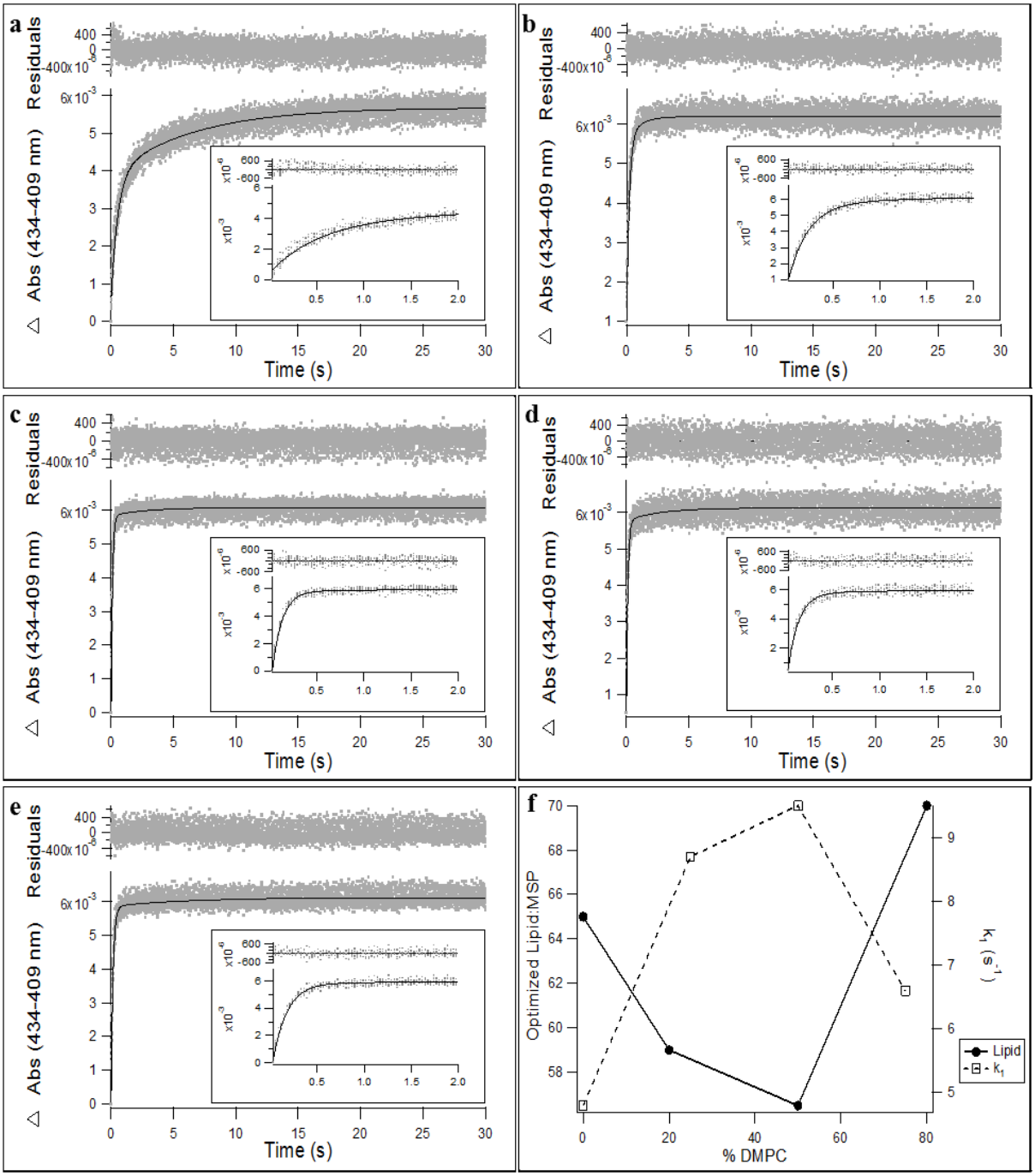

Figure 9. Absorbance kinetic traces and fits for KTZ binding to CYP3A4 in DFB (a), CYP3A4-nanodiscs containing 0% (b), 25% (c), 50% (d), or 75% (e) DMPC content. Insets: the first two seconds of the kinetic traces are shown. (f) Comparison of the optimized total lipid:MSP ratio (left y-axis) and the observed k_1 rate for KTZ binding to CYP3A4 in nanodiscs of varying DMPC content.

References

1. Ortiz de Montellano, P. R. (2005) *Cytochrome P450 : structure, mechanism, and biochemistry*, 3rd ed., Kluwer Academic/Plenum Publishers, New York
2. Aoyama, Y., and Yoshida, Y. (1978) The 14α—demethylation of lanosterol by a reconstituted cytochrome P-450 system from yeast microsomes. *Biochemical and Biophysical Research Communications* **85**, 28-34
3. Aoyama, Y., Kudo, M., Asai, K., Okonogi, K., Horiuchi, T., Gotoh, O., and Yoshida, Y. (2000) Emergence of fluconazole-resistant sterol 14-demethylase P450 (CYP51) in Candida albicans is a model demonstrating the diversification mechanism of P450. *Arch Biochem Biophys* **379**, 170-171
4. Yoshida, Y., Aoyama, Y., Noshiro, M., and Gotoh, O. (2000) Sterol 14-demethylase P450 (CYP51) provides a breakthrough for the discussion on the evolution of cytochrome P450 gene superfamily. *Biochem Biophys Res Commun* **273**, 799-804
5. Nebert, D. W., and Dalton, T. P. (2006) The role of cytochrome P450 enzymes in endogenous signalling pathways and environmental carcinogenesis. *Nature Reviews Cancer* **6**, 947-960
6. Guengerich, F. P. (2008) Cytochrome P450 and chemical toxicology. *Chemical Research in Toxicology* **21**, 70-83
7. Zanger, U. M., and Schwab, M. (2013) Cytochrome P450 enzymes in drug metabolism: Regulation of gene expression, enzyme activities, and impact of genetic variation. *Pharmacology & Therapeutics* **138**, 103-141
8. Yano, J. K., Wester, M. R., Schoch, G. A., Griffin, K. J., Stout, C. D., and Johnson, E. F. (2004) The structure of human microsomal cytochrome P450 3A4 determined by X-ray crystallography to 2.05-A resolution. *J Biol Chem* **279**, 38091-38094
9. Scott, E. E., and Halpert, J. R. (2005) Structures of cytochrome P450 3A4. *Trends in Biochemical Sciences* **30**, 5-7
10. Shimada, T., Yamazaki, H., Mimura, M., Inui, Y., and Guengerich, F. P. (1994) Interindividual Variations in Human Liver Cytochrome-P-450 Enzymes Involved in the Oxidation of Drugs, Carcinogens and Toxic-Chemicals - Studies with Liver-Microsomes of 30 Japanese and 30 Caucasians. *Journal of Pharmacology and Experimental Therapeutics* **270**, 414-423
11. Zhang, Q. Y., Dunbar, D., Ostrowska, A., Zeisloft, S., Yang, J., and Kaminsky, L. S. (1999) Characterization of human small intestinal cytochromes P-450. *Drug Metabolism and Disposition* **27**, 804-809
12. Ogu, C. C., and Maxa, J. L. (2000) Drug interactions due to cytochrome P450. *Proceedings (Baylor University. Medical Center)* **13**, 421-423
13. Rowland, P., Blaney, F. E., Smyth, M. G., Jones, J. J., Leydon, V. R., Oxbrow, A. K., Lewis, C. J., Tennant, M. G., Modi, S., Eggleston, D. S., Chenery, R. J., and Bridges, A. M. (2006) Crystal structure of human cytochrome P450 2D6. *J Biol Chem* **281**, 7614-7622
14. Williams, P. A., Cosme, J., Ward, A., Angove, H. C., Matak Vinkovic, D., and Jhoti, H. (2003) Crystal structure of human cytochrome P450 2C9 with bound warfarin. *Nature* **424**, 464-468
15. Williams, P. A., Cosme, J., Vinkovic, D. M., Ward, A., Angove, H. C., Day, P. J., Vonrhein, C., Tickle, I. J., and Jhoti, H. (2004) Crystal structures of human cytochrome P450 3A4 bound to metyrapone and progesterone. *Science* **305**, 683-686
16. Gay, S. C., Roberts, A. G., and Halpert, J. R. (2010) Structural features of cytochromes P450 and ligands that affect drug metabolism as revealed by x-ray crystallography and NMR (vol 2, pg 1451, 2010). *Future Medicinal Chemistry* **2**, 1612-1612

17. Gerber, N. C., and Sligar, S. G. (1992) Catalytic Mechanism of Cytochrome-P-450 - Evidence for a Distal Charge Relay. *Journal of the American Chemical Society* **114**, 8742-8743
18. Raag, R., Martinis, S. A., Sligar, S. G., and Poulos, T. L. (1991) Crystal-Structure of the Cytochrome-P-450cam Active-Site Mutant Thr252ala. *Biochemistry* **30**, 11420-11429
19. Dubois, R. N., Simpson, E. R., Tuckey, J., Lambeth, J. D., and Waterman, M. R. (1981) Evidence for a Higher Molecular-Weight Precursor of Cholesterol Side-Chain-Cleavage Cytochrome-P-450 and Induction of Mitochondrial and Cytosolic Proteins by Corticotropin in Adult Bovine Adrenal-Cells. *Proceedings of the National Academy of Sciences of the United States of America-Biological Sciences* **78**, 1028-1032
20. Sakaguchi, M., Mihara, K., and Sato, R. (1984) Signal recognition particle is required for co-translational insertion of cytochrome P-450 into microsomal membranes. *Proc Natl Acad Sci U S A* **81**, 3361-3364
21. Williams, P. A., Cosme, J., Sridhar, V., Johnson, E. F., and McRee, D. E. (2000) Mammalian microsomal cytochrome P450 monooxygenase: structural adaptations for membrane binding and functional diversity. *Mol Cell* **5**, 121-131
22. Wade, R. C., Winn, P. J., Schlichting, E., and Sudarko. (2004) A survey of active site access channels in cytochromes P450. *Journal of Inorganic Biochemistry* **98**, 1175-1182
23. Cojocaru, V., Winn, P. J., and Wade, R. C. (2007) The ins and outs of cytochrome P450s. *Biochimica Et Biophysica Acta-General Subjects* **1770**, 390-401
24. Fishelovitch, D., Shaik, S., Wolfson, H. J., and Nussinov, R. (2009) Theoretical Characterization of Substrate Access/Exit Channels in the Human Cytochrome P450 3A4 Enzyme: Involvement of Phenylalanine Residues in the Gating Mechanism. *Journal of Physical Chemistry B* **113**, 13018-13025
25. Black, S. D. (1992) Membrane Topology of the Mammalian P450-Cytochromes. *Faseb Journal* **6**, 680-685
26. Berka, K., Paloncyova, M., Anzenbacher, P., and Otyepka, M. (2013) Behavior of Human Cytochromes P450 on Lipid Membranes. *Journal of Physical Chemistry B* **117**, 11556-11564
27. Baylon, J. L., Lenov, I. L., Sligar, S. G., and Tajkhorshid, E. (2013) Characterizing the Membrane-Bound State of Cytochrome P450 3A4: Structure, Depth of Insertion, and Orientation. *Journal of the American Chemical Society* **135**, 8542-8551
28. Perozo, E., Kloda, A., Cortes, D. M., and Martinac, B. (2002) Physical principles underlying the transduction of bilayer deformation forces during mechanosensitive channel gating. *Nature Structural Biology* **9**, 696-703
29. Phillips, R., Ursell, T., Wiggins, P., and Sens, P. (2009) Emerging roles for lipids in shaping membrane-protein function. *Nature* **459**, 379-385
30. Romsicki, Y., and Sharom, F. J. (1998) The ATPase and ATP-binding functions of P-glycoprotein - Modulation by interaction with defined phospholipids. *European Journal of Biochemistry* **256**, 170-178
31. Sharom, F. J. (2014) Complex Interplay between the P-Glycoprotein Multidrug Efflux Pump and the Membrane: Its Role in Modulating Protein Function. *Front Oncol* **4**, 41
32. Mcelhaney, R. N. (1986) Differential Scanning Calorimetric Studies of Lipid Protein Interactions in Model Membrane Systems. *Biochimica Et Biophysica Acta* **864**, 361-421
33. Shaw, A. W., McLean, M. A., and Sligar, S. G. (2004) Phospholipid phase transitions in homogeneous nanometer scale bilayer discs. *FEBS Lett* **556**, 260-264
34. Anzenbacher, P., Hudeček, J., and Stružinský, R. (1982) Study of thermal stability of cytochrome P450 by differential scanning calorimetry. *FEBS Letters* **149**, 208-210
35. van Meer, G., Voelker, D. R., and Feigenson, G. W. (2008) Membrane lipids: where they are and how they behave. *Nat Rev Mol Cell Biol* **9**, 112-124

36. Ingelman-Sundberg, M., Hagbjork, A. L., Ueng, Y. F., Yamazaki, H., and Guengerich, F. P. (1996) High rates of substrate hydroxylation by human cytochrome P450 3A4 in reconstituted membranous vesicles: influence of membrane charge. *Biochem Biophys Res Commun* **221**, 318-322
37. Ahn, T., Guengerich, F. P., and Yun, C. H. (1998) Membrane insertion of cytochrome P450 1A2 promoted by anionic phospholipids. *Biochemistry* **37**, 12860-12866
38. Denisov, I. G., Grinkova, Y. V., Lazarides, A. A., and Sligar, S. G. (2004) Directed self-assembly of monodisperse phospholipid bilayer Nanodiscs with controlled size. *J Am Chem Soc* **126**, 3477-3487
39. Nath, A., Atkins, W. M., and Sligar, S. G. (2007) Applications of phospholipid bilayer nanodiscs in the study of membranes and membrane proteins. *Biochemistry* **46**, 2059-2069
40. Bayburt, T. H., and Sligar, S. G. (2010) Membrane protein assembly into Nanodiscs. *FEBS Lett* **584**, 1721-1727
41. Ritchie, T. K., Grinkova, Y. V., Bayburt, T. H., Denisov, I. G., Zolnerciks, J. K., Atkins, W. M., and Sligar, S. G. (2009) Reconstitution of Membrane Proteins in Phospholipid Bilayer Nanodiscs. *Methods in Enzymology; Liposomes, Pt F* **464**, 211-231
42. Denisov, I. G., and Sligar, S. G. (2011) Cytochromes P450 in nanodiscs. *Biochim Biophys Acta* **1814**, 223-229
43. Bayburt, T. H., Grinkova, Y. V., and Sligar, S. G. (2002) Self-Assembly of Discoidal Phospholipid Bilayer Nanoparticles with Membrane Scaffold Proteins. *Nano Letters* **2**, 853-856
44. Sessa, G., and Weissmann, G. (1968) Phospholipid spherules (liposomes) as a model for biological membranes. *J Lipid Res* **9**, 310-318
45. Subramanian, M., Low, M., Locuson, C. W., and Tracy, T. S. (2009) CYP2D6-CYP2C9 protein-protein interactions and isoform-selective effects on substrate binding and catalysis. *Drug Metab Dispos* **37**, 1682-1689
46. Gotoh, O. (1992) Substrate recognition sites in cytochrome P450 family 2 (CYP2) proteins inferred from comparative analyses of amino acid and coding nucleotide sequences. *J Biol Chem* **267**, 83-90
47. Schleinkofer, K., Sudarko, Winn, P. J., Ludemann, S. K., and Wade, R. C. (2005) Do mammalian cytochrome P450s show multiple ligand access pathways and ligand channelling? *Embo Reports* **6**, 584-589
48. Shah, M. B., Wilderman, P. R., Pascual, J., Zhang, Q. H., Stout, C. D., and Halpert, J. R. (2012) Conformational Adaptation of Human Cytochrome P450 2B6 and Rabbit Cytochrome P450 2B4 Revealed upon Binding Multiple Amlodipine Molecules. *Biochemistry* **51**, 7225-7238
49. Bell-Parikh, L. C., and Guengerich, F. P. (1999) Kinetics of cytochrome P450 2E1-catalyzed oxidation of ethanol to acetic acid via acetaldehyde. *Journal of Biological Chemistry* **274**, 23833-23840
50. Monk, B. C., Tomasiak, T. M., Keniya, M. V., Huschmann, F. U., Tyndall, J. D. A., O'Connell, J. D., Cannon, R. D., McDonald, J. G., Rodriguez, A., Finer-Moore, J. S., and Stroud, R. M. (2014) Architecture of a single membrane spanning cytochrome P450 suggests constraints that orient the catalytic domain relative to a bilayer. *Proceedings of the National Academy of Sciences of the United States of America* **111**, 3865-3870
51. Berka, K., Hendrychova, T., Anzenbacher, P., and Otyepka, M. (2011) Membrane Position of Ibuprofen Agrees with Suggested Access Path Entrance to Cytochrome P450 2C9 Active Site. *Journal of Physical Chemistry A* **115**, 11248-11255
52. Cojocaru, V., Balali-Mood, K., Sansom, M. S. P., and Wade, R. C. (2011) Structure and Dynamics of the Membrane-Bound Cytochrome P450 2C9. *Plos Computational Biology* **7**

53. Denisov, I. G., McLean, M. A., Shaw, A. W., Grinkova, Y. V., and Sligar, S. G. (2005) Thermotropic phase transition in soluble nanoscale lipid bilayers. *Journal of Physical Chemistry B* **109**, 15580-15588
54. Davydov, D. R., Fernando, H., Baas, B. J., Sligar, S. G., and Halpert, J. R. (2005) Kinetics of dithionite-dependent reduction of cytochrome P450 3A4: Heterogeneity of the enzyme caused by its oligomerization. *Biochemistry* **44**, 13902-13913
55. Kumar, S., Davydov, D. R., and Halpert, J. R. (2005) Role of cytochrome B5 in modulating peroxide-supported cyp3a4 activity: evidence for a conformational transition and cytochrome P450 heterogeneity. *Drug Metab Dispos* **33**, 1131-1136
56. Nath, A., Grinkova, Y. V., Sligar, S. G., and Atkins, W. M. (2007) Ligand binding to cytochrome P450 3A4 in phospholipid bilayer nanodiscs - The effect of model membranes. *Journal of Biological Chemistry* **282**, 28309-28320
57. Khatri, Y., Luthra, A., Duggal, R., and Sligar, S. G. (2014) Kinetic solvent isotope effect in steady-state turnover by CYP19A1 suggests involvement of Compound 1 for both hydroxylation and aromatization steps. *FEBS Lett* **588**, 3117-3122
58. Plucinski, L., Ranjan Gartia, M., Arnold, W. R., Ameen, A., Chang, T. W., Hsiao, A., Logan Liu, G., and Das, A. (2016) Substrate binding to cytochrome P450-2J2 in Nanodiscs detected by nanoplasmonic Lycurgus cup arrays. *Biosens Bioelectron* **75**, 337-346
59. Zhang, M., Huang, R., Ackermann, R., Im, S. C., Waskell, L., Schwendeman, A., and Ramamoorthy, A. (2016) Reconstitution of the Cytb5 -CytP450 Complex in Nanodiscs for Structural Studies using NMR Spectroscopy. *Angew Chem Int Ed Engl* **55**, 4497-4499
60. Isin, E. M., and Guengerich, F. P. (2006) Kinetics and thermodynamics of ligand binding by cytochrome P450 3A4. *Journal of Biological Chemistry* **281**, 9127-9136
61. Peyronneau, M. A., Delaforge, M., Riviere, R., Renaud, J. P., and Mansuy, D. (1994) High-Affinity of Ergopeptides for Cytochromes P450 3a - Importance of Their Peptide Moiety for P450 Recognition and Hydroxylation of Bromocriptine. *European Journal of Biochemistry* **223**, 947-956
62. Fedorov, R., Ghosh, D. K., and Schlichting, I. (2003) Crystal structures of cyanide complexes of P450cam and the oxygenase domain of inducible nitric oxide synthase - structural models of the short-lived oxygen complexes. *Archives of Biochemistry and Biophysics* **409**, 25-31
63. Woods, C. M., Fernandez, C., Kunze, K. L., and Atkins, W. M. (2011) Allosteric Activation of Cytochrome P450 3A4 by alpha-Naphthoflavone: Branch Point Regulation Revealed by Isotope Dilution Analysis. *Biochemistry* **50**, 10041-10051
64. Gillam, E. M. J., Baba, T., Kim, B. R., Ohmori, S., and Guengerich, F. P. (1993) Expression of Modified Human Cytochrome-P450 3a4 in Escherichia-Coli and Purification and Reconstitution of the Enzyme. *Archives of Biochemistry and Biophysics* **305**, 123-131
65. Omura, T., and Sato, R. (1962) A New Cytochrome in Liver Microsomes. *Journal of Biological Chemistry* **237**, 1375-&
66. Baas, B. J., Denisov, I. G., and Sliger, S. G. (2004) Homotropic cooperativity of monomeric cytochrome P450 3A4 in a nanoscale native bilayer environment. *Archives of Biochemistry and Biophysics* **430**, 218-228
67. Hoops, S., Sahle, S., Gauges, R., Lee, C., Pahle, J., Simus, N., Singhal, M., Xu, L., Mendes, P., and Kummer, U. (2006) COPASI- A COmplex PAthway SImulator. *Bioinformatics* **22**, 3067-3074
68. Sevrioukova, I. F., and Poulos, T. L. (2012) Structural and Mechanistic Insights into the Interaction of Cytochrome P4503A4 with Bromoergocryptine, a Type I Ligand. *Journal of Biological Chemistry* **287**, 3510-3517
69. Vogt, A. D., Pozzi, N., Chen, Z., and Di Cera, E. (2014) Essential role of conformational selection in ligand binding. *Biophys Chem* **186**, 13-21

70. Fagerberg, L., Jonasson, K., von Heijne, G., Uhlen, M., and Berglund, L. (2010) Prediction of the human membrane proteome. *Proteomics* **10**, 1141-1149
71. Denisov, I. G., Shih, A. Y., and Sligar, S. G. (2012) Structural differences between soluble and membrane bound cytochrome P450s. *Journal of Inorganic Biochemistry* **108**, 150-158
72. Maves, S. A., and Sligar, S. G. (2001) Understanding thermostability in cytochrome P450 by combinatorial mutagenesis. *Protein Science* **10**, 161-168
73. Panigrahi, R., Arutyunova, E., Panwar, P., Gimpl, K., Keller, S., and Lemieux, M. J. (2016) Reversible Unfolding of Rhomboid Intramembrane Proteases. *Biophys J* **110**, 1379-1390
74. Gill, P., Moghadam, T. T., and Ranjbar, B. (2010) Differential scanning calorimetry techniques: applications in biology and nanoscience. *J Biomol Tech* **21**, 167-193
75. Johnson, C. M. (2013) Differential scanning calorimetry as a tool for protein folding and stability. *Archives of Biochemistry and Biophysics* **531**, 100-109
76. Park, S. Y., Yamane, K., Adachi, S., Shiro, Y., Weiss, K. E., Maves, S. A., and Sligar, S. G. (2002) Thermophilic cytochrome P450 (CYP119) from Sulfolobus solfataricus: high resolution structure and functional properties. *Journal of Inorganic Biochemistry* **91**, 491-501
77. Mak, P. J., Denisov, I. G., Grinkova, Y. V., Sligar, S. G., and Kincaid, J. R. (2011) Defining CYP3A4 structural responses to substrate binding. Raman spectroscopic studies of a nanodisc-incorporated mammalian cytochrome P450. *J Am Chem Soc* **133**, 1357-1366
78. Das, A., Zhao, J., Schatz, G. C., Sligar, S. G., and Van Duyne, R. P. (2009) Screening of type I and II drug binding to human cytochrome P450-3A4 in nanodiscs by localized surface plasmon resonance spectroscopy. *Anal Chem* **81**, 3754-3759
79. Kijac, A. Z., Li, Y., Sligar, S. G., and Rienstra, C. M. (2007) Magic-angle spinning solid-state NMR spectroscopy of nanodisc-embedded human CYP3A4. *Biochemistry* **46**, 13696-13703
80. Hagn, F., Etzkorn, M., Raschle, T., and Wagner, G. (2013) Optimized phospholipid bilayer nanodiscs facilitate high-resolution structure determination of membrane proteins. *J Am Chem Soc* **135**, 1919-1925
81. Sreerama, N., and Woody, R. W. (2000) Estimation of protein secondary structure from circular dichroism spectra: comparison of CONTIN, SELCON, and CDSSTR methods with an expanded reference set. *Anal Biochem* **287**, 252-260
82. Sreerama, N., and Woody, R. W. (2004) On the analysis of membrane protein circular dichroism spectra. *Protein Sci* **13**, 100-112
83. Saboury, A. A., and Moosavi-Movahedi, A. A. (1994) Clarification of calorimetric and van't hoff enthalpies for evaluation of protein transition states. *Biochemical Education* **22**, 210-211
84. Kaur, P., Chamberlin, A. R., Poulos, T. L., and Sevrioukova, I. F. (2016) Structure-Based Inhibitor Design for Evaluation of a CYP3A4 Pharmacophore Model. *J Med Chem* **59**, 4210-4220
85. Sevrioukova, I. F., and Poulos, T. L. (2013) Pyridine-substituted desoxyritonavir is a more potent inhibitor of cytochrome P450 3A4 than ritonavir. *J Med Chem* **56**, 3733-3741
86. Sevrioukova, I. F., and Poulos, T. L. (2013) Dissecting cytochrome P450 3A4-ligand interactions using ritonavir analogues. *Biochemistry* **52**, 4474-4481
87. Ekroos, M., and Sjogren, T. (2006) Structural basis for ligand promiscuity in cytochrome P450 3A4. *Proc Natl Acad Sci U S A* **103**, 13682-13687
88. Zhang, W., Ramamoorthy, Y., Kilicarslan, T., Nolte, H., Tyndale, R. F., and Sellers, E. M. (2002) Inhibition of cytochromes P450 by antifungal imidazole derivatives. *Drug Metab Dispos* **30**, 314-318
89. Inouye, K., Kondo, S., Yamamura, M., Nakanishi, D., and Sakaki, T. (2001) Inhibitory effects of detergents on rat CYP1A1-dependent monooxygenase: comparison of mixed and fused systems consisting of rat CYP 1A1 and yeast NADPH-P450 reductase. *Biochem Biophys Res Commun* **280**, 1346-1351

90. Hosea, N. A., and Guengerich, F. P. (1998) Oxidation of nonionic detergents by cytochrome P450 enzymes. *Arch Biochem Biophys* **353**, 365-373
91. Basudhar, D., Madrona, Y., Kandel, S., Lampe, J. N., Nishida, C. R., and de Montellano, P. R. (2015) Analysis of cytochrome P450 CYP119 ligand-dependent conformational dynamics by two-dimensional NMR and X-ray crystallography. *J Biol Chem* **290**, 10000-10017
92. Stoll, S., Lee, Y. T., Zhang, M., Wilson, R. F., Britt, R. D., and Goodin, D. B. (2012) Double electron-electron resonance shows cytochrome P450cam undergoes a conformational change in solution upon binding substrate. *Proc Natl Acad Sci U S A* **109**, 12888-12893
93. Treuheit, N. A., Redhair, M., Kwon, H., McClary, W. D., Guttman, M., Sumida, J. P., and Atkins, W. M. (2016) Membrane Interactions, Ligand-dependent Dynamics, and Stability of Cytochrome P4503A4 in Lipid Nanodiscs. *Biochemistry*
94. Guengerich, F. P. (1999) Cytochrome P-450 3A4: regulation and role in drug metabolism. *Annu Rev Pharmacol Toxicol* **39**, 1-17
95. van Meer, G., and de Kroon, A. I. (2011) Lipid map of the mammalian cell. *J Cell Sci* **124**, 5-8
96. Smith, A. W. (2012) Lipid-protein interactions in biological membranes: a dynamic perspective. *Biochim Biophys Acta* **1818**, 172-177
97. Schmidt, D., Jiang, Q. X., and MacKinnon, R. (2006) Phospholipids and the origin of cationic gating charges in voltage sensors. *Nature* **444**, 775-779
98. Fong, T. M., and McNamee, M. G. (1986) Correlation between acetylcholine receptor function and structural properties of membranes. *Biochemistry* **25**, 830-840
99. Resh, M. D. (2006) Trafficking and signaling by fatty-acylated and prenylated proteins. *Nat Chem Biol* **2**, 584-590
100. Kim, K. H., Ahn, T., and Yun, C. H. (2003) Membrane properties induced by anionic phospholipids and phosphatidylethanolamine are critical for the membrane binding and catalytic activity of human cytochrome P450 3A4. *Biochemistry* **42**, 15377-15387
101. Yun, C. H., Song, M., and Kim, H. (1997) Conformational change of cytochrome P450 1A2 induced by phospholipids and detergents. *J Biol Chem* **272**, 19725-19730
102. Jang, H. H., Kim, D. H., Ahn, T., and Yun, C. H. (2010) Functional and conformational modulation of human cytochrome P450 1B1 by anionic phospholipids. *Arch Biochem Biophys* **493**, 143-150
103. Cho, E. Y., Yun, C. H., Chae, H. Z., Chae, H. J., and Ahn, T. (2008) Anionic phospholipid-induced regulation of reactive oxygen species production by human cytochrome P450 2E1. *FEBS Lett* **582**, 1771-1776
104. Yeagle, P. L. (1985) Cholesterol and the cell membrane. *Biochim Biophys Acta* **822**, 267-287
105. Navratilova, V., Paloncyova, M., Kajsova, M., Berka, K., and Otyepka, M. (2015) Effect of cholesterol on the structure of membrane-attached cytochrome P450 3A4. *J Chem Inf Model* **55**, 628-635
106. Bagatolli, L. A. (2006) To see or not to see: lateral organization of biological membranes and fluorescence microscopy. *Biochim Biophys Acta* **1758**, 1541-1556
107. Myers, J. K., Pace, C. N., and Scholtz, J. M. (1995) Denaturant M-Values and Heat-Capacity Changes - Relation to Changes in Accessible Surface-Areas of Protein Unfolding. *Protein Science* **4**, 2138-2148
108. White, S. H., and King, G. I. (1985) Molecular packing and area compressibility of lipid bilayers. *Proc Natl Acad Sci U S A* **82**, 6532-6536
109. Fukada, H., Sturtevant, J. M., and Quiocho, F. A. (1983) Thermodynamics of the binding of L-arabinose and of D-galactose to the L-arabinose-binding protein of Escherichia coli. *J Biol Chem* **258**, 13193-13198
110. Shrake, A., and Ross, P. D. (1990) Ligand-induced biphasic protein denaturation. *J Biol Chem* **265**, 5055-5059

111. Rathi, P. C., Fulton, A., Jaeger, K. E., and Gohlke, H. (2016) Application of Rigidity Theory to the Thermostabilization of Lipase A from Bacillus subtilis. *PLoS Comput Biol* **12**, e1004754